

**UCLA**

**UCLA Electronic Theses and Dissertations**

**Title**

Development of Materials and Processes for Additive Manufacturing of Multi-Functional Microarchitected Devices

**Permalink**

<https://escholarship.org/uc/item/65n8k4gr>

**Author**

Hensleigh, Ryan Michael

**Publication Date**

2021

Peer reviewed|Thesis/dissertation

UNIVERSITY OF CALIFORNIA

Los Angeles

Development of Materials and Processes for Additive Manufacturing of Multi-Functional  
Microarchitected Devices

A dissertation submitted in partial satisfaction of the requirements for the degree of Doctor of  
Philosophy in Civil Engineering

by

Ryan Michael Hensleigh

2021

© Copyright by

Ryan Michael Hensleigh

2021

## ABSTRACT OF THE DISSERTATION

Development of Materials and Processes for Additive Manufacturing of Multi-Functional  
Microarchitected Devices

by

Ryan Michael Hensleigh

Doctor of Philosophy in Civil Engineering

University of California, Los Angeles, 2021

Professor Xiaoyu Zheng, Chair

Materials and manufacturing are the critical enabler of our technological world. With new materials and advanced manufacturing, new opportunities for advanced application become possible. Additive manufacturing (AM), or three-dimensional (3D) printing, is a relatively new manufacturing process, which relies on building up of parts from raw material. It reduces manufacturing waste, is flexible in part output, and opens new final part form-factors/architectures to be accessible for advanced applications. Light-based AM is well established in its ability to fabricate complex 3D structures whose unique properties exceed or are unfound in natural materials, called metamaterials. These unique 3D structures and other benefits of light-based AM make it of increasing interest for fabrication of functional devices, energy storage, sensors, and actuators among others. However, the available materials

compatible with light-based AM, and AM in general, is limited. Specific material and processing limitations, viscosity, light absorption, and their underlying chemistry exclude the vast majority of materials from use in light-based AM. The majority of usable materials are on acrylic, vinyl, and thiol-based organic polymers whereas most functional materials are inorganic and not directly compatible.

This dissertation focuses on the development of new materials and processes to allow the light-based AM fabrication of functional materials. This includes graphene energy storage devices, patterned 3D deposition for freeform electronics of multiple materials (conductors, dielectric, magnetic), and high-temperature ceramics for lightweight structural electronics in extreme applications. This dissertation lays the foundation for integrating light-based AM methods to electronic device applications that incorporates conducting and dielectric materials in 3D. Further development can allow advanced antenna, bioelectronics, and structural electronics.

The dissertation of Ryan Michael Hensleigh is approved.

Mathieu Bauchy

David Jassby

Jonathan Hopkins

Xiaoyu Zheng, Committee Chair

University of California, Los Angeles

2021

## DEDICATION

“Imagination will often carry us to worlds that never were. But without it we go nowhere.”

– Carl Sagan

“The difference between the thinking of the paranoid patient and the scientist comes from the latter’s ability and willingness to test out his fantasies or grandiose conceptualizations through the system of checks and balances science has established – and to give up those schemes that are shown not to be valid on the basis of these scientific checks.”

- Richard Rhodes, *The Making of the Atomic Bomb*, pg. 151

Thanks to Dr. Zheng for pushing me to new heights as a researcher. Thanks to my committee members at Virginia Tech and UCLA for their thoughtful comments and guidance. Thanks to Huachen, Zhenpeng, and all my labmates, co-authors, and collaborators for your comradery and hard work over the years. Thanks to Dr. Pedulla, Dr. Hailer, and Dr. Skinner at Montana Tech and the Additive Manufacturing group at LLNL for guiding my early research career, it changed my life. Thanks to Mr. and Mrs. Smith, Mr. Decock, and Mr. Ramsey at CHS for sparking my scientific curiosity. A special thanks to Sameeksha and my family who always encouraged me, listened, and endured years of “experiments” from the molds I grew in my childhood room to the scientist I am today.

# TABLE OF CONTENTS

ACKNOWLEDGEMENTS .....	x
VITA .....	xiii
CHAPTER 1: BACKGROUND AND MOTIVIATION .....	1
References .....	4
CHAPTER 2: 3D PRINTING GRAPHENE AEROGELS FOR ENERGY STORAGE .....	5
2.1 Introduction .....	5
2.2 Microarchitected Graphenes for Arbitrary Graphene Structures .....	6
2.3 Initial Attempts at Fabricating 3DGs via SLA .....	7
2.4 Gel-Dispersion Method .....	10
2.5 MAG Morphology and Composition .....	14
2.6 MAG Mechanical Properties .....	19
2.7 Electrical Properties .....	23
2.8 Formulation Optimization .....	24
2.9 Critical Point Drying Versus Ambient .....	25
2.10 Sonication Effects .....	25
2.11 Polymer Loading Effects .....	28
2.12 MAG Solvent and Furnace Optimization .....	29
2.13 Furnace Treatment Optimization .....	31
2.14 Optimizing Strength MAG .....	35
2.15 Summary and Future Work .....	39
2.16 Acknowledgements .....	39
2.17 Materials and Methods .....	39
2.18 References .....	43
CHAPTER 3: FUNCTIONALIZED PIEZOELECTRIC PARTICLES FOR ENHANCED COMPOSITE RESPONSE .....	48

3.1 Introduction.....	48
3.2 P $\mu$ SL of Piezoelectrics .....	49
3.3 Piezoelectric Fibers.....	54
3.4 Molten Salt Wire Synthesis .....	56
3.5 Summary and Future Work .....	64
3.6 Acknowledgements .....	65
3.7 Materials and Methods .....	66
3.8 References.....	68
<b>CHAPTER 4: PRE-CERAMIC POLYMERS FOR HIGH-TEMPERATURE FUNCTIONAL</b>	
<b>MATERIALS.....</b>	<b>73</b>
4.1 Introduction.....	73
4.2 Formulation of Thiol-ene Stereolithography PDC .....	74
4.3 Functional SiOC 3D Ceramics via Doping.....	76
4.4 Summary and Future Work .....	79
4.5 Acknowledgements .....	80
4.6 Materials and Methods .....	80
4.7 References.....	82
<b>CHAPTER 5: PATTERNED DEPOSITION TO INTEGRATE 3D STRUCTURES INTO</b>	
<b>ELECTRICAL DEVICES .....</b>	<b>84</b>
5.1 Introduction.....	84
5.2 Charge Programmed Deposition .....	85
5.3 Multi-Material Deposition.....	91
5.4 Composites and Devices.....	94
5.5 Ongoing Work.....	97
5.6 Summary and Future Work .....	97
5.7 Acknowledgements .....	98
5.8 Materials and Methods .....	99
5.9 References.....	105

## LIST OF FIGURES AND TABLES

Figure 2-1: FGO MAG .....	10
Figure 2-2: Scheme of MAG resin synthesis .....	11
Figure 2-3: Optical microscopy of GO Gel-Dispersion.....	12
Figure 2-4. MAG Structures .....	13
Table 2-1: MAG Shrinkage .....	14
Figure 2-5: Morphology of MAGs .....	16
Figure 2-6: Raman and XRD of MAGs .....	18
Figure 2-7: Mechanical Properties MAGs .....	21
Figure 2-8: Hierarchical Structure MAGs .....	23
Figure 2-9: Sonication Effects MAG Surface Area .....	26
Figure 2-10: Polymer Loading Effect MAG Surface Area.....	28
Figure 2-11: DMF Evaporation .....	30
Figure 2-12: TGA Polymer, GO and MAG .....	32
Figure 2-13: MAG Weight Loss at Fixed Temperatures .....	33
Figure 2-14: Optimized Furnace Run .....	35
Figure 3-1: Surface Functionalization Piezoelectric Nanoparticles.....	53
Figure 3-2: FTIR and d33 of Functionalized Piezoelectrics .....	53
Figure 3-3: Piezoelectric Wire Composites .....	55

Figure 3-4: KTiNbO5 Rods .....	59
Figure 3-5: PTN Wires.....	60
Figure 3-6: KMN-KT and HMN-HT Wires .....	62
Figure 3-7: MN-T and PMN-PT .....	63
Figure 4-1: P $\mu$ SL of Ceramic.....	75
Figure 4-2: Doped SiOC for Functional 3D Ceramics .....	77
Figure 4-3: Diffusion in Rapid vs Conventionally Sintered SiOC .....	79
Figure 5-1: Overview of Selective Deposition Process .....	87
Figure 5-2: Catalyst Selectively from Surface Polarity .....	89
Figure 5-3: Deposition Programming and Resolution .....	90
Figure 5-4: Conductivity Measurement .....	91
Figure 5-6: Multi-Material Deposition .....	93
Figure 5-7: Tunable Dielectric Constant.....	95
Figure 5-8: Selectively Deposited Piezoelectric Devices .....	96
Figure 5-9: Selective Deposition for Antennas.....	97

## ACKNOWLEDGEMENTS

I would like to gratefully acknowledge funding support from DARPA Young Faculty Award, NSF (CMMI-17277492), Air Force Office of Scientific Research (FA9550-18-1-0299), the Office of Naval Research (N00014-18-1-2553), ICTAS Junior Faculty Award, Lawrence Livermore National Laboratory under the auspices of the U.S. Department of Energy under Contract DE-AC52-07NA27344, through LDRD award 16-ERD-051 (LLNL-JRNL-749080), Virginia Tech Startup funding, and University of California Los Angeles Startup funding.

No commercial reuse without the copyright holders permission is allowed. Contributions of specific co-authors are noted throughout the chapters.

Chapter 2 has been published in revised form in Ryan M Hensleigh, Huachen Cui, James S Oakdale, C Ye Jianchao, Patrick G Campbell, Eric B Duoss, Christopher M Spadaccini, Xiaoyu Zheng, Marcus A Worsley, Additive manufacturing of complex micro-architected graphene aerogels, *Materials Horizons*, 2018, Volume 5, Issue 6, pp. 1035-1041, DOI: <https://doi.org/10.1039/C8MH00668G>, with permission from the Royal Society of Chemistry.

No commercial re-distribution or re-use allowed.

Portions of Chapter 2 are in preparation for publication.

Chapter 3 has been published in a revised form in Huachen Cui, Ryan Hensleigh, Desheng Yao, Deepam Maurya, Prashant Kumar, Min Gyu Kang, Shashank Priya, Xiaoyu (Rayne) Zheng, Three-dimensional printing of piezoelectric materials with designed anisotropy and

directional response, *Nature Materials*, 2019, Volume 18, pp. 234-241,

DOI: <https://doi.org/10.1038/s41563-018-0268-1> *Nature Materials*. No commercial re-distribution or re-use allowed.

Chapter 3 has been published in revised form in Desheng Yao, Huachen Cui, Ryan Hensleigh, Parker Smith, Sam Alford, Dominic Bernero, Sydney Bush, Kyle Mann, H Felix Wu, Marvin Chin-Nieh, Garrett Youmans, Xiaoyu Zheng, Achieving the upper bound of piezoelectric response in tunable, wearable 3D printed nanocomposites, *Advanced Functional Materials*, 2019, Volume 29, Issue 42 DOI: <https://doi.org/10.1002/adfm.201903866>. No commercial re-distribution or re-use allowed.

Chapter 4 has been published in a revised form in Huachen Cui, Ryan Hensleigh, Hongshun Chen, Xiaoyu Zheng, Additive Manufacturing and size-dependent mechanical properties of three-dimensional microarchitected, high-temperature ceramic metamaterials, *Journal of Material Research*, 2018, Volume 33, pp. 360-371, DOI: <https://doi.org/10.1557/jmr.2018.11>, see reference 12. This version is published under a Creative Commons CC-BY-NC-ND. No commercial re-distribution or re-use allowed. Derivative works cannot be distributed. © copyright holder.

Chapter 4 has been published in a revised form in Chengwei Wang, Weiwei Ping, Qiang Bai, Huachen Cui, Ryan Hensleigh, Ruiliu Wang, Alexandra H. Brozena, Zhenpeng Xu, Jiaqi Dai, Yong Pei, Chaolun Zheng, Glenn Pastel, Jinlong Gao, Xizheng Wang, Howard Wang, Ji-Cheng Zhao, Bao Yang, Xiaoyu (Rayne) Zheng, Jian Luo, Yifei Mo, Bruce Dunn, Liangbing Hu, A general method to synthesize and sinter bulk ceramics in seconds, *Science*, 2020, Volume 368, pp. 521-

526, DOI: <https://doi.org/10.1126/science.aaz7681>, see reference 13. No commercial re-distribution or re-use allowed.

Chapter 5 has been published in a revised form in Ryan Hensleigh, Huachen Cui, Zhenpeng Xu, Jeffrey Massman, Desheng Yao, John Berrigan, Xiaoyu Zheng, Charge-programmed three-dimensional printing for multi-material electronic devices, Nature Electronics, Volume 3, Issue 4, pg. 216-224, DOI: <https://doi.org/10.1038/s41928-020-0391-2>, see reference 22. No commercial re-distribution or re-use allowed. Derivative works cannot be distributed.

Portions of Chapter 5 are in preparation for publication.

## VITA

### Degrees

Bachelors of Science, Chemistry, Montana Technological University, 2015

### Employment

Post-College Appointee, Lawrence Livermore National Laboratory, 2015-2016

AMGEN MIT Scholar Langer Lab, AMGEN Foundation, 2014

### Publications

1. Behera et al. “Current Challenges and Potential Directions Towards Precision Microscale Additive Manufacturing–Part II: Laser-Based Curing, Heating, and Trapping Processes.” *Precision Engineering*, 68, 2021
2. C. Wang et al. “A general method to synthesize and sinter bulk ceramics in seconds.” *Science*, 368, 2020
3. R. M. Hensleigh, H. Cui, et al. “Charge-programmed three-dimensional printing for multi-material electronic devices.” *Nature Electronics*, 1-9, 2020
4. D. Yao; H. Cui; R. M. Hensleigh et al. “Achieving the Upper Bound of Piezoelectric Response in Tunable, Wearable 3D Printed Nanocomposites.” *Advanced Functional Materials*, 1903866, 2019
5. H. Cui; R. M. Hensleigh et al. “Three-dimensional printing of piezoelectric materials with designed anisotropy and directional response.” *Nature Materials*, 18 (3), 234, 2019

6. R. M. Hensleigh et al. "Additive Manufacturing of complex micro-architected graphene aerogels." *Materials Horizons*, 5 (6), 1035-1041, 2018
7. H. Cui; R. Hensleigh; et al. "Additive Manufacturing and size-dependent mechanical properties of three-dimensional microarchitected, high-temperature ceramic metamaterials." *Journal of Materials Research*, 33 (3), 2018
8. J. Lewicki, et al. "'3D-Printing of Meso-structurally Ordered Carbon Fiber/Polymer Composites with Unprecedented Orthotropic Physical Properties.'" *Scientific Reports*, 7, 43401, 2017
9. J. Andriolo, R. Hensleigh, et al. "Iron-doped apatite nanoparticles for improvement of phage therapy." *Journal of Vacuum Science & Technology B*, 32 (6), 2014

### **Patents**

- Selective Deposition of Materials for Composite Structures via Additive Manufacturing - International Patent PCT/US2019/033385
- Additive Manufacturing and Design of Piezoelectric Materials with Arbitrary Structure and Response in 3D - International Patent No. PCT/US2019/034065
- Optically enhanced patternable photosensitivity via oxygen excitation - US10668708B2
- Architected three dimensional graphene via additive manufacturing - US20180196345A1
- System and method for stimulated emission depletion projection stereolithography - US20180056603A1

## CHAPTER 1: BACKGROUND AND MOTIVIATION

Additive manufacturing (AM) techniques in general, have been well developed for the fabrication of complex three dimensionally (3D) structures with structural materials (polymer, ceramics and metal) at high nano- and micro-meter resolutions.<sup>1</sup> 3D structured structural materials in the nano- and micro- range have shown interesting properties, including size effects,<sup>1-4</sup> superelasticity,<sup>2</sup> and exceptional stiffness to weight performance.<sup>3</sup>

There has been increasing interest in 3D structuring of functional materials, electronics, piezoelectrics, and energy storage. Studies have indicated that 3D structuring can enable significant increases in energy storage performance,<sup>5</sup> allow isotropic electromagnetic (EM) devices with unnatural properties,<sup>6</sup> and open traditional functional materials, like piezoelectrics, to new phenomena.<sup>7</sup> However, there are few established methods and protocols for AM 3D structuring of these functional materials, particularly in the nano- to micron range where interesting structural phenomena have been previously explored.<sup>1</sup>

A variety of processing challenges prevent high-resolution additive manufacturing techniques, particularly light-based micro-stereolithography (PμSL) and in general 3D printing, from fabricating functional 3D devices. The grand challenges lie in the trade-off between processability (being able to be net-shaped into complex architectures with desirable resolutions) and preserving functionality from their intrinsic functional feedstock. For example, while direct ink writing technique has been recently developed to process functional materials (piezoelectric fibers, carbon fibers etc),<sup>8</sup> it cannot reach the desired micro-scale resolution and three-dimensional feature complexity. While light based technique, including projection stereolithography have particular

advantages in feature fidelity and functional property, the photo-sensitive requirement in the feedstock, make it challenging to incorporate functional materials without sacrificing either feature fidelity or functionality, and this an area remains largely undeveloped.

Traditionally, P $\mu$ SL functional device fabrication relies on polymer-functional particle composites, which creates an array of challenges. For example, to garner high response from these composites, one desires a high particle loading, but this correspondingly increases viscosity and light-absorption making manufacturing difficult or impossible. Another difficulty is in integrating the successfully fabricated 3D printed devices with conventional electronics, including electrodes, wires and other elements. Few methods can easily achieve integrating a conductive element into an arbitrary 3D structure.

A major advance would be the ability to print multi-functional, multi-material feedstock into complex architectures, through which new functionalities and structural properties can be derived with designed 3D topology and feature sizes. To address this problem, I study the formulation, process property relationships, characterizations and applications of multi-functional architected metamaterials.

The goal of this dissertation is to develop new, innovative methods to overcome these challenges to allow P $\mu$ SL, and more broadly 3D printing, fabrication of 3D devices comprised of multiple functional and structural materials. I explore the processing-property relationships of functional nanomaterial resins, piezoelectric, graphene, multi-material synthesis and processing and how they affect P $\mu$ SL processing, viscosity, cure depth, etc. and develop novel strategies to enable 3D printing of all-in-one devices. Additionally, I explore the benefits of P $\mu$ SL processing

on these functional feedstocks, i.e. 3D topology effects, feature size effects, multi-material effects and how they collectively enable direct 3D printing of future material and devices.

The following chapters will breakdown the specific focus of my work. Functional devices can be broadly considered to have three major components. An energy storage component, a functional material component (magnetic, piezoelectric, etc.), and an interconnect/metal-dielectric component. Chapter 2 focuses on 3D printing of graphene materials, which are of significant interest for energy storage applications, but are severely limited in resolution and 3D manufacturing. Chapter 3 focuses on enhancing the performance of polymer composites which are the primary P $\mu$ SL fabrication of functional materials (piezoelectric, magnetics, etc.) Chapter 4 focuses on the use of P $\mu$ SL for high-temperature functional ceramics. P $\mu$ SL can readily fabricate ultra-light structure, which are of significant interest for aerospace applications, but as they are made of polymers, this limits their temperature range severely. Chapter 5 focuses on the development of 3D metal-dielectric which can be used both as a device (antenna, capacitor, etc.) or as an interconnect for 3D devices to traditional 2D hardware.

## References

1. Bauer, J. et al. Nanolattices: An Emerging Class of Mechanical Metamaterials. *Advanced Materials* 29, 1701850 (2017).
2. Meza, L. R., Das, S. & Greer, J. R. Strong, lightweight, and recoverable three-dimensional ceramic nanolattices. *Science* **345**, 1322–1326 (2014).
3. Zheng, X. et al. Ultralight, ultrastiff mechanical metamaterials. *Science* 344, 1373–1377 (2014).
4. Cui, H., Hensleigh, R., Chen, H. & Zheng, X. Additive Manufacturing and size-dependent mechanical properties of three-dimensional microarchitected, high-temperature ceramic metamaterials. *Journal of Materials Research* 33, 360–371 (2018).
5. Braun, P. V. & Cook, J. B. Deterministic Design of Chemistry and Mesostructure in Li-Ion Battery Electrodes. *ACS Nano* **12**, 3060–3064 (2018).
6. Liu, N. *et al.* Three-dimensional photonic metamaterials at optical frequencies. *Nature Materials* **7**, 31–37 (2008).
7. Cui, H. *et al.* Three-dimensional printing of piezoelectric materials with designed anisotropy and directional response. *Nature Materials* **18**, 234 (2019).
8. Lewis, J. A. Direct Ink Writing of 3D Functional Materials. *Advanced Functional Materials* **16**, 2193–2204 (2006).

## CHAPTER 2: 3D PRINTING GRAPHENE AEROGELS FOR ENERGY STORAGE

### 2.1 Introduction

Graphene is a single, two-dimensional (2D) layer of sp<sup>2</sup> bonded atomic carbon. Graphene's high electrical conductivity (8000 S/m)<sup>2</sup> and surface area (2600 m<sup>2</sup>/g)<sup>1</sup> make it an ideal scaffold for batteries and supercapacitors.<sup>4,5</sup> Experimental results have corroborated this, with graphene supercapacitors demonstrating record-breaking performance for carbon-based materials.<sup>6,7</sup> With the continual drive towards ever-higher energy storage performance for cell phones, electric vehicles, spacecraft, etc. there is a continual need to improve upon current energy storage materials and processes.

Recent studies have theoretically<sup>8</sup> and experimentally<sup>9,10</sup> demonstrated the benefits of 3D structures to enhance energy storage performance. By incorporating an interpenetrating 3D architectures, the diffusion length/tortuosity is significantly reduced, and the performance enhanced by as 6-7 times.<sup>8</sup> Beyond this, 3D structuring can have several benefits, including the ability to make free-form structure batteries which may inhabit the left-over space of electronic systems, form structural batteries which act as the casing themselves, and to form conformable or implantable devices for bioelectronics.<sup>10</sup>

Graphene is an excellent choice for all these applications due to its relatively low-toxicity compared to other battery materials, use in tissue-engineering scaffolds, and robust mechanical performance. However, fabricating of 3D-structured graphenes (3DGs) typically results in a sharp degradation of mechanical, electrical, and surface area properties compared to pristine 2D

graphene sheets.<sup>6,7</sup> These degradations arise from the lack of topological control on the orientation, alignment and bonding of the individual graphene sheets in the 3DG foam.<sup>11</sup>

3D printing has alleviated similar problems in polymer materials, but graphene 3D printing is limited to extrusion or templating techniques.<sup>7,11-16</sup> Due to the non-self-supporting nature of graphene extrusion inks and template methods, free-standing 3DGs are limited to large (>100  $\mu\text{m}$ ) features and log-pile-like structures. To achieve the enhancements of advanced 3D energy storage<sup>8</sup> beyond the state-of-the-art,<sup>9,10</sup> new advanced 3DG manufacturing methods are needed to achieve the structural complexity required for interpenetrating electrodes and self-supporting free-form electrodes.

## **2.2 Microarchitected Graphenes for Arbitrary Graphene Structures**

The only light-based AM of graphene foams relied on laser-based decomposition of nickel-sugar powders to create graphene foams in-situ. Fundamentally, this process relies on laser volatilizing the sugar which then templates as graphene on the nickel particles. The heat based nature and large laser spot size has resulted in very large features, millimeters (mms) to centimeters (cms).<sup>17</sup>

High-resolution light-based AM of graphene such as stereolithography (SLA), have never been demonstrated. This chapter focuses on the development of SLA methods for graphene foam production. A discussion of the various attempts at 3DG production by SLA will be presented as we feel these negative results are valuable in ongoing and future 3DG manufacturing work. Following this, a discussion of the initial development of the gel-dispersion method (GDM),

followed by processing-property relationships established to optimize the final material properties.

The SLA-based 3DG methods produces arbitrary 3D structures with features an order-of-magnitude finer than any previous graphene 3D printing method. To capture this complexity, we refer to these 3D printed graphenes as micro-architectured graphenes (MAGs). Optimized MAG processing produce surface areas approaching the state-of-the-art for 3D printed graphenes.

### **2.3 Initial Attempts at Fabricating 3DGs via SLA**

MAG processing is rooted in the works of Worsley et al.<sup>18-20</sup> who closely mentored this work, and reported one of the first graphene aerogels with exceptional properties including high surface area (1300 m<sup>2</sup>/g) and electrical conductivities (100 S/m). Those aerogels are derived from graphene oxide (GO) which is an oxidized form of graphene bearing many chemical functionalities, epoxy, hydroxyl, and carboxyl. In-situ chemical reduction of the epoxy groups by ammonium hydroxide leads to GO crosslinking into hydrogels, which are then supercritically dried to preserve pore structure, and finally thermally reduced to graphene aerogel at 1050 °C under inert atmosphere. MAG developments have focused on replicating the exceptional properties of these aerogels, and so have exclusively focused on GO-based systems.

The critical material requirement of SLA is the incorporation of photopolymer, i.e. acrylic, thiol, etc. monomers to allow near-UV crosslinking. Initial exploratory development of a suitable MAG resin used graphene oxide (GO) dispersed in pure polymer. Due to SLA viscosity limitations (<10 Pa\*s) GO loading was on the order of 10 mg/mL (1wt%). UV-crosslinking of these GO polymer composites followed by thermal reduction matching previous graphene

aerogel treatments was used. Probing the chars by scanning electron microscopy (SEM) revealed a non-porous carbon structure, and this is confirmed by similar reports in the literature.<sup>21</sup>

Several further attempt at using GO dispersed in bulk were also attempted. This includes attempting to crosslink the flakes of GO (FGO) within the cure photopolymer with ammonium hydroxide, reducing FGO with hydroiodic acid (HI), and etching the cure photopolymer while leaving FGO with sodium hydroxide (NaOH). All of these followed by the same inert atmosphere thermal treatment. However, none yielded observably porosity by SEM.

These results indicated that pure acrylate photopolymer would simply always lead to excess carbon filling any void space between the GO sheets and eliminating the desired high-surface area material. It was reasoned that to overcome this, the smallest amount possible of photopolymer should be used. To this end, a simple test was conducted, whereby increasing amounts of photopolymer were added to a standard 10mg/mL dispersion of FGO in N,N-dimethylformamide (DMF). DMF was chosen as it is an excellent solvent for GO, graphene, photopolymers, and photoinitiators.<sup>22</sup> At increasing levels of photopolymer, 6, 8, 12, 16, 20wt% (to DMF) a small sample was removed and cured under UV-light, between two glass slides with a ~100 micron scotch-tape spacer. The slides were separated and if there was only liquid present, i.e. no gelation, the photopolymer amount was increased until gelation was achieved.

An amount of 12wt% (0.12g to 1g DMF) was found to be the minimum possible loading of the photopolymers to achieve gelation. It should be noted the chosen photopolymers were chosen due to their purported ability to crosslink at ultra-low concentration, due to their relatively long backbone lengths. The polymers were polyethyleneglycol diacrylate with a molecular weight (MW) of 700 (PEGDA700) and a bisphenol A ethoxylate dimethacrylate with MW of 1700

(BisA1700) in a 1:1 weight ratio. Resins which used only pure PEGDA700 were weak, swollen with solvent, and could not be dried. Using only BisA1700 resulted in cured gels that were very brittle. The 1:1 weight ratio cured gels appeared relatively strong, yet malleable and so development has focused on this combination.

Initial SEM results indicated this reduced 12wt% polymer FGO dispersion when pyrolyzed produced a porous sample, encouraging further development. It was undertaken to test if the low-polymer loading was compatible with projection micro-SLA (PuSL) fabrication. PuSL is an SLA variant that uses a dynamic photomask to pattern an entire 2D layer in one exposure. Through trial-and-error it was found the resin was compatible with PuSL printing, **Figure 2-1**, with nitrogen purging of oxygen to low (~1%) levels compared to 21% in ambient air using Firefox in-situ oxygen sensor. In ambient oxygen, gelation was never observed, regardless of exposure time. With low-oxygen, relatively long exposure times of 30 to 60s were required, likely due to the low-polymer loading and high visible light absorption of GO (appears black). Using a surface analysis system the Brunauer–Emmett–Teller (BET) surface area of the FGO MAGs was recorded to be 47 m<sup>2</sup>/g significantly lower than Worsley et al. aerogels (1300 m<sup>2</sup>/g) we were targeting.

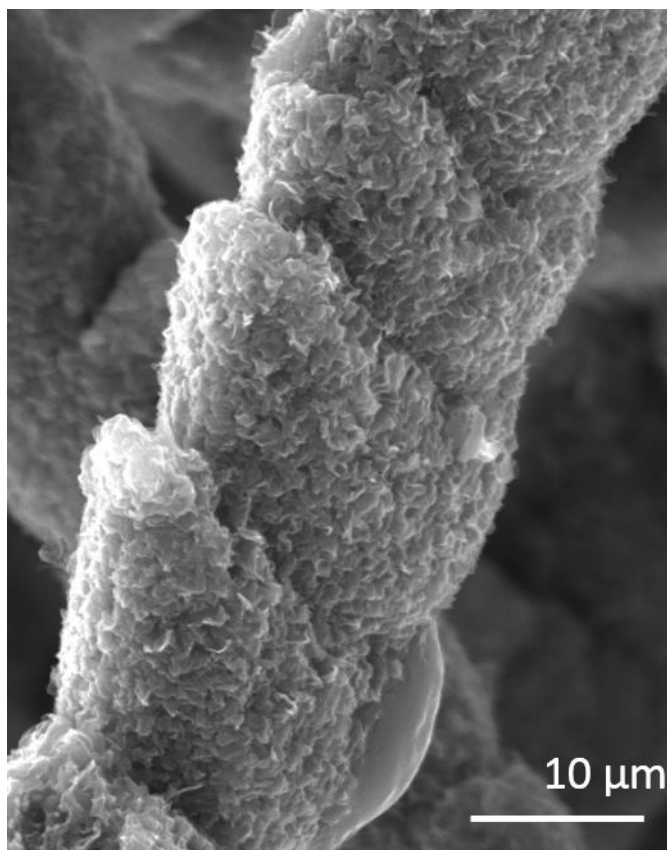


**Figure 2-1: FGO MAG strut showing the small pore structure**

#### **2.4 Gel-Dispersion Method**

The key feature of the Worsley et al. aerogels is the sheet-sheet crosslinking, preventing restacking to preserve surface area of the 2D graphene sheets within the 3D foam. It was reasoned that to achieve high-surface area we would need to replicate this within the photopolymer gels. As earlier tests of crosslinking within the bulk photopolymer had failed, it

was hypothesized that pre-crosslinking the GO aerogel before dispersion into the 12wt% photopolymer DMF organogel would result in an increase of surface area.

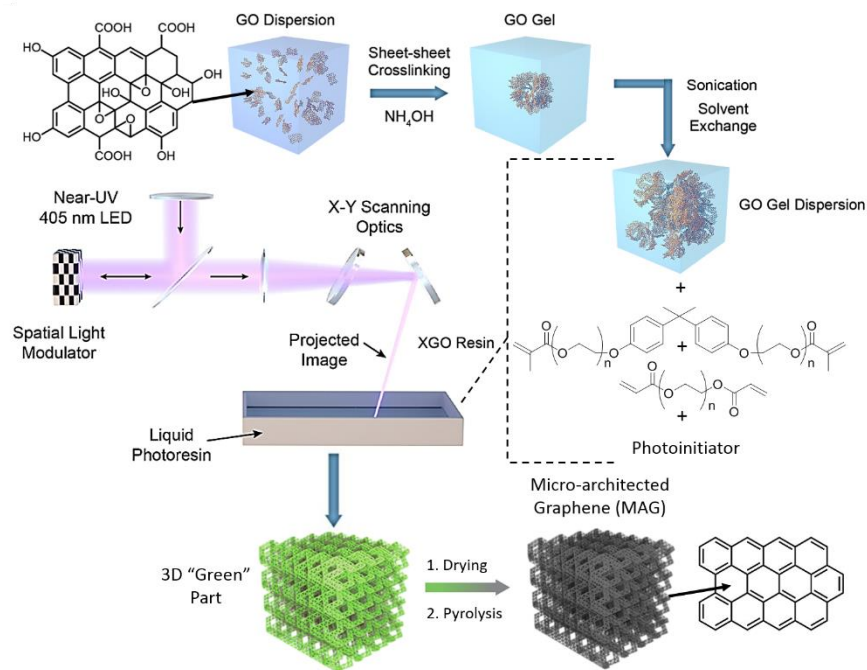


**Figure 2-2: Scheme of MAG resin synthesis.** GO is first crosslinked (XGO) into a hydrogel monolith then dispersed by sonication into a gel fragment dispersion. The addition of acrylates and photoinitiator creates the “XGO resin” and allows PuSL 3D printing, followed by drying and pyrolysis to the final microarchitected graphene (MAG)

**Figure 2-2** depicts the overall resin synthesis beginning with the synthesis of the GO aerogel from Worsley et al. The GO hydrogel is then washed several times with deionize (DI) water to remove excess ammonium hydroxide, then with ethanol, then with DMF. The DMF is added so

that the GO will form a 1wt% solution based on the initial GO weight. The GO hydrogel monolith is then broken up with a chemical spatula to ~1 to 5mm sized pieces and ultra-sonically dispersed this produces a GO hydrogel particle dispersion (referred to as gel-dispersion) where within the GO particles, sheet-sheet crosslinking of the GO preserve the fine pore structure of the Worsley et al. aerogel. Optical light microscopy reveals that after 24 hours of ultra-sonication the GO monolith is thoroughly dispersed with no particles larger than several microns, the resolution limit of PuSL processing, **Figure 2-3**.

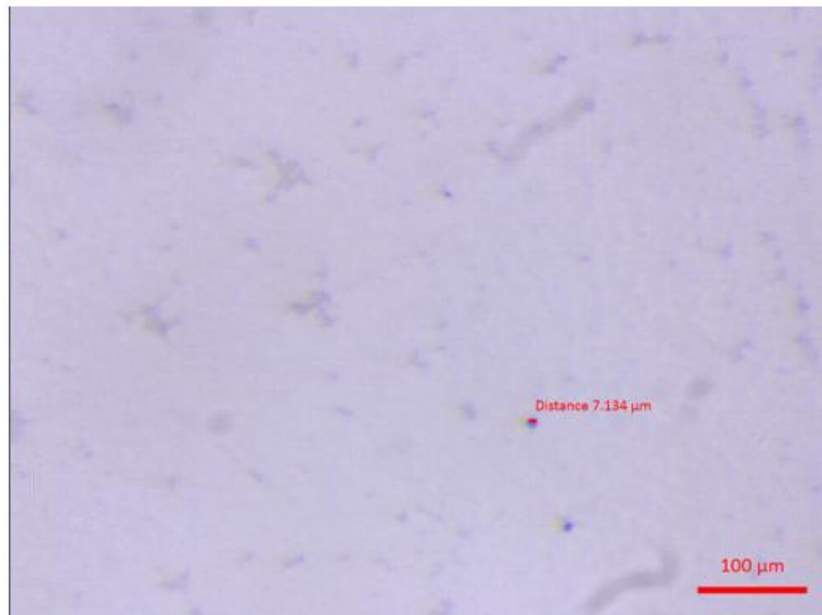


**Figure 2-3: Optical microscopy of GO Gel-Dispersion** showing most of the hydrogel monolith has been broken down into sub 10 micron particles, with a few agglomerations on the order of 10-50 microns.

To this GO gel-dispersion the small (12wt% to DMF) of acrylates (50/50 PEGDA700/BisA1700) are added. After 3D printing/UV-curing of the photopolymer the

structures are dried via supercritical or freeze-drying. These “green” structures are pyrolyzed removing the majority of the photopolymer and reduces the GO green structure into a MAG.

PuSL printing can achieve highly complex MAG structures, **Figure 2-4**, including octet-truss, gyroid, cuboisodecahedrons, and Kelvin foams. As the GO-acrylate DMF organogel is self-supporting, any designed 3D topologies are possible. Shape is preserved after pyrolysis of the green structures, Figure 2-4B shows an optical microscopy image of the pyrolyzed gyroid structure and Figure 2-4C-D show SEM images of the complex curve surface. These are the most advanced 3DGs in terms of 3D topology.<sup>7,18</sup>

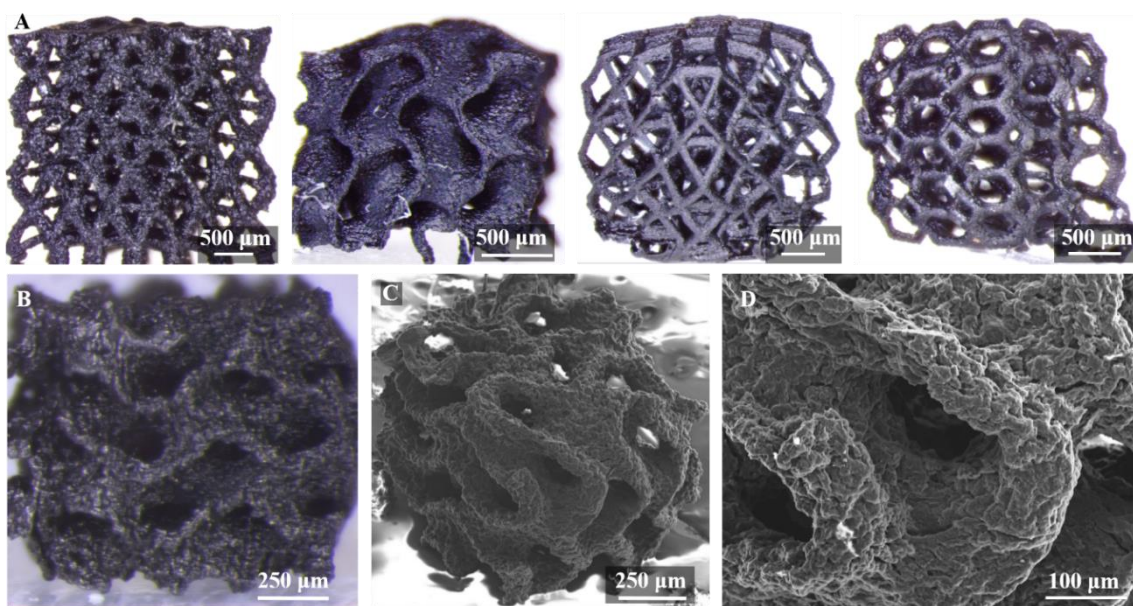


**Figure 2-4. MAG Structures** A) Four "Green" MAG parts of differing unit-cell structures before pyrolysis from left to right octet-truss, gyroid, cubo-octahedron, and Kelvin foam; B) Optical image of pyrolyzed gyroid; C) SEM image of pyrolyzed gyroid with intricate overhang structures D) Zoomed image of pyrolyzed gyroid in "C"

Critically, the gel-dispersed MAGs confirm our hypothesis and show an increase in surface area (147 m<sup>2</sup>/g) compared to the uncrosslinked FGO samples.

## 2.5 MAG Morphology and Composition

The pyrolyzed MAGs shrinkage was investigated for the octet-truss structures, using the overall dimensions and the dimensions of a strut within the structure for “green” lattice before pyrolysis and after pyrolysis. The values are listed in **Table 2-1** shows a 60% shrinkage, ignoring the values in the height column do to lack of sample points. The shrinkage also appears uniform.

**Table 2-1: MAG Shrinkage**

<b>Green Lattice</b>				
<b>Length</b>	<b>width</b>	<b>height</b>	<b>strut diameter</b>	
<b>(<math>\mu\text{m}</math>)</b>	<b>(<math>\mu\text{m}</math>)</b>	<b>(<math>\mu\text{m}</math>)</b>	<b>(<math>\mu\text{m}</math>)</b>	
969.57	971.71	491.53	89.88	
978.93	976.73	626.3	33.56	
906.26	906.18	559	94.43	
900.97	924.69	620.89	66.87	
895.6	915.05	524.68	83.77	
952.87	822.33	533.19	67.31	
<b>average</b>	934.03	919.45	559.27	72.64

	<b>Pyrolyzed Lattice</b>			
	<b>length (<math>\mu\text{m}</math>)</b>	<b>width (<math>\mu\text{m}</math>)</b>	<b>height (<math>\mu\text{m}</math>)</b>	<b>strut diameter (<math>\mu\text{m}</math>)</b>
	407.19	426.52	340.22	30.26
	398.27	386.92		33.64
	388.97	385.68		22.25
	405.4	409.7		33.65
	364.64			36.97
<b>average</b>	392.89	402.21	340.22	31.35
<b>%change</b>	<b>-57.94%</b>	<b>-56.26%</b>	<b>-39.17%</b>	<b>-56.83%</b>

This shrinkage aids in gaining the high-resolution. The ultimate printing/gelling resolution achieved is approximately 20  $\mu\text{m}$ . After pyrolysis this leaves us with the smallest MAG features sizes on the order of 10  $\mu\text{m}$  **Figure 2-5**. This is an order-of-magnitude smaller than extrusion based 3DGs and represents a new state-of-the-art limit.<sup>7,12</sup> The precursor GO (Cheaptubes) is characterized as being single-layer and having a 1-10  $\mu\text{m}$  X-Y diameter. We therefore hypothesize that our process is at the limit of fabrication resolution for these GO sheets, as fabrication resolution cannot be smaller than the printing material.

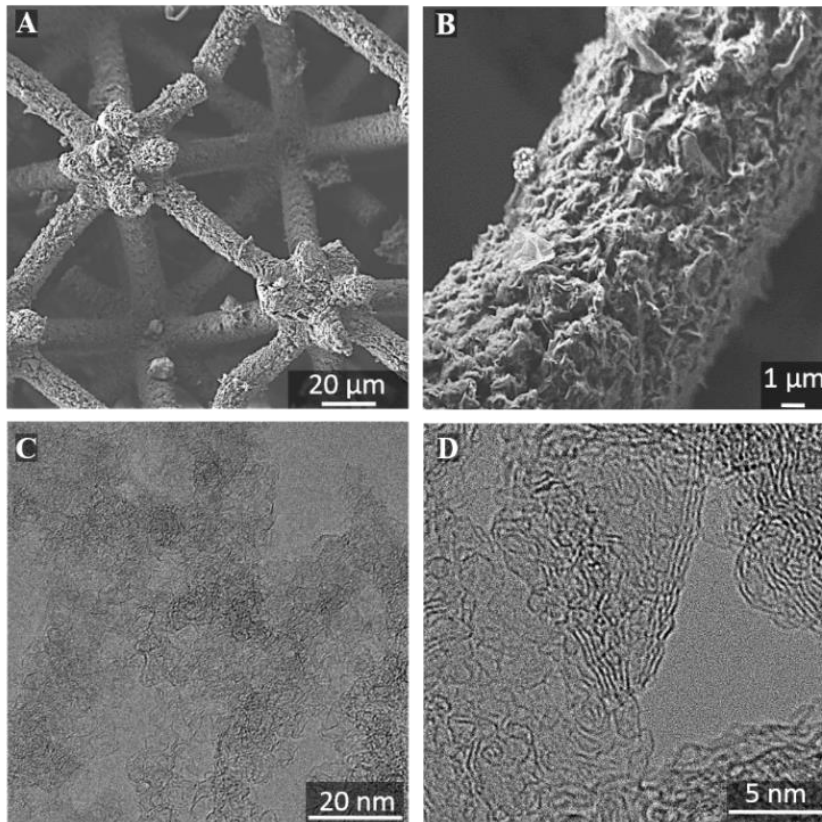


**Figure 2-5: Morphology of MAGs** A) SEM of XGO MAG B) Zoomed SEM of XGO MAG showing porous nature of strut C) TEM of XGO MAG showing sheet wrinkling and imperfect stacking D) Zoomed TEM showing stacking on the order of 4-5 graphene layers

Transmission electron microscopy (TEM) in **Figure 2-5** is very similar to the previous work of Worsley et al., showing wrinkling and some restacking of the sheets on the order of 3-5 layers.<sup>29</sup> This sheet restacking reinforces that the loss of surface area is due to the GO foam collapse during pyrolysis as the sheet-sheet interface becomes inaccessible to the probe gas (nitrogen) used in BET analysis.<sup>28</sup>

Raman Spectroscopy is a very valuable technique for graphene and carbon material analysis. It is possible to note single and multi-layer transitions, and crystallinity of graphene i.e. graphite-like or amorphous. Raman was done on both the traditional Worsley et al. aerogels as a standard and the MAG derived graphenes, **Figure 2-6**. The primary peaks of interest for carbons are, the G band (1582 cm<sup>-1</sup>), D band (1350 cm<sup>-1</sup>), G' band (3248 cm<sup>-1</sup>), and D' band(2700 cm<sup>-1</sup>) bands.<sup>2,20,23-29</sup> The Worsley et al. graphene aerogel matches well with previous reported spectra by Worsley. The key features are the strong, broad G and D band peaks which result from scattering at sheet edges. The MAG derived graphene similarly shows a strong and broad D and G band, indicating a similar microstructure to traditional 3DGs. The lack D' or G' peaks indicates there is low crystallinity, i.e. no graphite-like layers.<sup>2,20,23-29</sup> This indicates our MAG derived aerogels are similar in microstructure to traditional 3DGs, despite the increase in sheet restacking, the sheets are not well-ordered, like graphite in their restacking and likely have some inter-layer pore spacing that is accessible to BET analysis.

The thermal reduction of MAGs was monitored and a “green” MAG gel was compared to the final pyrolyzed MAG. The PEGDA700 and BisA1700 monomers carry significant amounts of oxygen (typical of acrylates). Pyrolysis thermal reduction of GO to graphene critically requires the elimination of oxygen, and the addition of oxygen by the acrylate may interfere with this process, which could lower the final electrical conductivity. SEM energy dispersive X-Ray spectroscopy (SEM-EDX) can detect elemental composition. The “green” MAG showed high-levels (20%) of oxygen from both the GO and acrylate, **Figure 2-6**, similar to levels reported by Worsley et al.<sup>2,19,20</sup> The pyrolyzed MAGs are essentially pure carbon, with only 5% oxygen, also similar to reports by Worsley et al.<sup>2,19,20</sup> The addition of acrylate therefore seems to have little

effect on the final elemental composition and burns out cleanly to give thermally reduced graphene sheets.

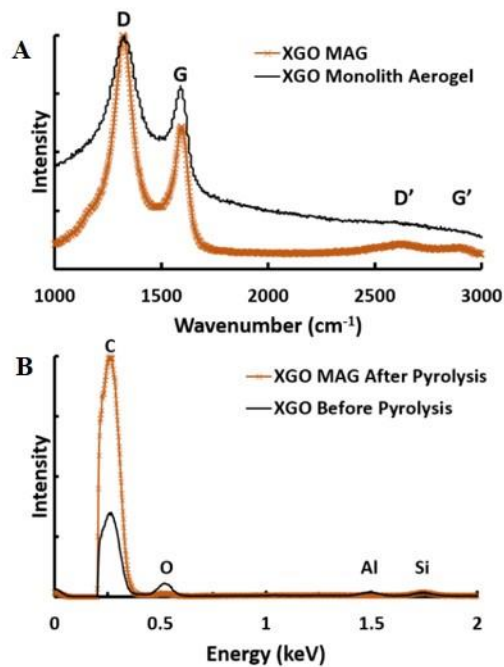


**Figure 2-6: Raman and XRD of MAGs** A) Micro-Raman analysis of XGO MAG and XGO aerogel showing identical MAG aerogel microstructure. B) SEM-EDS of XGO with no polymer before annealing, showing highly oxidized nature, compared to the furnace treated XGO MAGs revealing total loss of acrylate, and GO reduction leaving largely pure graphene network within the MAG struts

## 2.6 MAG Mechanical Properties

One of the key benefits of 3D structuring is its benefits to 3D foams. The mechanical properties of 3D foams is dependent on its underlying microstructure i.e. the interconnectivity of the struts/sheets within the foam. Consider a log-log plot of Young's modulus (E) versus density ( $\rho$ ) of a foam, normalized to the solid base material modulus ( $E_s$ ) and density ( $\rho_s$ ). The material will following scaling relation, where the scaling exponent (n) is used to gauge the severity of degradation.<sup>8</sup>

$$\frac{E}{E_s} \propto \left(\frac{\rho}{\rho_s}\right)^n \quad \text{Equation: (2-1)}$$

The majority of materials show a much greater than linear (n=1) degradation of mechanical properties at lower densities, consider polystyrene foams which degrade with n~2.<sup>10</sup> 3DGs experience extreme mechanical degradation, with n~2.73, meaning that despite pristine graphene having orders-of-magnitude higher E than polystyrene, foams of polystyrene will outperform 3DGs at low-density.<sup>10</sup>

This poor mechanical performance at low-density is concerning as graphene, and other nanocarbons, are regularly used as current-collectors within energy storage systems. Ideally the current collector density/wt% within the energy storage system will be as small as possible i.e. low density, but it often is responsible for maintain the mechanical properties of the energy storage system. Batteries can experience extreme swelling with cycling, on the order of 400%,<sup>45</sup> and the inability to predictably control 3DG's mechanical properties is a concerning limitation. 3DGs mechanical properties can only currently be trial-and-error changes in 3DGs foam processing i.e. changes in reducing agent, time, temperature, etc. To maintain superelastic properties, 3DGs are often either composited with polymers or other materials, or not fully

reduced i.e. only processed to low temperature (<400 °C) which leaves oxygen moieties from the GO precursor; both methods lower the electrical conductivity and limit the electrode performance.

AM has demonstrated that controlling the microstructure of polymer foams, one can achieve near linear ( $n \sim 1.1$ ) scaling. Using other so-called micro-architectures, such as the pyramidal lattice structure, can achieve high scaling ( $n \sim 2$ ) if less-stiff materials are desired. This tunability by altering the micro-architecture is a predictable process and could have significant benefits to 3DGs.<sup>8</sup> While previous graphene 3D printing methods could not achieve the fabrication complexity required, our MAG processing is capable.

The octet-truss is an open-foam micro-architecture previously used to achieve near linear scaling in 3D printed polymers.<sup>8</sup> A range of MAG octet-truss were fabricated with 9-42% relative density ( $\frac{\rho}{\rho_s}$ ), and two pyramidal micro-architected MAGs were fabricated using the previously described methods. Compression testing (Instron, 10 kN cell) was used to analyze their stiffness and they were compared to literature reported 3DGs. The results are shown in **Figure 2-7**.

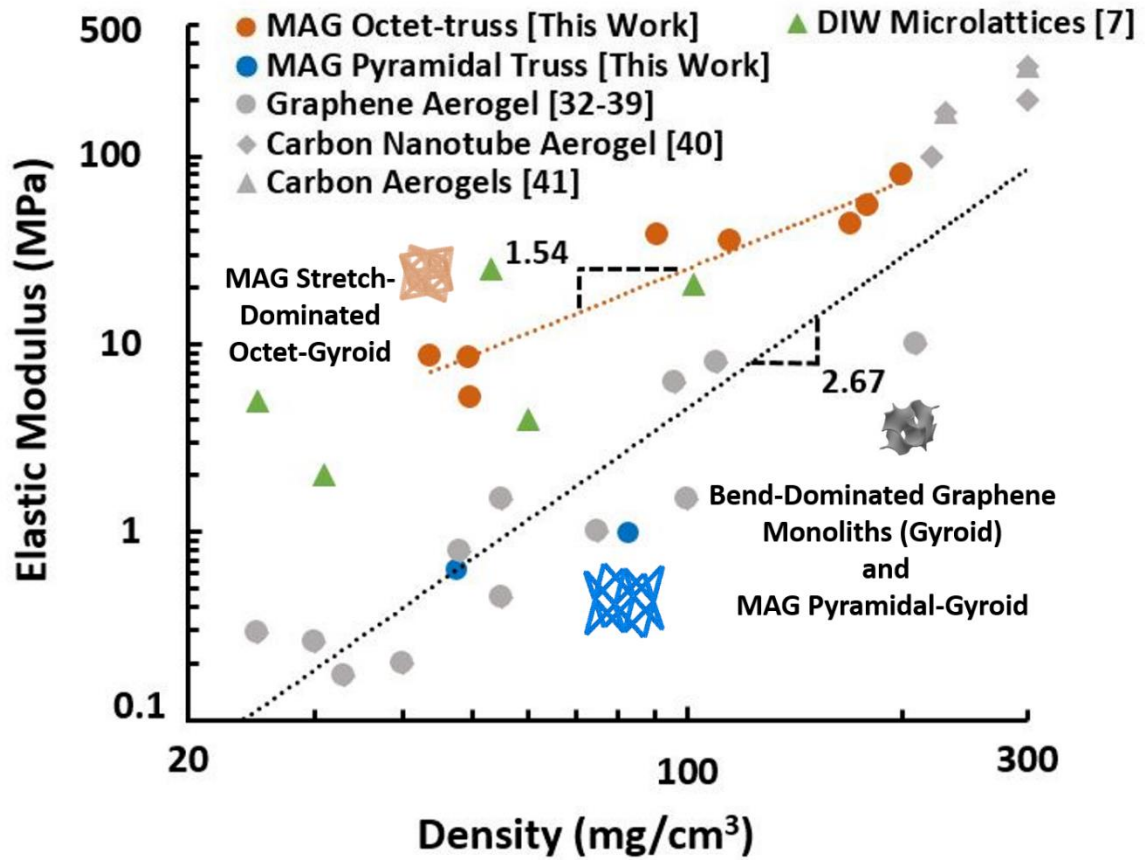


**Figure 2-7: Mechanical Properties MAGs** a) Elastic modulus versus density for MAG octet-truss (orange), MAG pyramidal truss (blue), and several previously reported graphene aerogels and 3D printed graphenes

Work by Qin et al. establishes that 3DGs can be modelled as being mechanically similar to that of gyroids.<sup>10</sup> Therefore, MAGs must be considered a hierarchical structure, **Figure 2-8**, with the macro-structure chosen by the 3D printed design, and within the lattice struts the graphene foam modelled as a gyroid. Hierarchical lattice foams have properties, which depend on both the constitutive structures.<sup>6</sup>

Their behavior can be modelled by modification of **Equation 2-1** reported by Zheng et al. and modified by my colleagues Huachen Cui and Desheng Yao. The following equation (2-2):

$$E/E_s \sim (\bar{\rho})^{\alpha N_1 + (1-\alpha)N_2} \quad \text{Equation: (2-2)}$$

where  $N_1$  is the scaling factor of gyroid (2.73),  $N_2$  is the scaling factor of the octet-truss (1.1), and  $\bar{\rho}$  is the overall density of the 3D MAG.  $\alpha$  represents the variation of the gyroid relative density to the overall density i.e. when varying the MAG density from 9-42%, this is designed as variation in the octet-truss density, however as the gyroid density is not strictly controlled,  $\alpha$  accounts for variation in its density.<sup>6,31</sup> If in varying the density ( $\bar{\rho}$ ) of the 3D MAGs the gyroid density remains constant ( $\alpha=0$ ), then the scaling of the 3D MAG will that of the octet-truss (1.1).

The octet-truss MAGs exhibit a scaling factor of  $n=1.56$ , **Figure 2-7**. This is significantly improved compared to unstructured 3DGs<sup>32-39</sup> carbon nanotube aerogels (CNT),<sup>40</sup> and carbon aerogels<sup>41</sup> all of which have a similar scaling to gyroid  $n\sim 2.67$ . Our MAG octet-truss also outperform the previously reported state-of-the-art 3D printed graphenes, by Cheng et al. had a scaling of  $n=2.5$  (Green triangles Figure 2-7).<sup>10</sup>

We can simultaneously demonstrate mechanical tunability and reinforce that the improved scaling is due to underlying microstructure by comparing the octet-truss MAGs to the MAG structured as pyramidal lattice ( $n=2$ ). Pyramidal MAGs are significantly less stiff than octet-truss MAGs despite similar densities. Between the pyramidal and octet-truss MAGs, we can achieve an order-of-magnitude range in elastic modulus tunability.

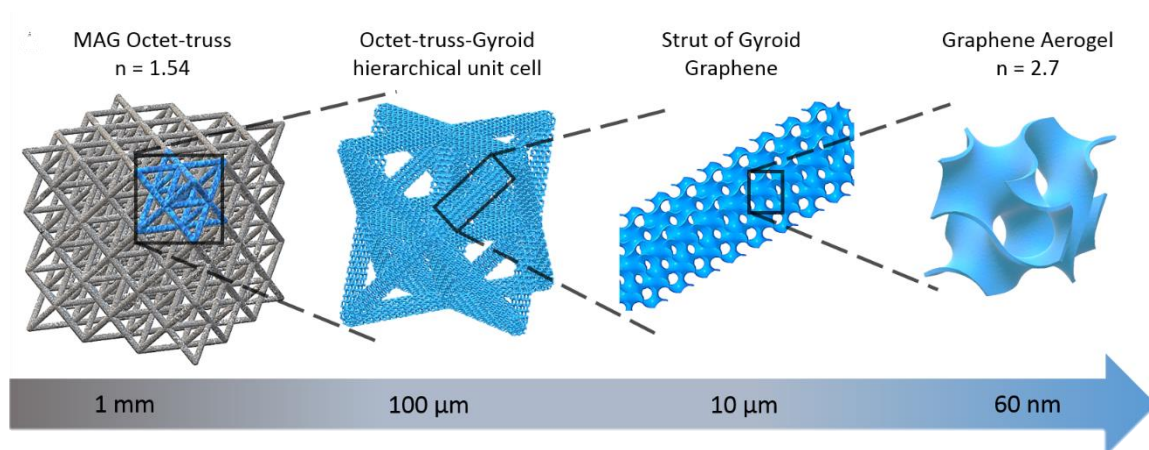


**Figure 2-8: Hierarchical Structure MAGs** A) MAGs consist of a hierarchical structure with the overall chosen 3D printed structure (in this case octet-truss) being the larger macro-structure, and the graphene foam being the finer microstructure in the struts represented by a gyroid

## 2.7 Electrical Properties

The electrical conductivity of octet-truss MAGs was probed by simple ohm-meter resistive testing. Placing needle probes on either end of the structure, measuring the resistance, and then dividing by the height of the structure. An electrical conductivity of 64 S/m for a MAG density of 92 mg/cm<sup>3</sup> was found. Worsley et al. base 3DGs conductivity is 100 S/m, indicating there is some loss of interconnectivity of the sheets, but compared to previous literature, MAGs are equivalent in their conductivity. Improvements could be had with higher furnace treatment temperature but likely at a loss of surface area.<sup>29</sup>

## 2.8 Formulation Optimization

The previous sections have all focused on characterization of the initial MAG resin formulation. That is, a Worsley et al. graphene hydrogel, exchanged with DMF, sonicated for 12-24 hours to form a 1wt% (to DMF) GO particle dispersion, with 6wt% (to DMF) PEGDA700, 6wt% BisA1700, and 4wt% Irgacure 819. After photocuring, supercritical CO<sub>2</sub> or freeze-drying followed by furnace treatment at 2 °C/min up to 1050 °C, holding for 3 hours, then 2 °C/min cooling.

This process represents a significant advancement in 3DG processing, particularly the ability to free-form pattern complex 3D graphene with high electrical conductivity (64 S/m), fine 10 micron feature resolution, and essentially any desired structure. There are still significant drawbacks to applying our MAGs to practical applications in 3D energy storage. Particularly, the relatively low surface area (140 m<sup>2</sup>/g) compared to similar aerogels, the small footprint (~5mmx5mm) of our parts, and the overall strength of the materials which is quite brittle (<1% ultimate strain).

There are several important processing questions to consider in MAG resin synthesis. To the author's knowledge, there have been no reports exploring processing-property relationships of such a gel-dispersion technique. An exploration of these properties was undertaken, focusing on each step of the resin synthesis scheme, **Figure 2-2** with a focus of understanding the effects on each step on final MAG properties, particularly with an aim to improve surface, area, printability, and strength.

## **2.9 Critical Point Drying Versus Ambient**

Aerogel processing has long been hampered by the requirement for critical point drying e.g. supercritical or freeze-drying. This requirement is due to the capillary effect during evaporation causing pore collapse and loss of surface area. These drying techniques are highly specialized, time consuming, and not practical for scale-up. Several reports in recent years have noted that with sufficiently strong porous material or carefully chosen solvents ambient drying is possible. It has been suspected from the beginning that our gel-dispersion method would not require critical point drying; however, an early test yielded low to no surface area when air-dried versus  $140 \text{ m}^2/\text{g}$  when supercritical or freeze-dried. As will be detailed in the following sections several modifications were found to improve the MAG processing including more robust gels and ambient drying was again tested.

The results indicate that ambient drying is effective and can be used. The following sections will exclusively use ambient drying due to its convenience and the highest reported ambiently-dried surface areas ( $846 \text{ m}^2/\text{g}$ ) are equivalent to those found using freeze-drying ( $787 \text{ m}^2/\text{g}$ ). The ambient drying procedure is to simply wash the cured part several times in ethanol, then with water several times, then allowed to dry under gentle heating ( $\sim 60\text{-}80 \text{ }^\circ\text{C}$ ) overnight. This saves a significant amount of time and cost in MAG processing.

## **2.10 Sonication Effects**

A major focus was put on the sonication/breakup of the graphene oxide monolith i.e. the gel-dispersion procedure. As a significant surface area was only noted in the gel-dispersed samples, it is hypothesized that the crosslinked GO particles survive composite pyrolysis to form the pores

in the final MAG structure. The size and quality of these dispersed crosslinked particles, which are created by sonication of the monolith, seem of primary importance to the final texture and surface area properties of the final MAG. Reports have indicated that sonication does lead to GO sheet breakdown.

Previously, a sonication time of 16 hours was used, leading to a surface area of (140 m<sup>2</sup>/g). A series of tests was conducted where, with a fixed polymer loading (at 20wt% as will be discussed in the next section), the sonication time was increased. The results are reported in Figure 2-9.

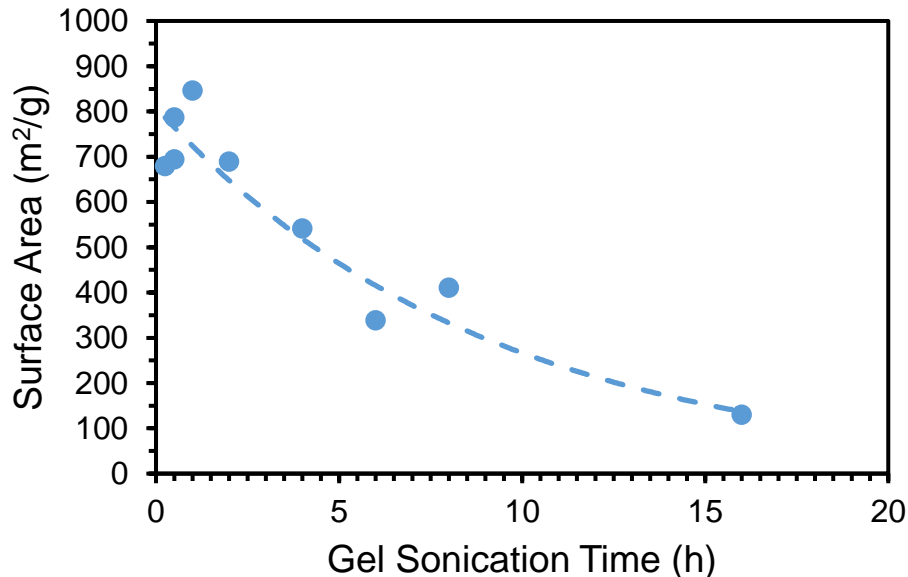


**Figure 2-9: Sonication Effects MAG Surface Area A)** As the sonication time is increased there is a clear drop-off in surface area

The results clearly indicate that increasing sonication time leads to loss of surface area. Critically, with short sonication times of 30min to 1 hour, surface area is significantly higher

with highest tested (846 m<sup>2</sup>/g) which is approaching the state-of-the-art (Cheng et al. 704 to 1066 m<sup>2</sup>/g). Based on these results it is hypothesized that the dispersed XGO particle size is critical. As each particle contains pores within it, excessive sonication leads to GO sheet breakdown, smaller particles, and the loss of these pores, and hence surface area, in the final structure.

To further confirm this a Worsley et al. aerogel was made using smaller initial flake sizes. Typically, a 1-20 micron X-Y diameter average GO flake size is used. When a 300 to 800 nanometer (nm) GO flake size (same supplier, Cheaptubes) was used to make MAG resin, we saw a significant drop in surface area to 237 m<sup>2</sup>/g despite the same formulation and processing parameters including short sonication time (30min).

An additional test was done using large initial XGO flakes (1-20 μm X-Y). Typically, to make the Worsley et al. gel the commercially purchased GO powder is mixed with DI water and sonicated for 12-24 hours before being used to crosslink into GO hydrogels. As sonication has been established as important in breaking down these crosslinked GO hydrogels, it was tested whether excessive sonication in the initial dispersion of GO powder in to DI can be detrimental to surface area. Only a single test was completed, sonicating the GO powder in DI water for 60 hours, and completing the processing with same loading of polymer and other processing parameters as has been discussed. There is a significant drop to nearly no surface area (23 m<sup>2</sup>/g). Sonication breakdown of GO sheets has been noted in literature, and this further indicates that the GO sheet size and XGO particle size are critical to achieving high surface area in the final MAG.

## 2.11 Polymer Loading Effects

The initial MAG resin used as little polymer as possible, with the hypothesis that excess polymer leads to excess carbon and decreased surface area as we had seen many samples filled with excess carbon using bulk polymer. However, the MAG resin printability is limited by this low polymer loading, requiring very low oxygen atmosphere (~0.01%) and long exposure times (30s to 2min) relative to other PuSL resins.

A series of samples with increasing polymer loading, from the standard 12wt% to 40wt% using the same ratio and type of polymer were processed exactly the same, except with the short sonication time of 30min. The results are in **Figure 2-10**.

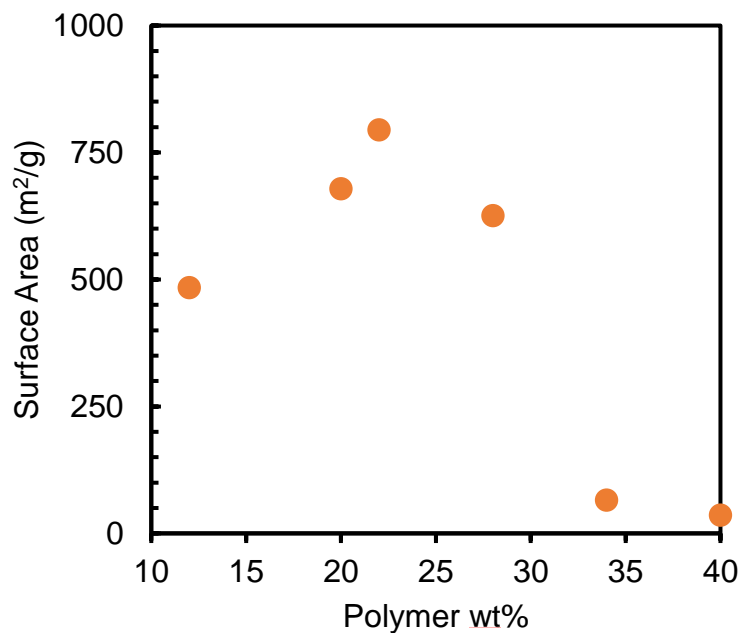


**Figure 2-10: Polymer Loading Effect MAG Surface Area** – There is a clear effect of polymer loading, and high surface area peaks around 22wt% polymer loading.

We find there is an optimum polymer loading of 22wt%. This polymer loading has a clear increase in surface area compared to others at (795 m<sup>2</sup>/g). Previously, we observed SEM images that indicated polymer loadings at this level would lead to no appreciable surface area. While other reports which use neat acrylate show obvious excessive carbon,<sup>22</sup> loadings below 30wt% still show clear porosity and surface area. The underlying mechanism why 22wt% polymer loading leads to high surface area is under investigation. It is hypothesized that during pyrolysis, polymer burnoff leads to gas release, which prevents pore collapse and graphene sheet restacking leading to loss of surface area. Excessive polymer leads to excessive carbon, while too little polymer gives off too little gas to prevent graphene sheet restacking.

## **2.12 MAG Solvent and Furnace Optimization**

The solvent used in the initial MAG system was DMF, which has been studied for years as possible carcinogen, its effects on pregnant women, and is not recommended for general use if can be avoided. During PuSL printing, it was also noted that DMF underwent significant evaporation, **Figure 2-11**, during normal printing (1 L/min N<sub>2</sub> flow) and ambient (0 L/min N<sub>2</sub> flow). Over a 3 hour time, which is typical printing time for a complex structure with the MAG resin, over 0.5 grams of solvent evaporated out of an estimated 10g total bath. Such a significant variance of the GO, polymer, and initiator loading is enough to significantly vary the printing/curing times between builds, making the process impossible to accurately replicate each printing cycle and likely affecting part quality significantly.

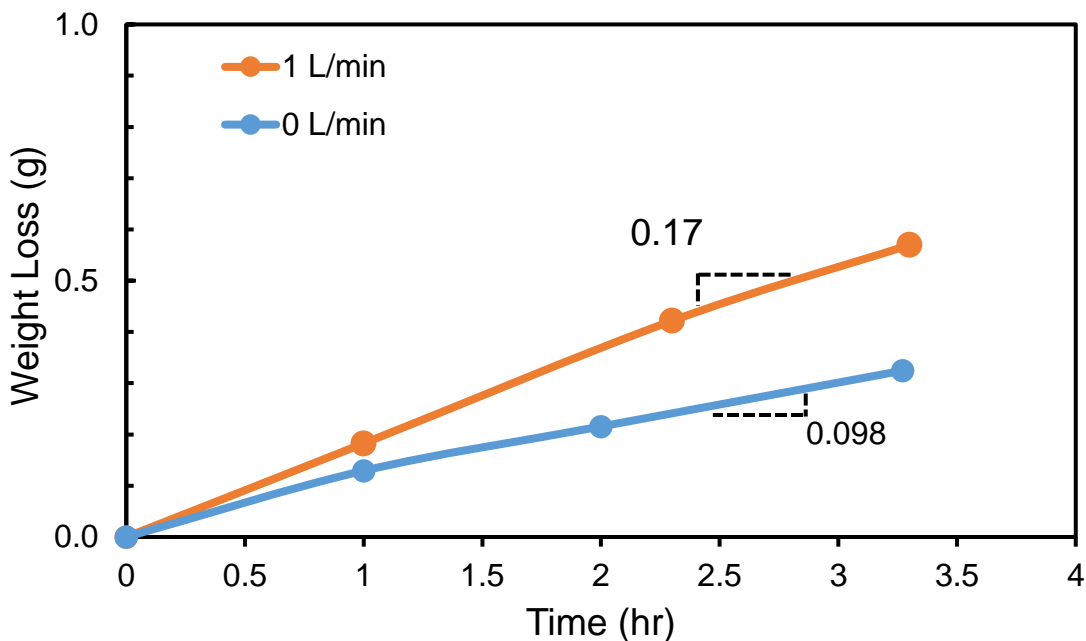


**Figure 2-11: DMF Evaporation** – This chart monitors the evaporation of DMF from MAG resin under ambient (0 L/min) and normal printing operations (1 L/min) nitrogen flow

The relatively high vapor pressure 2.7 mm\*Hg, particularly with the flowing nitrogen setup, of DMF is the fundamental source of this evaporation, and so it would be desirable to find a less volatile solvent.

For plausible scale-up, increasing processing safety, and resin stability, different solvents were explored to replace DMF. DMF was chosen as it the best solvent for graphene sheets as reported by Paredes et al.,<sup>21</sup> and it can dissolve the photopolymer and photoinitiators to make a homogenous MAG resin. Water is an excellent solvent for GO, however, cannot dissolve the photopolymer and initiator adequately. Water-soluble initiators such as lithium-TPO salt

(Colorado Photopolymer Solutions) induced gelation of the GO, which has been observed for other metal salts, and so water as a solvent was not pursued though with a new initiator it may be possible. Paredes et al. indicates that N-methyl-2-pyrrolidone (NMP), tetrahydrofuran (THF), and ethylene glycol (EG) are also excellent solvents, and based on their hydrophobicity, should also dissolve photopolymer and initiator.<sup>21</sup> Based on ambient temperature vapor pressure values reported by Sigma-Aldrich, NMP (0.29 mm\*Hg), and EG (0.08 mm\*Hg) were chosen to be tested as they should have low evaporation relative to DMF (2.7 mm\*Hg), while THF (143 mm\*hg) greater.

Dispersing a 1wt% GO hydrogel into NMP and EG, and left for 24 hours, we observed no obvious sedimentation. However, the EG did possess a sheer-thinning viscoelastic quality, appearing as a gel until shaken. This could prove useful in formulating an extrusion ink, but is not desirable for PuSL processing which requires low (<10 Pa\*S) viscosity. The NMP dispersion appeared stable (no obvious sedimentation) and low viscosity by eye making it an excellent solvent for low evaporation and improved safety.

### **2.13 Furnace Treatment Optimization**

The furnace treatment of MAG structures is based on previous report of Worsley et al. of 2 °C/min to 1050 °C, holding for 3 hours, then cooling at 2 °C/min to room temperature. This near 20 hour process is not desirable for application and scale-up of MAG structures. The slow process is chosen to minimize rapid pyrolysis of the acrylate polymer and allow the GO to reduce and undergo sheet-sheet bonding to maintain high surface area. A study of the thermal processing of GO was undertaken to optimize the process for shorter time while maximizing

surface area. Thermogravimetric analysis (TGA) monitors weight loss with time or temperature during pyrolysis under various atmospheres. **Figure 2-12**, shows a TGA spectrum of the MAG “green” structure under nitrogen atmosphere ramping at 10 °C/min to 1000 °C (limit of TGA system), of the pure as-purchased GO, and also of the acrylic polymer with no GO but with an equivalent amount of DMF and initiator and both treated the same.

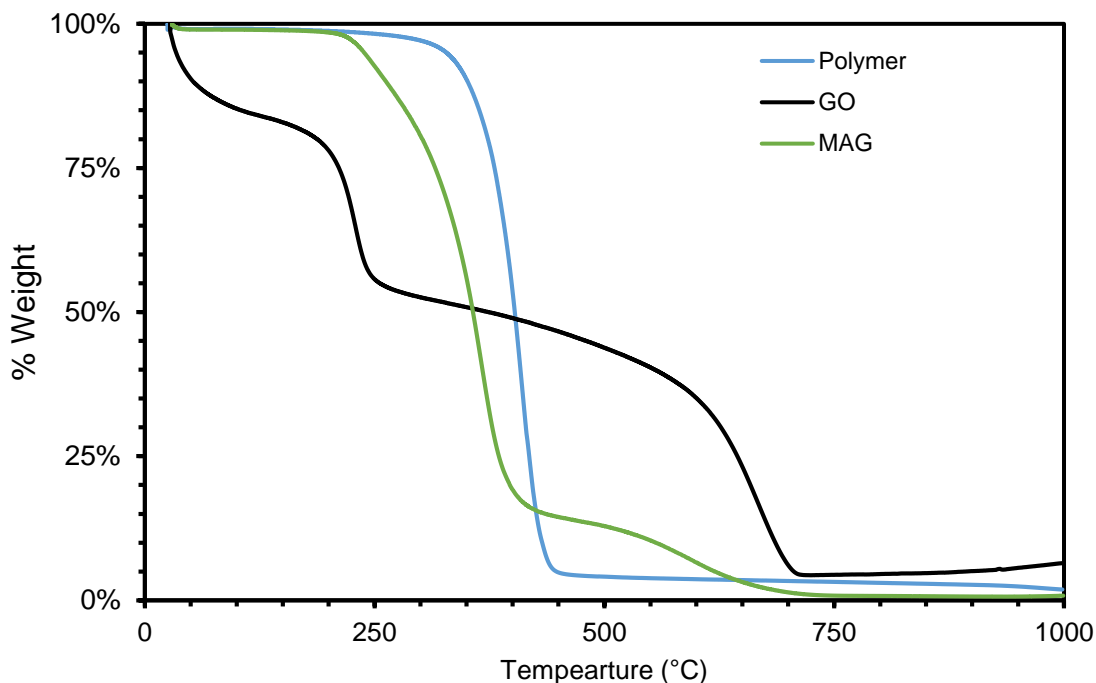


**Figure 2-12: TGA Polymer, GO and MAG** – Weight loss with temperature under nitrogen atmosphere for green MAG, MAG polymer with no GO, and pure as-purchased GO

TGA reveals there is one large 90% drop in weight for the polymer, occurring in the 300 to 450 °C range. The MAG resin sees a similar significant drop of ~80% of its weight from 225 °C to 425 °C while the GO experiences several small drops in weight loss of various deoxygenations.<sup>57</sup> The majority of the weight loss, and therefore texturization of the MAG

occurs over a short range in temperature (175 °C) and time (0.5 – 2 hours) of the very long 37 hours furnace treatment. We therefore hypothesize that, the very slow treatment is not necessary, and that only slow (2 °C/min) furnace ramp rates are required over this small temperature window. Hypothetically it may be possible to enhance surface area if a much slower burnout of polymer is used, reducing the chances for pore collapse by giving GO sheets more time to “find” each other and fuse together.

A series of TGA tests was then performed to determine the optimum hold temperature to allow a slow burnout of 2 hours that would give a slow loss in weight. The TGA was set to rapidly rise (10 °C/min) and hold at set temperatures in the 300 °C to 400 °C range, and the results are in **Figure 2-13**.

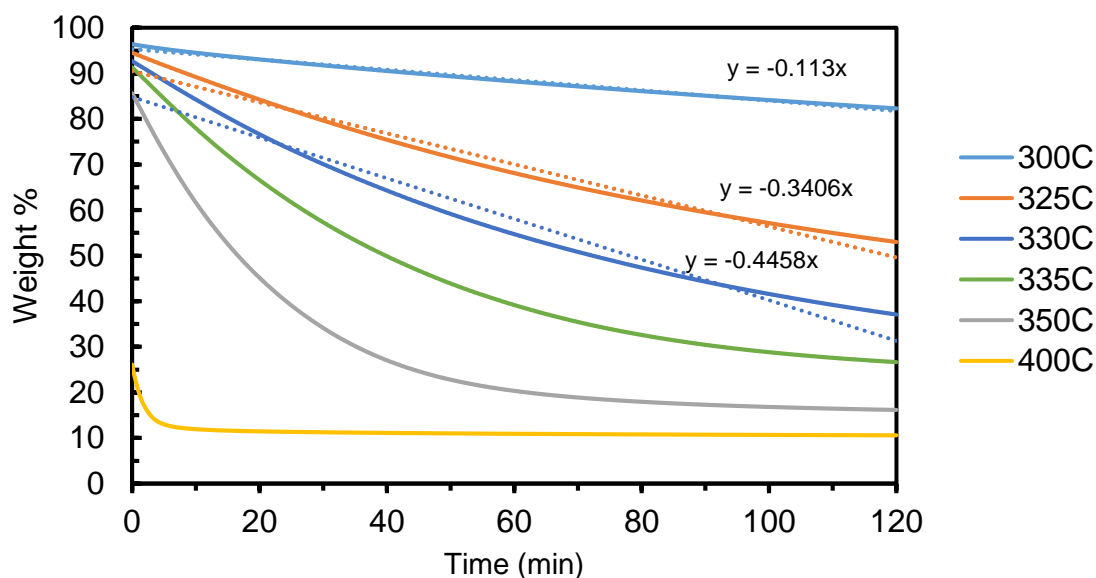


**Figure 2-13: MAG Weight Loss at Fixed Temperatures** – Holding green MAG structures at various temperatures and monitoring the rate of weight loss

The results show that holding at lower temperature (300-330 °C) we see an approximately linear weight loss of the 2 hour hold time. From 330 to 400 °C we see a more exponential drop in weight. The 400 °C curve begins at approximately 25wt% of the original, indicating pyrolysis is nearly complete by the time experimental monitoring begins. For the 300, 325, and 330 °C curves, a linear fitting was used to determine the rate of weight loss which varied from .11%/min to .45%/min.

In the typical processing the green MAG undergoes a ~80% weight loss over 200 °C, which (at 2 °C/min) is a rate of 0.8%/min. Therefore, a holding temperature at 330 °C with a weight loss of 0.45%/min over 2 hours is significantly slower at nearly half the rate. We therefore propose an optimized furnace run, to achieve similar results or enhanced to original MAG processing over this critical temperature range, but before and after using a much faster 10 °C/min ramp rate, to save time, **Figure 2-14**. This reduces the overall time from 20 hours for typical MAG processing to 8 hours.

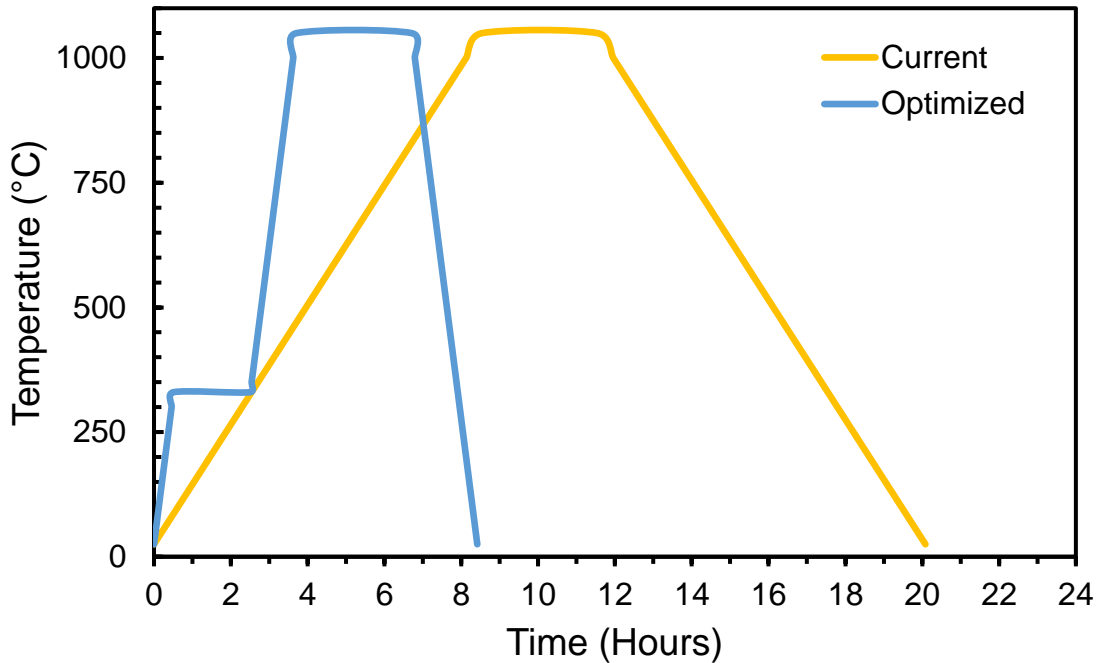


**Figure 2-14: Optimized Furnace Run** – Typical furnace run graphically shown, approximately 20 hours total, and optimized run 8 hours total

Surface area analysis of the optimized furnace run results in a surface area of 695 m<sup>2</sup>/g which is within the range of previous samples using the standard furnace run. This optimized furnace treatment maintains similar surface area and can save time. The hypothesis of improved surface area from the slower polymer burnout rate appears false.

### 2.14 Optimizing Strength MAG

While 3D structuring does allow tunability of mechanical stiffness, **Figure 2-7**, the underlying MAG base-material property is quite brittle, in a typical case completely collapse

beyond 0.1% strain. The Worsley et al. methods MAGs are based upon also suffer from low strain, though MAGs are even lower.<sup>2,19</sup>

3DGs are renowned for their high-strain, up to 80% even at cryogenic temperatures.<sup>46</sup> A review of the literature for high strain 3DGs reveals several key factors, typically high-strain is only accomplished with freeze-drying methods, low-temperature thermal treatment, typically less than 400 °C.<sup>47,48</sup> This leads to incomplete reduction of the GO sheets, and likely incompletely combustion of incorporated polymers or other additives. While this allows high strain in the 3DGs, this leads relatively low electrical conductivity, less than 10 S/cm, and low surface-area, both undesirable for energy storage.<sup>49</sup>

Of the ones that are pyrolyzed to high-temperature, there seem to be two distinct methods to achieve high-elasticity. One method uses elaborate synthesis processes, a mix of hydrothermal, freeze-drying, and chemical reduction, to achieve arch-like structures, some with negative Poisson's ratio, which maintains high strain after annealing at high temperature, 800-1000 °C.<sup>50-53</sup> The other method is to use polymer additives, which form graphitic carbon sheets between the graphene after high-temperature pyrolysis.<sup>49,54</sup> The first methods using freeze-based methods are elaborate, time consuming, and freeze-drying results in very low surface area (<100 m<sup>2</sup>/g). In contrast, the polymer methods are straightforward, and achieve high surface area and electrical conductivity. Both methods were pursued to improve the strength of MAGs.

We first replicated the work of Zhang et al.<sup>50</sup> which uses a hydrothermal treatment to form a 3DG with various reducing chemicals, cleaned with several solvent exchanges, and then symmetrically frozen in water (by suspending in freezer). The freezer temperature was -20 °C instead of Zhang et al. – 80 °C. From here, the process is modified to incorporate it into the

MAG processing. The symmetrically frozen monolith is slowly thawed to room temperature, exchanged with ethanol, then DMF to form a 1wt% solution, broken with a spatula, and sonicated for 1 hour, similar to the Worsley et al. monolith. A 20wt% loading of polymer in the 50/50 wt/wt ratio of PEGDA700/BisA1700 was added, just as used for regular MAGs, but instead of 4wt% photoinitiator, 2wt% of a thermal initiator, Azobisisobutyronitrile (AIBN), was used. 2mL of the Zhang et al. resin was then thermally cured at 80 °C overnight. The structure was pyrolyzed similar to the Worsley et al. MAG, which is very similar to the Zhang et al. procedure, however the monolithic gel did not survive to produce a monolith 3DG. What small pieces of 3DG survived appear quite brittle and no more work was pursued on using the Zhang et al. or other freeze-based 3DG method for improving MAG strain. It is hypothesized that the reduction of GO during the hydrothermal step, leads to poor inter-sheet crosslinking, and this lead to the subsequent collapse of the structure during pyrolysis.

Polymer-based methods to improve strength of MAGs were also explored. The fundamental method is to add polymer additives, which convert to graphitic carbon sheets, which will bridge the graphenes sheets. Polyacrylonitrile (PAN) is a well-known polymer used as a carbon fiber precursor and has been used to enhance mechanical properties of CNT aerogels by fusing them together with graphene-like sheets.<sup>54</sup> Polyamic acid (PAA) which is a precursor to poly(imide), was used by Liu et al. to synthesize superelastic 3DGs with up to 70% strain and very high electrical conductivity ( $> 1000$  S/m) after thermal reduction at temperatures much higher than most 3DG papers, 2800 °C.<sup>49</sup> Liu et al. relies on a freeze-dry method, which likely results in low surface (which they do not report), so it is unclear if the benefits of their methods will translate when combined with the Worsley et al. chemically reduced 3DGs.

The focus was put on the Liu et al. PAA method as work by Herzberger et al. demonstrated a PAA resin formulated for SLA fabrication, making it easily combined with MAG processing.<sup>55</sup> The PAA is dispersed with a positively charged monomer, 2-(dimethylamino)ethyl methacrylate (DMAEMA), which may help assemble the PAA between the dispersed GO particles which have remnant, negative carboxyl functionality.<sup>56</sup>

A series of MAG resins was made with 60min sonicated Worsley et al. GO organogel in DMF, with 20wt% PEGDA700 and BisA1700 in a 50/50 by weight ratio, and 2wt% thermal initiator. A PAA resin was made based on Herzeberger et al. combining 28.12g of 15-16wt% PAA in NMP (Sigma-Aldrich) and 1.735g DMAEMA and stirring overnight. Liu et al. found that low loadings, 1 to 2wt% to the solvent, of PAA resulted in highest strain as this minimizes excess graphitic layers. With the approximately 14wt% PAA-DMAEMA resin, we added 0.1, 0.2g, 0.3g, and 0.4g (0.7wt% to 28wt% PAA) to the 2g MAG resins and thermally cured at 80 °C overnight. The green gels were washed with ethanol several times, then water several times and dried in air at 100 °C overnight. These were pyrolyzed using the typical furnace methods of 2 °C/min to 1050 °C, holding 3h, then cooling at 2 °C/min.

The resulting monoliths were still highly brittle in nature, and showed no obvious mechanical difference from the typical MAG structures. The densities of the samples varied from 354 to 494 mg/mL, which is similar to the XGO MAG cube at 469 mg/mL reported in the Materials Horizons paper reference 58. It is suspected that the acrylate network interferes with the PAA carbonization and bridging of the GO particles during pyrolysis. Possibly the acrylate or its degradation products has some cross reaction with the PAA, it is not clear. Further work in this area should be pursued.

## **2.15 Summary and Future Work**

The fabrication of graphene aerogels via light-based additive manufacturing was accomplished for the first time. Resolutions an order-of-magnitude finer (10 micron), and surface areas approaching the state-of-the-art for 3D printed graphenes (>800 m<sup>2</sup>/g) were demonstrated. The mechanical performance at decreasing density was explored, and 3D structure can enhance the hierarchical response compared to traditional monolithic aerogels. Further works should focus on the large area 3D printing of MAGs and their applications to energy storage. Additionally, improvement of MAG toughness should also be done, through polymer compositing to provide carbon connections between MAG particles, and optimized heat treatments.

## **2.16 Acknowledgements**

This chapter has been published in revised form in Ryan M Hensleigh, Huachen Cui, James S Oakdale, C Ye Jianchao, Patrick G Campbell, Eric B Duoss, Christopher M Spadaccini, Xiaoyu Zheng, Marcus A Worsley, Additive manufacturing of complex micro-architected graphene aerogels, *Materials Horizons*, 2018, Volume 5, Issue 6, pp. 1035-1041, DOI: <https://doi.org/10.1039/C8MH00668G>, with permission from the Royal Society of Chemistry.

No commercial re-distribution or re-use allowed.

## **2.17 Materials and Methods**

Single Layer Graphene oxide (GO) XY dimensions of 1-20 μm was purchased from CheapTubes. Dimethylformamide (DMF), Bisphenol A ethoxylate (2 EO/phenol)

dimethacrylate (BisA-EDMA) with an average molar mass of  $M_n \sim 484$ , polyethylene glycol diacrylate  $M_n \sim 700$  (PEGDA700), ammonium hydroxide (28 - 30% in water), and phenylbis(2,4,6-trimethylbenzoyl)phosphine oxide (Irg819) were purchased from Sigma-Aldrich.

**Preparation of Photocurable Graphene Aerogel Resin:** In a typical preparation, 0.2 g GO was dispersed by ultrasonication in deionized water (20 g). GO crosslinking was catalyzed by 3.6 g of ammonium hydroxide (0.18 g/1 g GO dispersion) while heating at 80 °C for 96 h following previous reports.<sup>[19]</sup> After the reaction, the XGO hydrogel was washed by gently decanting and adding fresh deionized water, at least 3X for 12 h each. The XGO hydrogel was then exchanged with acetone, twice for 12 h, and finally with DMF twice for 12 h. Approximately 20 mL of solvent was used for each exchange, except the final DMF exchange which was set at 20 g for the final concentration (1 wt% or 10 mg/g of GO/DMF). The XGO hydrogel in DMF was broken up with a spatula to 1 to 5 mm diameter pieces, and then ultrasonicated for 24 h. To the XGO dispersion 1.2 g PEGDA700, 1.2 g BisA-EDMA, and 0.8 g Irg819 were added to make the XGO resin.

**Three-Dimensional Printing of Graphene Aerogel:** To print structures, we used a custom built system equipped with a 405 nm light source. A three-dimensional CAD model is sliced vertically into a series of layers. Using a spatial light modulator (SLM) as a dynamically reconfigurable digital photomask, each two-dimensional image slice is sequentially transmitted to the SLM which takes on the pattern of the image. Near-UV

light illuminates the SLM from a photodiode, and a patterned beam is reflected. The patterned beam is reflected by a galvanometer mirror pair onto the photoresin. Where the two-dimensional image hits the resin, the material crosslinks and solidifies. Subsequently, the substrate on which the layer rests is lowered, thus reflowing a thin film of liquid over the cured layer. The image projection is then repeated, with the next image slice forming the subsequent layer. Parts of differing relative densities were made by varying the light exposure time of the parts, effectively producing parts with varying strut thicknesses.

**Bulk Sample Preparation:** Bulk samples for porosimetry were prepared by sandwiching the photocurable resin between glass slides with a small, ~0.5 mm spacer and curing in a broad spectrum light box (ELC-500) for 4 min on each side.

**Drying and Carbonization:** After printing, the resulting green gels were washed in DMF with sonication for a few min. They were then soaked in acetone for 24 h to remove all the DMF, exchanging the acetone several times. The wet gels were subsequently dried with supercritical CO<sub>2</sub> (Electron Microscope Sciences, EMS3100) for 24 h. For freeze-drying, green gels were washed in DMF with sonication for a few min. They were then rinsed with ethanol several times (a few mL for ~1 min) to remove DMF, and then soaked in water for 24 h, before freezing at -20°C. These frozen samples were lyophilized on a VWR lyophilizer for 24 h.

Samples were pyrolyzed at 1050°C under a N<sub>2</sub> atmosphere for 3 h, ramping up and down from room temperature at 1°C per minute. The graphene aerogel materials were isolated as black 3D carbon structures.

Characterization: Surface area was analyzed by Brunauer-Emmett-Teller nitrogen porosimetry using ASAP 2000 Surface Area Analyzer (Micrometrics Instrument Corporation). Samples from 0.05 to 0.1 grams were put under vacuum ( $10^{-5}$  Torr) and heated at 150 °C for 24 h to remove adsorbed species before testing. Micro-Raman was done using a Renishaw inVia spectrometer with a 50x Leica objective and a 514 nm 9 mW Ar<sup>+</sup> laser.

Mechanical Testing: Samples were tested in an Instron 5944 using standard flat compression plates (T1223-1022) and 500N load cell. Each sample was run through 5 cycles, at 2% strain each cycle, with a strain rate of 0.01% strain/min. Samples were tested on the [010] face, i.e. perpendicular to the build direction, to avoid support material which could lower the modulus. Data was extracted over less than 10% of the total loading or unloading curve, typically from the second or third cycle, to assure the Instron plate was fully attached to the sample. If the Z direction of a Cartesian coordinate system is the build direction, then the average X and Z of the lattice were determined by optical microscopy and used as the cross-sectional area, while the Y of the lattice was used as the length of the sample to calculate percent strain.

Conductivity: Conductivity was measured by first coating a XGO MAG by sputtering palladium on two opposite faces of the lattice. The resistance from these faces were measured by a multimeter, and converting to conductivity using the measured distance between contact points by optical microscopy. This is a simplified approximation, as the pathways in the lattices tested are actually longer than the direct distance measured.

## 2.18 References

1. A. Peigney, C. Laurent, E. Flahaut, R. R. Bacsa and A. Rousset, *Carbon*, 2001, 39, 507–514.
2. M. A. Worsley, P. J. Pauzauskie, T. Y. Olson, J. Biener, J. H. Satcher and T. F. Baumann, *J. Am. Chem. Soc.*, 2010, 132, 14067–14069.
3. C. Lee, X. Wei, J. W. Kysar and J. Hone, *Science*, 2008, 321, 385–388.
4. B. F. Machado and P. Serp, *Catal. Sci. Technol.*, 2011, 2, 54–75.
5. C. Zhu, T. Liu, F. Qian, T. Y.-J. Han, E. B. Duoss, J. D. Kuntz, C. M. Spadaccini, M. A. Worsley and Y. Li, *Nano Lett.*, 2016, 16, 3448–3456.
6. X. Zheng, W. Smith, J. Jackson, B. Moran, H. Cui, D. Chen, J. Ye, N. Fang, N. Rodriguez, T. Weisgraber and C. M. Spadaccini, *Nat. Mater.*, 2016, 15, 1100.
7. C. Zhu, T. Y.-J. Han, E. B. Duoss, A. M. Golobic, J. D. Kuntz, C. M. Spadaccini and M. A. Worsley, *Nat. Commun.*, 2015, 6, ncomms7962.
8. X. Zheng, H. Lee, T. H. Weisgraber, M. Shusteff, J. DeOtte, E. B. Duoss, J. D. Kuntz, M. Biener, Q. Ge, J. A. Jackson, S. O. Kucheyev, N. X. Fang and C. M. Spadaccini, *Science*, 2014, 344, 1373–1377.
9. A. Nieto, B. Boesl and A. Agarwal, *Carbon*, 2015, 85, 299–308.
10. Z. Qin, G. S. Jung, M. J. Kang and M. J. Buehler, *Sci. Adv.*, 2017, 3, e1601536.
11. S. Barg, F. M. Perez, N. Ni, P. do V. Pereira, R. C. Maher, E. Garcia-Tuñon, S. Eslava, S. Agnoli, C. Mattevi and E. Saiz, *Nat. Commun.*, 2014, 5, 4328.

12. E. García-Tuñon, S. Barg, J. Franco, R. Bell, S. Eslava, E. D'Elia, R. C. Maher, F. Guitian and E. Saiz, *Adv. Mater.*, 2015, 27, 1688–1693.
13. Y. Jiang, Z. Xu, T. Huang, Y. Liu, F. Guo, J. Xi, W. Gao and C. Gao, *Adv. Funct. Mater.*, 2018, 28, 170724.
14. Y. Lin, F. Liu, G. Casano, R. Bhavsar, I. A. Kinloch and B. Derby, *Adv. Mater.*, 2016, 28, 7993–8000.
15. Q. Zhang, F. Zhang, S. P. Medarametla, H. Li, C. Zhou and D. Lin, *Small*, 2016, 12, 1702–1708.
16. J. Sha, Y. Li, R. Villegas Salvatierra, T. Wang, P. Dong, Y. Ji, S.-K. Lee, C. Zhang, J. Zhang, R. H. Smith, P. M. Ajayan, J. Lou, N. Zhao and J. M. Tour, *ACS Nano*, 2017, 11, 6860–6867.
17. Q. Zhang, F. Zhang, X. Xu, C. Zhou and D. Lin, *ACS Nano*, 2018, 12, 1096-1106.  
DOI:10.1021/acsnano.7b06095.
18. X. Zheng, J. Deotte, M. P. Alonso, G. R. Farquar, T. H. Weisgraber, S. Gemberling, H. Lee, N. Fang and C. M. Spadaccini, *Rev. Sci. Instrum.*, 2012, 83, 125001.
19. M. A. Worsley, S. O. Kucheyev, H. E. Mason, M. D. Merrill, B. P. Mayer, J. Lewicki, C. A. Valdez, M. E. Suss, M. Stadermann, P. J. Pauzauskie, J. H. Satcher, J. Biener and T. F. Baumann, *Chem. Commun.*, 2012, 48, 8428–8430.
20. M. A. Worsley, T. Y. Olson, J. R. I. Lee, T. M. Willey, M. H. Nielsen, S. K. Roberts, P. J. Pauzauskie, J. Biener, J. H. Satcher and T. F. Baumann, *J. Phys. Chem. Lett.*, 2011, 2, 921–925.

21. J. I. Paredes, S. Villar-Rodil, A. Martínez-Alonso and J. M. D. Tascón, *Langmuir*, 2008, 24, 10560–10564.
22. H. Korhonen, L. H. Sinh, N. D. Luong, P. Lehtinen, T. Verho, J. Partanen and J. Seppälä, *Phys. Status Solidi A*, 2016, 213, 982–985.
23. D. Graf, F. Molitor, K. Ensslin, C. Stampfer, A. Jungen, C. Hierold and L. Wirtz, *Nano Lett.*, 2007, 7, 238–242.
24. A. C. Ferrari and J. Robertson, *Phys. Rev. B*, 2000, 61, 14095–14107.
25. A. C. Ferrari, *Solid State Commun.*, 2007, 143, 47–57.
26. F. Tuinstra and J. L. Koenig, *J. Chem. Phys.*, 1970, 53, 1126–1130.
27. X. Xie, Y. Zhou, H. Bi, K. Yin, S. Wan and L. Sun, *Sci. Rep.*, , DOI:10.1038/srep02117.
28. M. A. Worsley, S. Charnvanichborikarn, E. Montalvo, S. J. Shin, E. D. Tylski, J. P. Lewicki, A. J. Nelson, J. H. Satcher, J. Biener, T. F. Baumann and S. O. Kucheyev, *Adv. Funct. Mater.*, 2014, 24, 4259–4264.
29. M. A. Worsley, T. T. Pham, A. Yan, S. J. Shin, J. R. I. Lee, M. Bagge-Hansen, W. Mickelson and A. Zettl, *ACS Nano*, 2014, 8, 11013-11022.
30. J. C. M. F.R.S, *Lond. Edinb. Dublin Philos. Mag. J. Sci.*, 1864, 27, 294–299.
31. L. R. Meza, S. Das and J. R. Greer, *Science*, 2014, 345, 1322–1326.
32. S. Barg, F. M. Perez, N. Ni, P. do Vale Pereira, R. C. Maher, E. Garcia-Tuñon, S. Eslava, S. Agnoli, C. Mattevi and E. Saiz, *Nat. Commun.*, 2014, 5, 4328.
33. Z. Han, Z. Tang, P. Li, G. Yang, Q. Zheng and J. Yang, *Nanoscale*, 2013, 5, 5462–5467.
34. Y. Li, J. Chen, L. Huang, C. Li, J.-D. Hong and G. Shi, *Adv. Mater.*, 2014, 26, 4789–4793.

35. L. Lv, P. Zhang, H. Cheng, Y. Zhao, Z. Zhang, G. Shi and L. Qu, *Small*, 2016, 12, 3229–3234.
36. H. Sun, Z. Xu and C. Gao, *Adv. Mater.*, 2013, 25, 2554–2560.
37. Z. Tang, S. Shen, J. Zhuang and X. Wang, *Angew. Chem. Int. Ed.*, 2010, 49, 4603–4607.
38. Q. Zhang, X. Xu, D. Lin, W. Chen, G. Xiong, Y. Yu, T. S. Fisher and H. Li, *Adv. Mater.*, 2016, 28, 2229–2237.
39. X. Zhang, Z. Sui, B. Xu, S. Yue, Y. Luo, W. Zhan and B. Liu, *J. Mater. Chem.*, 2011, 21, 6494–6497.
40. M. A. Worsley, S. O. Kucheyev, J. H. Satcher, A. V. Hamza and T. F. Baumann, *Appl. Phys. Lett.*, 2009, 94, 073115.
41. R. W. Pekala, C. T. Alviso and J. D. LeMay, *J. Non-Cryst. Solids*, 1990, 125, 67–75.
42. S. N. Khaderi, V. S. Deshpande and N. A. Fleck, *Int. J. Solids Struct.*, 2014, 51, 3866–3877.
43. R. Lakes, *Nature*, 1993, 361, 511–515.
44. R. Raccichini, A. Varzi, S. Passerini and B. Scrosati, *Nature Materials*, 2015, 14, 271–279.
45. P. V. Braun and J. B. Cook, *ACS Nano*, 2018, 12, 3060–3064.
46. K. Zhao, T. Zhang, H. Chang, Y. Yang, P. Xiao, H. Zhang, C. Li, C. S. Tiwary, P. M. Ajayan and Y. Chen, *Science Advances*, 2019, 5.
47. H. Sun, Z. Xu and C. Gao, *Advanced Materials*, 2013, 25, 2554–2560.
48. L. Qiu, J. Z. Liu, S. L. Y. Chang, Y. Wu and D. Li, *Nature Communications*, 2012, 3, 1241.

49. J. Liu, Y. Liu, H.-B. Zhang, Y. Dai, Z. Liu and Z.-Z. Yu, *Carbon*, 2018, 132, 95–103.
50. Q. Zhang, X. Xu, D. Lin, W. Chen, G. Xiong, Y. Yu, T. S. Fisher and H. Li, *Advanced Materials*, 2016, 28, 2229–2237.
51. H.-L. Gao, Y.-B. Zhu, L.-B. Mao, F.-C. Wang, X.-S. Luo, Y.-Y. Liu, Y. Lu, Z. Pan, J. Ge, W. Shen, Y.-R. Zheng, L. Xu, L.-J. Wang, W.-H. Xu, H.-A. Wu and S.-H. Yu, *Nature Communications*, 2016, 7, 12920.
52. M. Yang, N. Zhao, Y. Cui, W. Gao, Q. Zhao, C. Gao, H. Bai and T. Xie, *ACS Nano*, 2017, 11, 6817–6824.
53. M. Peng, Z. Wen, L. Xie, J. Cheng, Z. Jia, D. Shi, H. Zeng, B. Zhao, Z. Liang, T. Li and L. Jiang, *Advanced Materials*, 2019, 31, 1902930.
54. K. H. Kim, Y. Oh and M. F. Islam, *Nature Nanotech*, 2012, 7, 562–566.
55. J. Herzberger, V. Meenakshisundaram, C. B. Williams and T. E. Long, *ACS Macro Lett.*, 2018, 7, 493–497.
56. A. Kudo, P. G. Campbell and J. Biener, *ChemNanoMat*, 2018, 4, 338–342.
57. A. Ganguly, S. Sharma, P. Papakonstantinou and J. Hamilton, *J. Phys. Chem. C*, 2011, 115, 17009–17019.
58. R. M. Hensleigh, H. Cui, J. S. Oakdale, J. C. Ye, P. G. Campbell, E. B. Duoss, C. M. Spadaccini, X. Zheng and M. A. Worsley, *Materials Horizons*, 2018, 5, 1035–1041.

## CHAPTER 3: FUNCTIONALIZED PIEZOELECTRIC PARTICLES FOR ENHANCED COMPOSITE RESPONSE

### 3.1 Introduction

Composites are by far the most common method to allow P $\mu$ SL printing. Due to the light polymerization requirement, there are few options for feedstock materials. By far the most prominent materials that meet this requirement, as well as the cure speed (<1 min) and viscosity (typically <10 Pa\*s) requirements, are acrylates, vinyls, and thiol-ene organic monomer systems. This severely limits P $\mu$ SL's ability to form functional materials as most functional materials are inorganic. The only method by which to print these highly response functional inorganics, is through compositing with the aforementioned acrylics, vinyls, or thiol-ene monomers. However, P $\mu$ SL typically also has strict viscosity requirements, which limits the maximum processable inorganic loading. Other techniques, particular direct ink write extrusion, have far more development in functional materials, as they can process very high loadings (>50wt%) of inorganic materials with very high viscosity, but are limited to log-pile like structures (inks are not self-supporting) and typically low resolution (>100  $\mu$ m).

To overcome this, a concerted effort is needed to improve P $\mu$ SL ink performance and processability to allow high-resolution (<100  $\mu$ m), and true freeform 3D structures with highly functional composites. Several problems require attention. Higher loadings of inorganics are needed, which maintain lower viscosity. If loading cannot be increased, then the response of the composite, with fixed loadings, needs to be enhanced. I have chosen to focus particularly on the problem of enhancing response at a fixed loading.

### 3.2 P $\mu$ SL of Piezoelectrics

Interconversion of mechanical energy to electrical energy through the piezoelectric effect has been long known and today finds wide application from actuators to microphones. The effect arises from a crystal asymmetry, and this crystalline requirement is directly reflected in the strong piezoelectric response of inorganics, such as barium titanate (BTO) and lead zirconate-titanate (PZT). These classic piezoelectric ceramics exhibit strong piezoelectric coefficients ( $d_{33}$ ) of 300 and 200 pC/N respectively, but their high brittleness and near impossible machinability into complex shapes, limits their utility, particularly for in-vivo and wearable technologies.<sup>4</sup>

Semi-crystalline polymer piezoelectrics have been demonstrated, with the most notable example being poly(vinylidene fluoride) (PVDF). These polymer piezoelectrics possess the desirable flexibility of rubbers, and have regularly been used to demonstrate flexible piezoelectric systems capable of being stretched or manipulated for various technologies such as wearables. However, the low piezoelectric coefficient of PVDF ( $\sim 20$  pC/N), and processing difficulty in controlling polymer crystallinity, has limited polymer piezoelectrics.<sup>5</sup>

Many reports seek to combine the high piezoelectric coefficient of inorganic piezoelectrics with the flexibility and processability of polymers. Two primary methods have been explored. The first, and much more developed, relies on elaborate microfabrication processes, patterning a thin film piezoelectric and conductor array and then encapsulating in a polymer.<sup>6-10</sup> The performance is impressive, but the complex processing limits scalability and

limits structures to relatively simple 2-dimensional (2D) planar, stacked systems, or relatively simple kirigami or origami-like structures.<sup>11</sup>

The other method, relies on nanocomposites of inorganic piezoelectric nanomaterials dispersed in a polymer matrix. Nanocomposites give greater processability, scalability, and have demonstrated complex 2D structures which could self-fold into pseudo-3D structures.<sup>5,12</sup> Their main drawback is the degradation of the piezoelectric coefficient by 1 to 2 orders-of-magnitude compared to the pure piezoelectric.<sup>13,14</sup> Enhancing the performance of piezoelectric nanocomposites (PNCs) would offer a scalable platform for materials with high piezoelectric performance, high flexibility, and the ability for processing into complex devices.

Recently, surface functionalization of piezoelectric nanoparticles with a monolayer of was used to enhance PNC performance by about an order of magnitude to near 50% that of the pure ceramic. These functionalization agents presumably forms a monolayer, which is able to crosslink with the polymer matrix. These functionalized PNCs (PNC-f) showed a strong dependence of piezoelectric performance on matrix stiffness, and of functionalization agent binding to the surface, indicating that more efficient load transfer between the polymer matrix intermediary and the piezoelectric nanoparticle is the likely mechanism of enhancement.

In order to further enhance the performance of PNC, and demonstrate its processability, we explore the use of surface grafted functionalization agents on piezoelectric nanoparticles. These PNC-f enhancing the load transfer from the matrix to the piezoelectric to increase the response of the composite. The processability of PNC-f is demonstrated by printing complex, 3D PNC architectures via light-based additive manufacturing. We demonstrate a high-performance flexible piezoelectric composite with only a single-material.

In **Figure 3-1**, is a schematic showing the overall process and theory. That surface functionalization will lead to enhanced piezoelectric composite response.

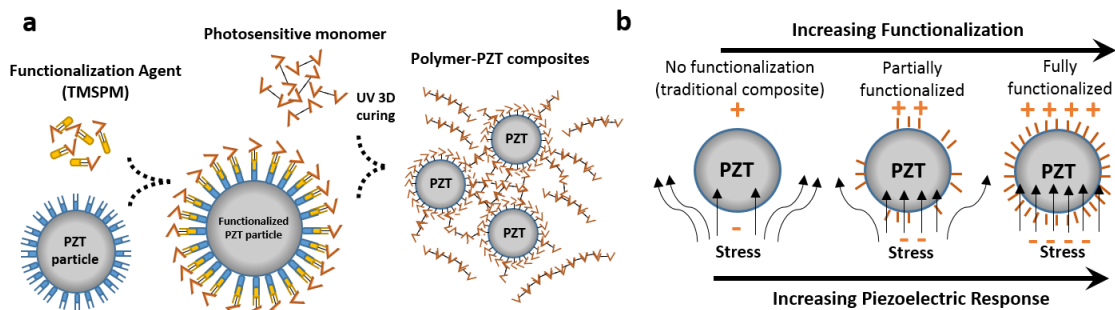


**Figure 3-1: Surface Functionalization Piezoelectric Nanoparticles** – (a) Schematic for PZT functionalization and 3D printing. (b) Hypothesis of PZT functionalization, with highest functionalization giving highest response.

Using commercially available PZT, and methacrylate-alkoxysilane (TMSPM) we developed a protocol for acrylate surface functionalization of PZT. Alkoxysilanes are well known to react with a wide variety of surface. By refluxing PZT with TMSPM in deionized water we were able to attach TMSPM to the surface. Only in water was significant TMSPM attachment found, ethanol and other solvents did not produce significant functionalization, as measured by Fourier-transform Infrared Spectroscopy (FTIR). This is a highly aggressive treatment, compared to previous treatments of BTO particles.<sup>13,14</sup> This is likely due to differences between the BTO and PZT surface.

**Figure 3-2** shows the FTIR of thoroughly cleaned functionalized PZT particles with different initial loadings of the surface agent (a) or reaction times (b). The spectrum focuses on the carbonyl and alkene of the acrylate surface groups nominally at  $1710\text{ cm}^{-1}$  and  $1630\text{ cm}^{-1}$ , respectively. It

shows the functionalization level can be varied by the surface linker loading or reaction time. We functionalized PZT particles with 0wt% ~ 150wt% surface linker loadings. Above the “100%” threshold, we do not see a nominal increase in the FTIR peak, indicating maximum surface coverage.

We loaded particles with different functionalization levels with the UV curable resin having 3% and 30% volume loadings (equivalent to 18.8wt%~76.3wt% loading), and were used for fabricating cuboid samples (8mm by 8mm by 2 mm). As-fabricated samples were tested, and the  $d_{33}$  constants of the samples are summarized in Figure 3-2c. For the low particle loading (3vol%) composite, the  $d$  constant is nearly zero without functionalization, and increases with the functionalization level until the particles are fully functionalized. The same trend was observed for the high particle loading (30vol%, i. e., 76.3wt%) composite, i.e., the  $d$  constant increases from ~50pC/N to ~100pC/N with fully functionalized nanoparticles.

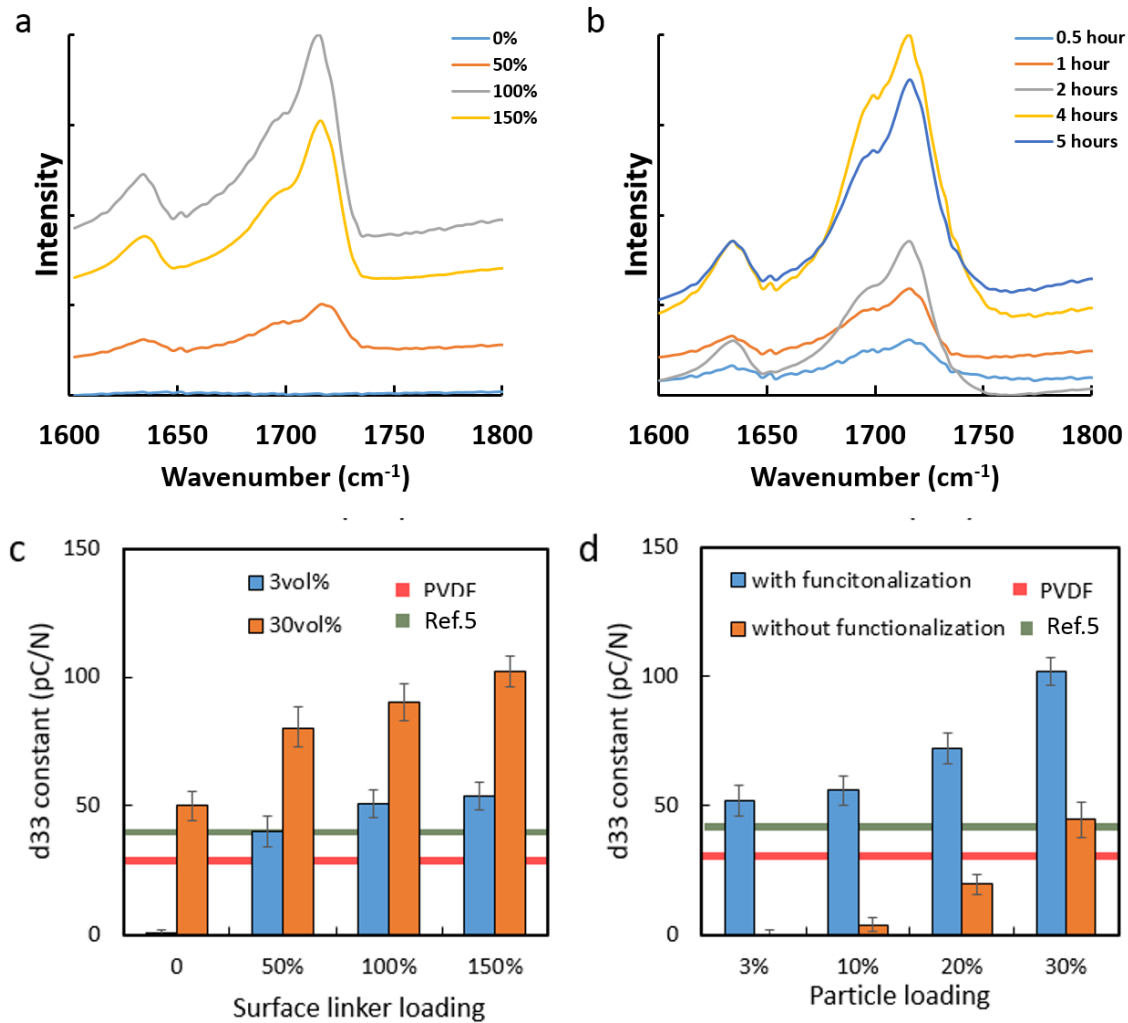


**Figure 3-2: FTIR and  $d_{33}$  of Functionalized Piezoelectrics** a) Fourier-transform infrared spectroscopy (FTIR) result showing the effects of different TMSPM loading. b) FTIR result showing the effects of reaction time on the surface functionalization, peaks around 4hrs. c)  $d$  constant as a function of the surface linker loading of the functionalization of PZT nanoparticles. d) Comparison of  $d$  constant as a function of nanoparticle volume loading percentage under two conditions: with functionalization and without functionalization.

This work successfully functionalized the surface of PZT particles with silane acrylate monomers and optimized the reaction process. Importantly, we see a clear enhancement with surface functionalization, indicating this is a viable means to enhance composite performance for P $\mu$ SL manufacturing of piezoelectrics. This work was applied to create high performance piezoelectric architectures with directional response. These composites have the highest response of any previously reported 3D printed piezoelectric composite.<sup>15</sup>

### 3.3 Piezoelectric Fibers

Recent work in collaboration with my colleague Desheng Yao,<sup>15</sup> has corroborated the piezoelectric composite enhancement through numerical modelling. His work additionally revealed that particle aspect ratio has a significant effect on composite performance, **Figure 3-3**. He found an increasing aspect ratio i.e. the particles becoming more wire-like, resulted in a seven times increase in composite performance. Additionally, work by Xu et al. found that lead magnesium niobate-lead titanate (PMN-PT) piezoelectric nanowires and hierarchical nanowires, exhibited nearly order-of-magnitude improvements in composite performance vs particle composites.<sup>16,17</sup> PMN-PT is one the highest performing piezoelectrics known. Therefore, we focused on replicating and applying this work.

Xu et al.'s synthesis is based on a sol-gel hydrothermal growth of PMN-PT wires, however, initial attempt to directly replicate the work met with failure, no material was precipitated i.e. no powder was produced. The critical component was identified as sodium hydroxide, which is added to sol-gel to induce precipitation. The amounts recommended in the manuscript appeared

to be too small, and were increased, and subsequently, hierarchical-wires of PMN-PT, which were previously reported to have the highest piezoelectric response known were produced.<sup>16</sup>

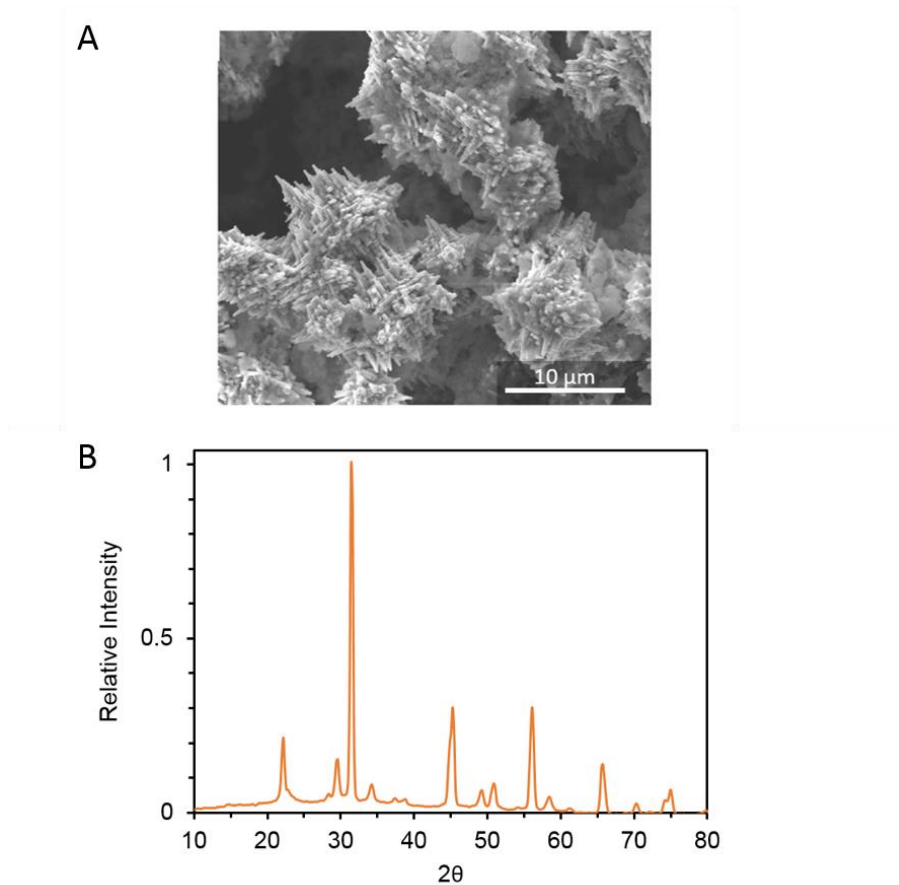


**Figure 3-3: Piezoelectric Wire Composites** a) As synthesized PMN-PT hierarchical wires  
c) XRD of PMN-PT wires showing the desired perovskite crystal structure

The XRD, Figure 3-3C matches well with the expected structure. The current limitation and focus is on scaling up the production of the wires to usable amounts. While successful, the overall yield of the Xu et al. hydrothermal method (~0.1g/batch) was far too low to be practically applied for making PuSL resin. At minimum to develop a PuSL resin, approximately 20mL of

material is needed, which at a 50vol% loading of PMN-PT (8.1 g/mL), would require 81g, or >800 replications of the Xu et al. synthesis (36h total reaction time, ~3.3 years to replicate).

It was explored if the per batch yield could be increased. In the Xu et al. synthesis, 10g of a PMN-PT sol-gel is dispersed in 50g water. This dilutes the precursors and minimizes the final output of the reaction. A doubling of the amount of sol-gel to 20g, and using 40g water under the same conditions produced only amorphous powder. A subsequent increase in NaOH from 20g to 30g produced hierarchical wires. The ~0.2g/batch was still far too low.

Using pure sol-gel in the reaction was tested, with 30g NaOH. After reacting 24h at 200 °C per the Xu et al. method, no powder precipitated. The NaOH was increased and the process repeated, in 10g NaOH batches until 60g of NaOH was added, at which point the reaction mixture became too viscous to mix. No powder precipitated and this method does not seem viable. Alternative synthesis routes to reach the scales of production are necessary.

### **3.4 Molten Salt Wire Synthesis**

Molten salt is a scalable method that has been commonly used for the synthesis of various metal oxide, and other material nanomaterial structures.<sup>18</sup> Other methods of nanomaterial synthesis, such as hydrothermal and sol-gel methods do not typically produce gram-scale amounts of material per batch, can have complex/time consuming processing, and are not easily repeatable/scalable.<sup>19,20</sup> Molten salt is the most common method to produce gram-scale amounts of piezoelectric fibers.<sup>21,22</sup>

The molten salt method relies on topochemical chemistry, a set of methods for the rational synthesis of inorganics.<sup>21,23</sup> Topochemical methods rely on a parent skeleton maintaining its

structure throughout the reaction process. This parent structure can be modified by exchanging intercalated ions, modifying edge sites, or changing from layered to 3D interconnected. Consider the piezoelectric barium titanate ( $\text{BaTiO}_3$ ), whose structure consists of polyhedral of titanium and oxygen ( $\text{TiO}_3$ ) with the Ba ion intercalated within the polyhedral titanium-oxygen network.<sup>23</sup> The Ba ion can diffuse or be exchanged to form other oxides, such as strontium titanate ( $\text{SrTiO}_3$ ). Importantly, the  $\text{TiO}_3$  network maintains its morphology throughout the reaction, hence beginning with a wire-like  $\text{TiO}_2$  precursor, one can then form many perovskites with the same morphology. Through molten salt topochemical synthesis, precursors with controlled morphology are well known and scalably synthesized.<sup>21,22</sup> There examples of both forming the precursor structure in-situ with the cation, or separately reacting the precursor (such as  $\text{TiO}_2$ ) to form the desired morphology and then treating with the cation in a second reaction to form the final product.

The ultimate goal is to produce PMN-PT wires, however, there are no reports of forming PMN-PT wires via molten salt methods in the literature. There are reports of PMN-PT particle synthesis via molten salt methods, and complex oxides have been made using the molten salt method, so there is no reason to think PMN-PT molten salt synthesis of wires is impossible.<sup>24-26</sup>

Titania<sup>22</sup> and niobate<sup>27,28</sup> wires are both well known in the literature via molten salt, and there are a few reports of combined titano-niobate wires (but not ferroelectric).<sup>29</sup> In those previous explorations, alkali metal niobates and titanate, such as sodium (Na) or potassium (K), were the focus. The alkali ions serve to expand the titanium or niobium lattice, before being topochemically exchanged with the final cation to form the ferroelectric (typically lead, Pb). It has been noted previously that unexpanded parent oxides ( $\text{TiO}_2$  or  $\text{Nb}_2\text{O}_5$ ) when reacted undergo

a change in volume on the order of 40-50%.<sup>30</sup> This induces significant stress, leading to a breakdown in powders to smaller particles than their precursors. Such breakdowns would result in the loss of any initial wire structure, so I solely focused on alkali titanio-niobates precursors. Additionally, previous ferroelectric oxide wire synthesis, have noted, that alkali titanate and alkali niobate wire precursors are layered in structure. These layered structure are well known to undergo ion exchange and delamination which would result in a loss of wire structure.<sup>31</sup> Previous studies found it was critical to remove the alkali component, converting the oxide to a 3D skeletal network, to maintain wire structure.<sup>20,28</sup> This is accomplished by ion exchange of the alkali metal with a proton ( $H^+$ ), and then gentle (400 °C) dehydration.<sup>31-33</sup> This dehydration forces interlayer bonding to occur and the 3D lattice reforms. Critically, these reformed oxides have expanded lattice channels, such as reformed titania having a  $TiO_2$  (B) crystal structure, or reformed  $Ti_2Nb_2O_9$  (from  $KTiNbO_5$ ). These oxides maintain an expanded nature, which can be used to reintercalate cations for batteries, and as previously discussed, will reduce stress during transformation to the ferroelectric oxide ( $PbTiO_3$  and PMN-PT) and help maintain the parent wire structure we are seeking.<sup>34,35</sup>

I chose to first replicate the work of Teshima et al. for the synthesis of potassium titanoniobate rods ( $KTiNbO_5$ ).<sup>29</sup>  $KTiNbO_5$  is similar to (PMN-PT) and I believe it can serve as an excellent starting material for PMN-PT wire production. The results of replicating the Teshima et al. method are show in **Figure 3-4**. Stoichiometric amounts of parent oxides  $TiO_2$  and  $Nb_2O_5$ , potassium carbonate, and potassium chloride were hand mixed and fired at 1020 °C for 2 hours using a 20 mol% loading from Teshima et al. X-ray diffraction (XRD) results are identical to that reported by Teshima et al. These  $KTiNbO_5$  were then converted to  $HTiNbO_5$  by

stirring on a 70 °C hot plate in 6M hydrochloric acid (HCl) for 48 hours, with one HCl exchange at 24 hours.<sup>32,33</sup> HTiNbO<sub>5</sub> maintains the wire structure, and XRD results are also shown in Figure 3-4 in agreement with Teshima, . HTiNbO<sub>5</sub> was then dehydrated at 400 °C for 1h and were converted to Ti<sub>2</sub>Nb<sub>2</sub>O<sub>9</sub>.

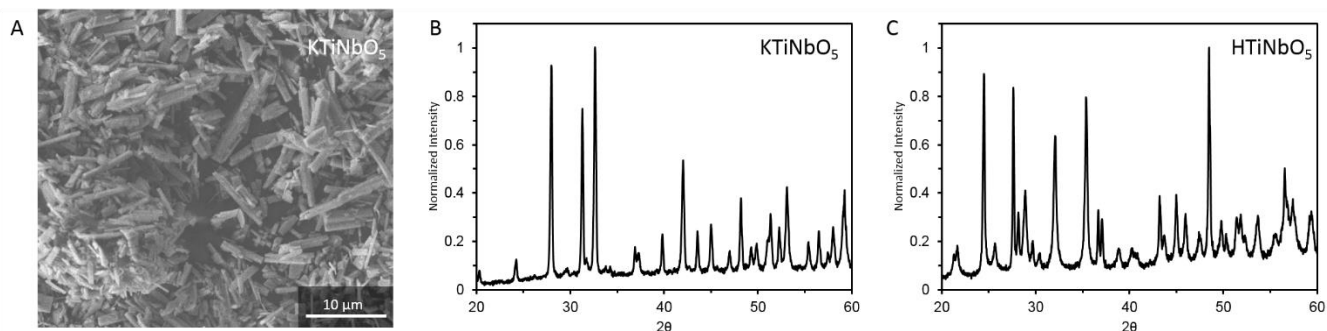


**Figure 3-4: KTiNbO5 Rods** a) SEM of KTiNbO<sub>5</sub> rods b) XRD of KTiNbO<sub>5</sub> rods c) XRD of HTiNbO<sub>5</sub> rods

HTiNbO<sub>5</sub> was then dehydrated at 400 °C for 1h and were converted to Ti<sub>2</sub>Nb<sub>2</sub>O<sub>9</sub> and the appropriate crystal structure is achieved. Critically the wire morphology from the original KTiNbO<sub>5</sub> is maintained through the entire sequence. Ti<sub>2</sub>Nb<sub>2</sub>O<sub>9</sub> was then converted to PbTi<sub>0.5</sub>Nb<sub>0.5</sub>O<sub>3</sub> (PTN) by reacting with lead acetate at 810 °C for 10 min using an equal weight of KCl powder.<sup>26,28</sup> The results are shown in **Figure 3-5**. I have found no reports of reacting Ti<sub>2</sub>Nb<sub>2</sub>O<sub>9</sub> with Pb, and so only nominally refer to the product as PbTiNbO<sub>3</sub> it may posses different stoichiometry. The product has no conductivity (via simple ohm-meter test) and has a strong yellow color. The XRD results (Figure 3-5D) are similar to perovskites. The key question was would the Ti<sub>2</sub>Nb<sub>2</sub>O<sub>9</sub> maintain its wire structure and and Figure 3-5C shows this is the case.

This supports my hypothetical synthesis plan, that such reformed expanded titano-niobates can maintain their wire structure for possible use in perovskite synthesis.

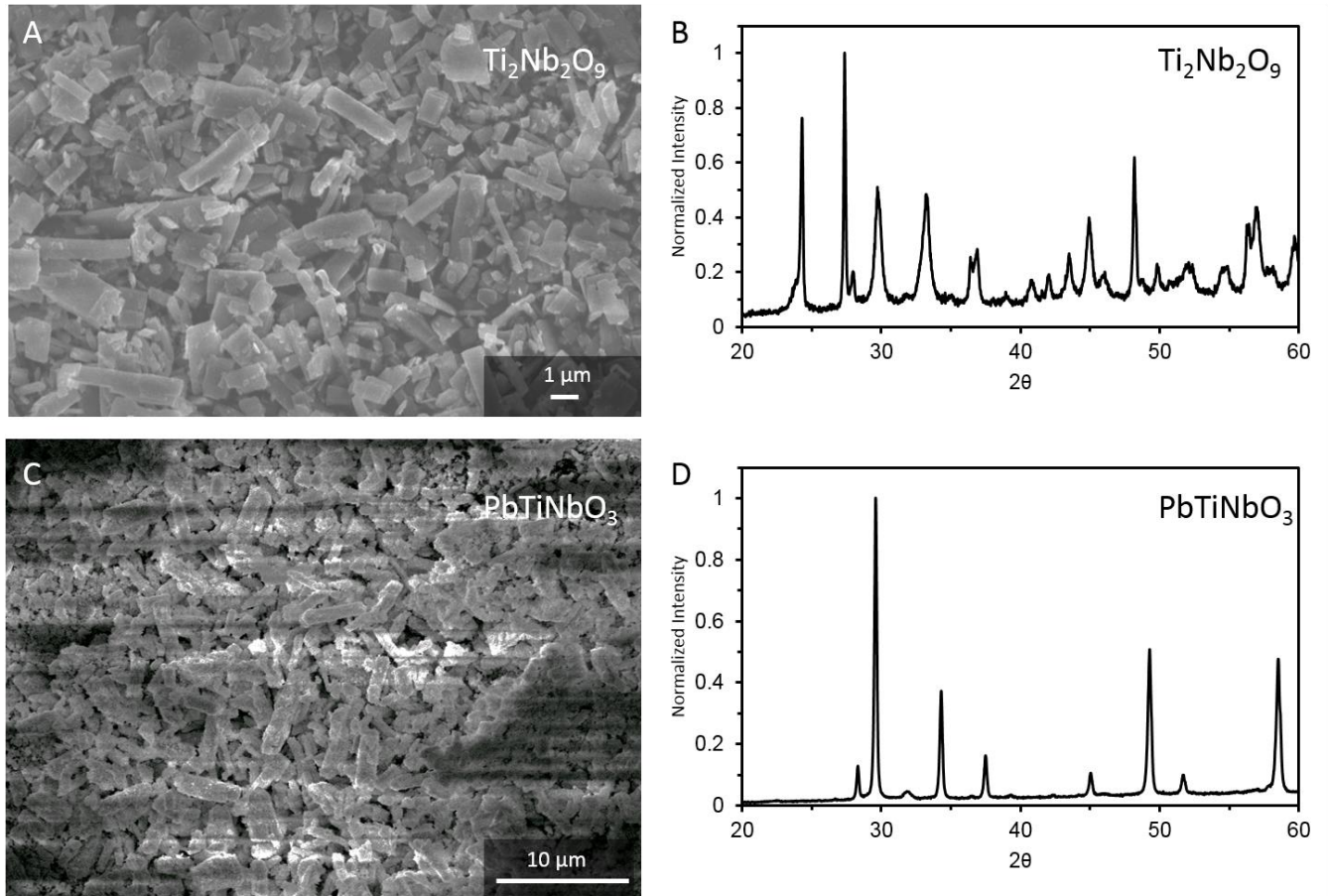


**Figure 3-5: PTN Wires** a-b) SEM and XRD of  $\text{Ti}_2\text{Nb}_2\text{O}_9$  wires c-d) SEM and XRD of  $\text{PbTiNbO}_3$  wires

We then modified this process with the goal of PMN-PT wires. The most desirable being 0.65PMN-0.35PT, due to its extremely high piezoelectric response.<sup>16,17</sup> We therefore maintained the same powder weight as Teshima et al. but modified the Nb/Ti ratio, and replaced 33% of the Nb with MgO to achieve the proper stoichiometry. Reacting at  $1020\ ^\circ\text{C}$  for 3h, with 50 mol% of

KCl, we achieved wire structured, nominally potassium magnesium niobate-potassium titanate (KMN-KT), **Figure 3-6**. It must be noted that I have found no data on any KMN-KT compound being previously reported, even in XRD databases, so it is not clear if this is the true compound, but for simplicity it will be referred to as KMN-KT 65-35. I then performed the same conversion, 48h in 6M HCl, and wire structure is maintained, however, the XRD results are not consistent with an ion exchange, Figure 3-6D. As the H<sup>+</sup> ion is smaller the K<sup>+</sup> an upshift in peaks is expected, and we only see a downshift. This may indicate that the KMN-KT wires are not a layered structure which can undergo ion exchange.

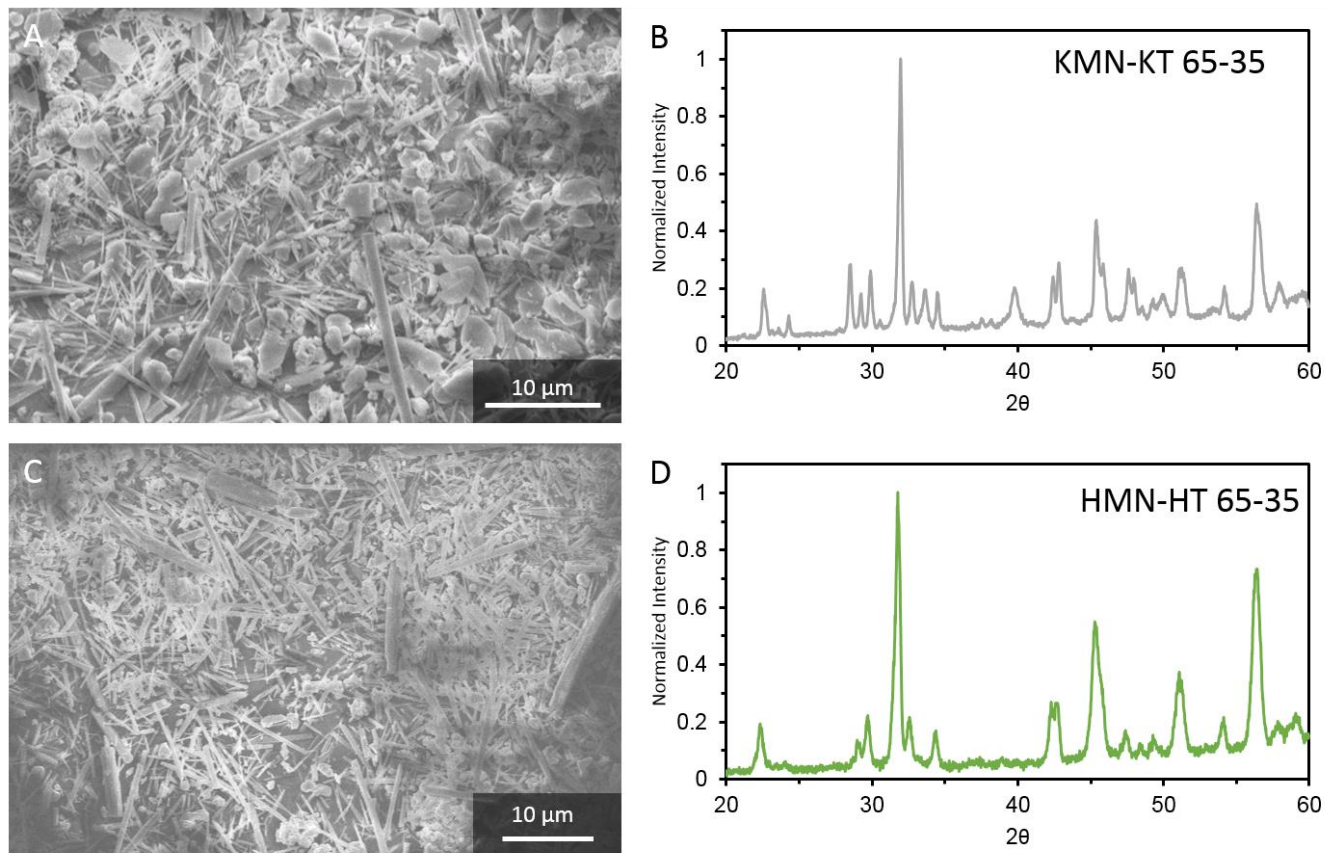


**Figure 3-6: KMN-KT and HMN-HT Wires** a-b) SEM and XRD of KMN-KT 65-35 wires  
c-d) SEM and XRD of HMN-HT wires e-f) SEM and XRD of PMN-PT 65-35 powder

We then similarly performed the dehydration at 400 °C for 1h to form nominally MN-T with expanded lattice, as previously discussed. The wire structure is still maintained, **Figure 3-7**, However, we see no change in MN-T XRD which was expected based on the HTiNbO<sub>5</sub> to Ti<sub>2</sub>Nb<sub>2</sub>O<sub>5</sub> conversion. Li et al.<sup>28</sup> noted much higher temperatures were required, up to 550 C for potassium niobate to niobium oxide dehydration, however, when attempted with MN-T, no changes in XRD were seen (data not shown).

MN-T was then converted to nominally PMN-PT by reacting with lead acetate at 810 °C for 10 min using an equal weight of KCl powder.<sup>26,28</sup> However, the wire structure is lost in this process, Figure 3-7C. This loss of wire structure may be due to as previously discusses, that the KMN-KT and HMN-HT phases are not ion-exchangeable, layered structures. This would explain the confusing shift in XRD from KMN-KT to HMN-HT to MN-T. The XRD of PMN-PT Figure 3-7D is quite similar to PMN-PT, except for a possible PbO contamination at 29 and 30.5 degrees.

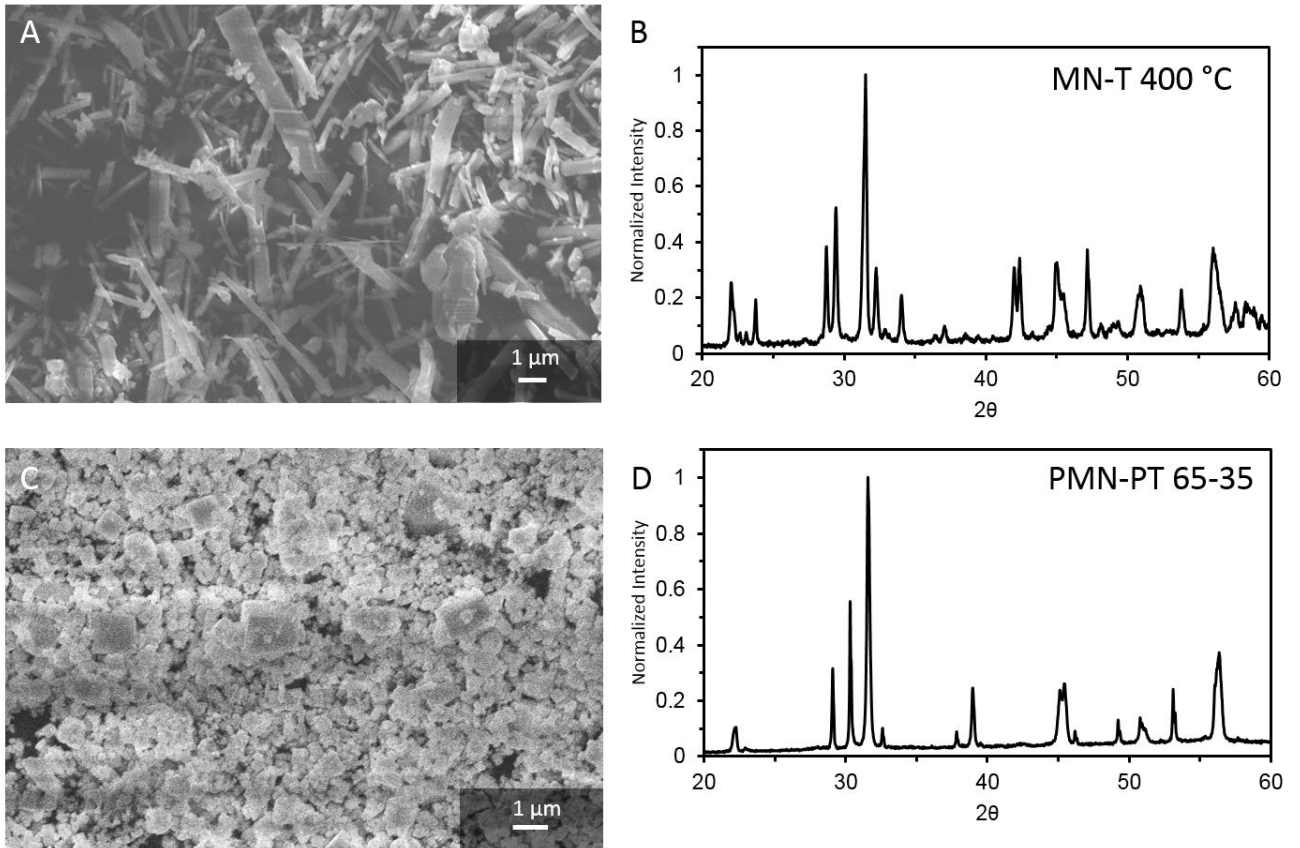


**Figure 3-7: MN-T and PMN-PT** a-b) SEM and XRD of MN-T 65-35 wires c-d) SEM and XRD of PMN-PT powder

Overall, the 65-35 KMN-KT to PMN-PT wire route failed. It should be noted, I have found no previous works which have explored magnesium-titano-niobates, and none of titano-niobates with a 35-65 ratio. However, there are a wide variety of titano-niobates, with high Ti/Nb ratios, which are known to form layered phases with alkali metals. It was hypothesized 65-35 KMN-KT would similarly form a layered phase. Previous studies have noted that Mg replaces Nb in the lattices, and can form expanded phases with potassium in the 66/34 Nb/Mg ratio as was attempted here, though it is not clear how titanium affects this.<sup>36</sup> Titano-niobate studies have noted that the stoichiometry of Nb/Ti can vary and form layered phases, but the ratios of Nb/Ti were quite narrow and focused around the  $\text{KTiNbO}_5$  stoichiometry.<sup>37,38</sup> The highest Nb/Ti ratio found to be stable was 60-40, so it may be the 65/35 Nb/Ti ratio is too divergent, again it is unclear how magnesium incorporation affects this as I have seen no studies explore the potassium-magnesium-niobium-titanium oxide system. The 60-40 Nb/Ti ratio is piezoelectric, though relatively far from the morphotropic phase boundary, but may offer at least an expanded phase which to explore the formation of PMN-PT wires.<sup>40</sup> Additionally, very high Nb/Ti ratio of 90-10 have also been noted with a semi-expanded lattice structure,<sup>41</sup> which would be of interest of 90-10 PMN-PT which is highly electrostrictive.<sup>42</sup>

### **3.5 Summary and Future Work**

The hypothesis that surface functionalization would improve piezoelectric performance, and that maximizing surface functionalization would achieve maximum performance was confirmed. A protocol to surface functionalize PZT particles was demonstrated. The synthesis of

piezoelectric nanowires was attempted and while hydrothermal synthesis results provided the desired wires, the amounts were far lower than practical. A molten salt route was explored but proved unsuccessful, likely due to the 65-35 KMN-KT phase not being an ion-exchangeable phase. Molten salt methods should be further explored for piezoelectric wire synthesis. A 60-40 or 90-10 KMN-KT to PMN-PT route should be explored.

### **3.6 Acknowledgements**

Portions of this dissertation chapter have been published in a revised form in Huachen Cui, Ryan Hensleigh, Desheng Yao, Deepam Maurya, Prashant Kumar, Min Gyu Kang, Shashank Priya, Xiaoyu (Rayne) Zheng, Three-dimensional printing of piezoelectric materials with designed anisotropy and directional response, *Nature Materials*, 2019, Volume 18, pp. 234-241, DOI: <https://doi.org/10.1038/s41563-018-0268-1> *Nature Materials*, see reference 39. No commercial re-distribution or re-use allowed.

Chapter 3 has been published in revised form in Desheng Yao, Huachen Cui, Ryan Hensleigh, Parker Smith, Sam Alford, Dominic Bernero, Sydney Bush, Kyle Mann, H Felix Wu, Marvin Chin-Nieh, Garrett Youmans, Xiaoyu Zheng, Achieving the upper bound of piezoelectric response in tunable, wearable 3D printed nanocomposites, *Advanced Functional Materials*, 2019, Volume 29, Issue 42 DOI: <https://doi.org/10.1002/adfm.201903866>. No commercial re-distribution or re-use allowed.

### 3.7 Materials and Methods

3-(trimethoxysilyl)propyl methacrylate (TMSPM), glacial acetic acid, potassium carbonate, lead acetate trihydrate, niobium oxide, titanium oxide, magnesium oxide, sodium chloride, potassium chloride, and hydrochloric acid (37wt%) were purchased from Millipore-Sigma. Lead-zirconate-titanate was purchased from APC.

0.6g PZT were dispersed in DI water with 1.049g acetic acid via sonication for 10 minutes. Then 1.049g of TMSPM was added and sonicated an additional 5 minutes. This dispersion was boiled for 4-5 hours while stirring with a loose lid. The mixture was washed with ethanol several times and allowed to dry before use.

KTiNbO<sub>5</sub> was grown following Teshima et al.<sup>29</sup> 2.479g potassium carbonate, 2.862g TiO<sub>2</sub> (50/50 anatase/rutile), 4.763g Nb<sub>2</sub>O<sub>5</sub>, and 10.687g KCl were hand ground for 3 minutes using a glass mortar and pestle. They were fired in an alumina crucible with a second crucible laid on top at 1020 °C for 2h, going 4h up to temperature and down. These were washed several times with deionized water, and then once with acetone and then dried.

KMN-KT 65-35 was attempted via a modified Teshima route, combining 2.796g potassium carbonate, 2.2768g TiO<sub>2</sub>, 4.644g Nb<sub>2</sub>O<sub>5</sub>, 0.7042g MgO, and 10.687g KCl, hand grinding for 3 minutes then firing 1020 °C for 2h.

Ion exchange was done by stirring 4g of the powder with ~15mL 6M hydrochloric acid, for 48h, changing the acid once at 24h via centrifugation.

Dehydration was done going 3h up to 400 °C, holding 1h, then coming 3h down to room temperature. Air flow was ~400 mL/min.

Conversion to nominally  $\text{PbNbTiO}_3$  was done by hand grinding 1.5g of  $\text{Ti}_2\text{Nb}_2\text{O}_9$  with 5.3485g lead acetate trihydrate, 3.0329g NaCl, 3.869g KCl for 3 minutes. For PMN-PT 65-35, 1.5g of MN-T, 5.9962g lead acetate trihydrate, 3.3204g NaCl, 4.2357g KCl were hand ground for 3 minutes. These mixtures were fired in an alumina crucible with a second crucible sitting on top, at 810 °C for 10 minutes, going 3h up to and down from temperature in 400 mL/min flowing air.

### 3.8 References

1. Bauer, J. *et al.* Nanolattices: An Emerging Class of Mechanical Metamaterials. *Advanced Materials* **29**, 1701850 (2017).
2. Zheng, X. *et al.* Ultralight, ultrastiff mechanical metamaterials. *Science* **344**, 1373–1377 (2014).
3. Cui, H., Hensleigh, R., Chen, H. & Zheng, X. Additive Manufacturing and size-dependent mechanical properties of three-dimensional microarchitected, high-temperature ceramic metamaterials. *Journal of Materials Research* **33**, 360–371 (2018).
4. Dagdeviren, C. *et al.* Recent progress in flexible and stretchable piezoelectric devices for mechanical energy harvesting, sensing and actuation. *Extreme Mechanics Letters* **9**, 269–281 (2016).
5. Kim, K. *et al.* 3D Optical Printing of Piezoelectric Nanoparticle–Polymer Composite Materials. *ACS Nano* **8**, 9799–9806 (2014).
6. Dagdeviren, C. *et al.* Conformal piezoelectric energy harvesting and storage from motions of the heart, lung, and diaphragm. *PNAS* **111**, 1927–1932 (2014).
7. Park, K.-I. *et al.* Highly-Efficient, Flexible Piezoelectric PZT Thin Film Nanogenerator on Plastic Substrates. *Adv. Mater.* **26**, 2514–2520 (2014).
8. Hwang, G.-T. *et al.* Self-Powered Cardiac Pacemaker Enabled by Flexible Single Crystalline PMN-PT Piezoelectric Energy Harvester. *Adv. Mater.* **26**, 4880–4887 (2014).
9. Park, D. Y. *et al.* Self-Powered Real-Time Arterial Pulse Monitoring Using Ultrathin Epidermal Piezoelectric Sensors. *Adv. Mater.* **29**, n/a-n/a (2017).

10. Lu, B. *et al.* Ultra-flexible Piezoelectric Devices Integrated with Heart to Harvest the Biomechanical Energy. *Scientific Reports* **5**, srep16065 (2015).
11. Yan, Z. *et al.* Mechanical assembly of complex, 3D mesostructures from releasable multilayers of advanced materials. *Sci Adv* **2**, (2016).
12. Kim, K. *et al.* Tunable Surface and Matrix Chemistries in Optically Printed (0–3) Piezoelectric Nanocomposites. *ACS Appl. Mater. Interfaces* **8**, 33394–33398 (2016).
13. Siddiqui, S. *et al.* High-performance flexible lead-free nanocomposite piezoelectric nanogenerator for biomechanical energy harvesting and storage. *Nano Energy* **15**, 177–185 (2015).
14. Park, K.-I. *et al.* Flexible Nanocomposite Generator Made of BaTiO<sub>3</sub> Nanoparticles and Graphitic Carbons. *Adv. Mater.* **24**, 2999–3004 (2012).
15. Yao, D. *et al.* Achieving the Upper Bound of Piezoelectric Response in Tunable, Wearable 3D Printed Nanocomposites. *Advanced Functional Materials* **29**, 1903866 (2019).
16. Xu, S. *et al.* Flexible Piezoelectric PMN–PT Nanowire-Based Nanocomposite and Device. *Nano Letters* **13**, 2393–2398 (2013).
17. Xu, S., Poirier, G. & Yao, N. PMN-PT Nanowires with a Very High Piezoelectric Constant. *Nano Letters* **12**, 2238–2242 (2012).
18. Liu, X., Fechler, N. & Antonietti, M. Salt melt synthesis of ceramics, semiconductors and carbon nanostructures. *Chemical Society Reviews* **42**, 8237–8265 (2013).
19. Cho, S.-B., Oledzka, M. & Riman, R. E. Hydrothermal synthesis of acicular lead zirconate titanate (PZT). *Journal of Crystal Growth* **226**, 313–326 (2001).

20. Zhou, Z., Tang, H. & Sodano, H. A. Scalable Synthesis of Morphotropic Phase Boundary Lead Zirconium Titanate Nanowires for Energy Harvesting. *Advanced Materials* 26, 7547–7554 (2014).
21. Li, L., Deng, J., Chen, J. & Xing, X. Topochemical molten salt synthesis for functional perovskite compounds. *Chemical Science* 7, 855–865 (2016).
22. Mao, Y., Banerjee, S. & Wong, S. S. Large-Scale Synthesis of Single-Crystalline Perovskite Nanostructures. *J. Am. Chem. Soc.* 125, 15718–15719 (2003).
23. Schaak, R. E. & Mallouk, T. E. Perovskites by Design: A Toolbox of Solid-State Reactions. *Chem. Mater.* 14, 1455–1471 (2002).
24. Zhao, S., Li, Q., Feng, Y. & Nan, C. Microstructure and dielectric properties of PMN–PT ceramics prepared by the molten salts method. *Journal of Physics and Chemistry of Solids* 70, 639–644 (2009).
25. Yoon, K. H., Cho, Y. S. & Kang, D. H. Molten salt synthesis of lead-based relaxors. *Journal of Materials Science* 33, 2977–2984 (1998).
26. Zupei, Y., Shaorong, Z., Shaobo, Q., Bin, C. & Changsheng, T. Reaction mechanisms of PMN-PT powder prepared by molten salt synthesis. *Ferroelectrics* 265, 225–232 (2002).
27. Xu, C.-Y., Zhen, L., Yang, R. & Wang, Z. L. Synthesis of Single-Crystalline Niobate Nanorods via Ion-Exchange Based on Molten-Salt Reaction. *J. Am. Chem. Soc.* 129, 15444–15445 (2007).
28. Li, L. et al. Wire Structure and Morphology Transformation of Niobium Oxide and Niobates by Molten Salt Synthesis. *Chem. Mater.* 21, 1207–1213 (2009).

29. Teshima, K. et al. The growth of highly crystalline, idiomorphic potassium titanoniobate crystals by the cooling of a potassium chloride flux. *CrystEngComm* 13, 1190–1196 (2011).
30. Shrout, T. R., Papet, P., Kim, S. & Lee, G.-S. Conventionally Prepared Submicrometer Lead-Based Perovskite Powders by Reactive Calcination. *Journal of the American Ceramic Society* 73, 1862–1867 (1990).
31. Fang, M. et al. Layer-by-Layer Growth and Condensation Reactions of Niobate and Titanoniobate Thin Films. *Chem. Mater.* 11, 1526–1532 (1999).
32. Rebbah, H., Desgardin, G. & Raveau, B. Les oxydes  $ATiMO_5$  : Echangeurs cationiques. *Materials Research Bulletin* 14, 1125–1131 (1979).
33. Inoue, K., Suzuki, S. & Nagai, M. Ion exchanged potassium titanoniobate as photocatalyst under visible light. *J Electroceram* 24, 110–114 (2010).
34. Colin, J.-F., Pralong, V., Hervieu, M., Caignaert, V. & Raveau, B. Lithium Insertion in an Oriented Nanoporous Oxide with a Tunnel Structure:  $Ti_2Nb_2O_9$ . *Chem. Mater.* 20, 1534–1540 (2008).
35. Tournoux, M., Marchand, R. & Brohan, L. Layered  $K_2Ti_4O_9$  and the open metastable  $TiO_2(B)$  structure. *Progress in Solid State Chemistry* 17, 33–52 (1986).
36. Kumada, N. & Kinomura, N. Preparation and crystal structure of new potassium niobium oxides:  $K_2M_2Nb_4O_{13}$  ( $M = Mg, Fe$ ). *Materials Research Bulletin* 32, 559–567 (1997).
37. Rebbah, H., Desgardin, G. & Raveau, B. Nonstoichiometric oxides with a layer structure: The compounds  $A_{1-x}(Ti_{1-x}M_{1+x})O_5$ . *Journal of Solid State Chemistry* 31, 321–328 (1980).

38. Uma, S. Structural Diversity in Complex Layered Oxides. in Handbook of Solid State Chemistry 571–594 (American Cancer Society, 2017).  
doi:10.1002/9783527691036.hsscvol1020.
39. Cui, H. et al. Three-dimensional printing of piezoelectric materials with designed anisotropy and directional response. Nature Materials 18, 234–241 (2019).
40. Shrout, T. R., Chang, Z. P., Kim, N. & Markgraf, S. Dielectric behavior of single crystals near the  $(1-X)$   $\text{Pb}(\text{Mg}^{1/3}\text{Nb}^{2/3})\text{O}_3$  -  $(x)$   $\text{PbTiO}_3$  morphotropic phase boundary. Ferroelectrics Letters Section 12, 63–69 (1990).
41. Lin, C. et al. Defective  $\text{Ti}_2\text{Nb}_{10}\text{O}_{27.1}$  : an advanced anode material for lithium-ion batteries. Scientific Reports 5, 17836 (2015).
42. Zhang, Q., Pan, W., Bhalla, A. & Cross, L. E. Electrostrictive and Dielectric Response in Lead Magnesium Niobate–Lead Titanate (0.9PMN · 0.1PT) and Lead Lanthanum Zirconate Titanate (PLZT 9.5/65/35) under Variation of Temperature and Electric Field. Journal of the American Ceramic Society 72, 599–604 (1989).

## CHAPTER 4: PRE-CERAMIC POLYMERS FOR HIGH-TEMPERATURE FUNCTIONAL MATERIALS

### 4.1 Introduction

A key benefit of additive manufacturing (AM) is the fabrication of ultra-light structures via lattices.<sup>1</sup> Two key fields where such ultra-light structures could have major application are aerospace and automotive fields. However, aerospace and automotive fields often require high strength and high temperature performance (>500 °C). In such extreme environments, acrylate polymers typical of light-based AM are not suitable. Ceramics offer several highly desirable properties, including high strength and high temperature and are common in aerospace and automotive applications. Additionally, their brittle nature prevents subtractive manufacturing into high-resolution (<100 micron) structures. Additive manufacturing, via particle composites or polymer derived ceramics has allowed the fabrication of complex, ultra-light ceramics with dense structural features.<sup>1-3</sup> For light-based AM, polymer derived ceramics (PDCs) are the most successful and straightforward way to manufacture ceramics, though they are limited to silicon oxycarbide (SiOC) ceramics.<sup>4,5</sup> However, doping of SiOC with metal ions or nanomaterials, has previously been used to produce a variety of functional ceramic materials, including magnetic, and piezoresistive by in-situ formation of functional ceramics (silicides, carbides, oxides) during PDC pyrolysis.<sup>6-10</sup> Doped SiOC ultra-light ceramic structures could offer a unique platform for aerospace and automotive sensors, with minimal weight gain, but all previous AM ceramics are structural in nature. No fully-dense functional ceramics have been reported for light-based AM to our knowledge.<sup>1-5</sup>

Here we first formulate and demonstrate a thiol-ene based PDC ceramic for stereolithography. We then extend this to two different doped PDC ceramics that can be fabricated into various complex shapes. In combination with rapid sintering, these doped PDCs maintain their functionality and form a high temperature piezoresistive sensor.

#### **4.2 Formulation of Thiol-ene Stereolithography PDC**

Thiol and vinyl siloxanes as well as acrylate based siloxanes are readily available from commercial sources. We focused on high-crosslink density to achieve small features sizes. Due to their previous success for PDC AM,<sup>4</sup> we focused on thiol-ene based siloxanes, with very high (>99%) functionality and thiol and vinyl respectively. Combining thiol and vinyl siloxanes makes for a readily photo-initiated click-based thiol-ene resin.<sup>11</sup>

Using a custom-made stereolithography system, **Figure 4-1**, a variety of complex structure could be fabricated using the thiol-ene based PDC. This includes octet-trusses which survived the pyrolysis to produce SiOC ceramic lattices. Pyrolysis was carried out in a tube furnace ramping at 1°C/min, holding at 1000°C for 1hr, and then ramping to room temperature at 3°C/min under ultra-high purity Argon.

Thermogravimetric analysis (TGA) on the thiol-ene resin and results are show in Figure 4-1C. Key to PDC success is the high-conversion to solids at high temperature. Excessive burnout of polymers to carbon dioxide, water, etc. during pyrolysis can lead to part failure. The thiol-ene resin, gives approximately 60wt% ceramic after conversion at 1000 °C which similar to previous reported thiol-ene PDCs.<sup>4</sup> The final elemental analysis via scanning electron microscopy – energy

dispersive X-ray spectroscopy (SEM-EDX) shows the expected SiOC elemental distribution, similar to previous reports.<sup>4</sup> Parts experienced 34% linear shrinkage during pyrolysis.<sup>12</sup>

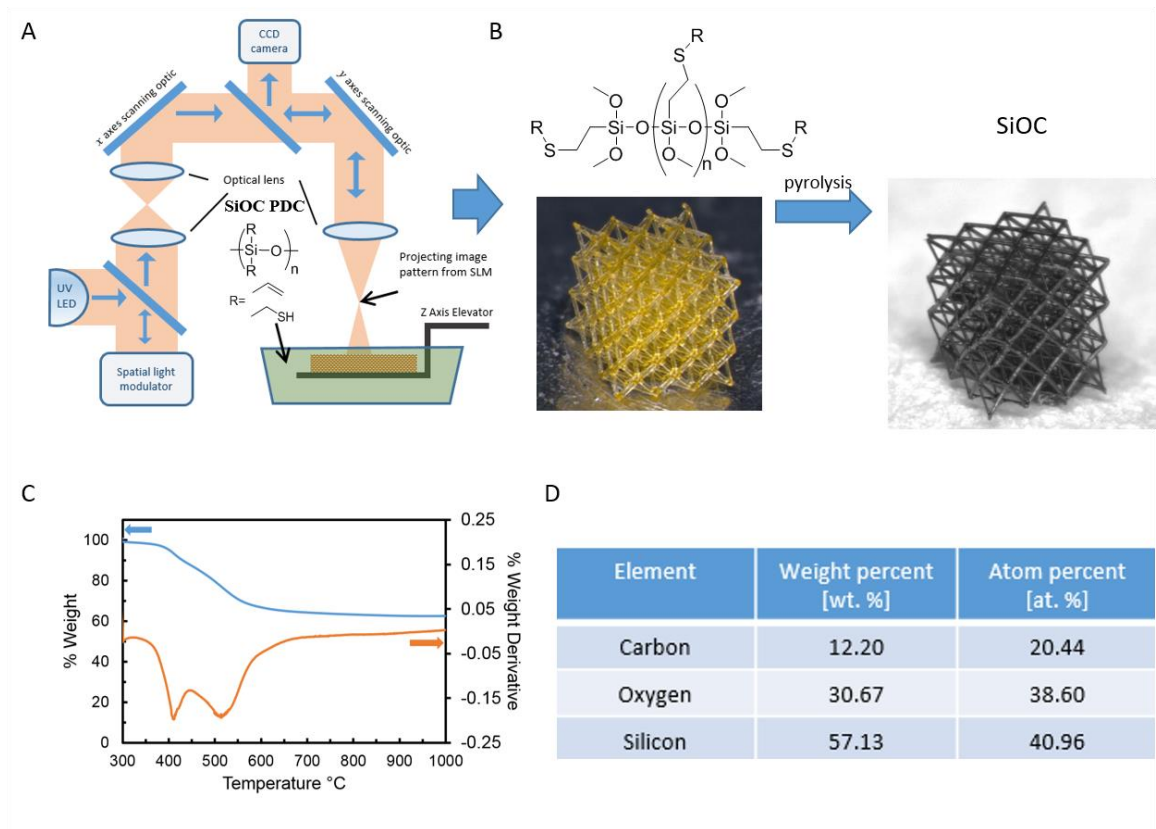


**Figure 4-1: PμSL of Ceramic** A) Schematic of projection stereolithography of pre-ceramic polymers B) Structure of thiol-ene siloxane and micro-gear “green” part in orange, and the pyrolyzed form imaged with SEM in gray C) TGA of thiol-ene PDC resin D) SEM-EDX of final pyrolyzed ceramic showing element content

### 4.3 Functional SiOC 3D Ceramics via Doping

Previous reports have noted that doping of SiOC can lead to functional properties including high piezoresistance (change in conductivity with strain) and magnetism.<sup>6-10</sup> Combining functional SiOC carbide ceramics, with multi-material printing could open a new platform for high-temperature device manufacturing. Printed structures with spatially-distributed different compositions at a micro- and nano-scale would create range of application with useful mechanical and thermal properties.

A significant drawback to this method, is the ideal composition need to be locally maintained after co-sintering. Cross-diffusion and difference in shrinkage and sintering time/temperature for different components may limit our methods. Therefore, we have collaborated with a group at University of Maryland, managed by Liangbing Hu, to use rapid sintering (~1 min total) to fabricate doped SiOC ceramics, with minimal cross-diffusion.<sup>13</sup>

The metal doping comes from the respective metal salts. Initially, the thiol-ene SiOC resin was used, however, it was found cobalt salts were not soluble. Therefore, a alkoxy-silane based SiOC resin, similar to previously reported methods, was used, **Figure 4-2**.<sup>5</sup> Aluminum alkoxides were soluble in the previously reported thiol-ene SiOC resin. To demonstrate the sintering capability, we 3D printed multi-material honeycomb structures featuring aluminum (Al) doped SiOC (for piezoresistivity response) and cobalt (Co) doped SiOC (for magnetic responses), which appear as green and orange respectively in Figure 4-2B. The rapid sintering (under argon) rapidly decomposes the SiOC and metal salt to form metal-doped ceramics, while maintain 3D structure, Figure 4-2C. Refer to reference 13 for full details on rapid sintering procedure.

Critically, the rapid sintering minimizes the diffusion of Al and Co as detected by SEM-EDX mapping, Figure 4-2D. This minimizes cross-talk and contamination in the respective domains particularly when compared to conventional sintering (1 C/min, 1000C 1h) where we see excessive cross-diffusion in Figure 4-2E.

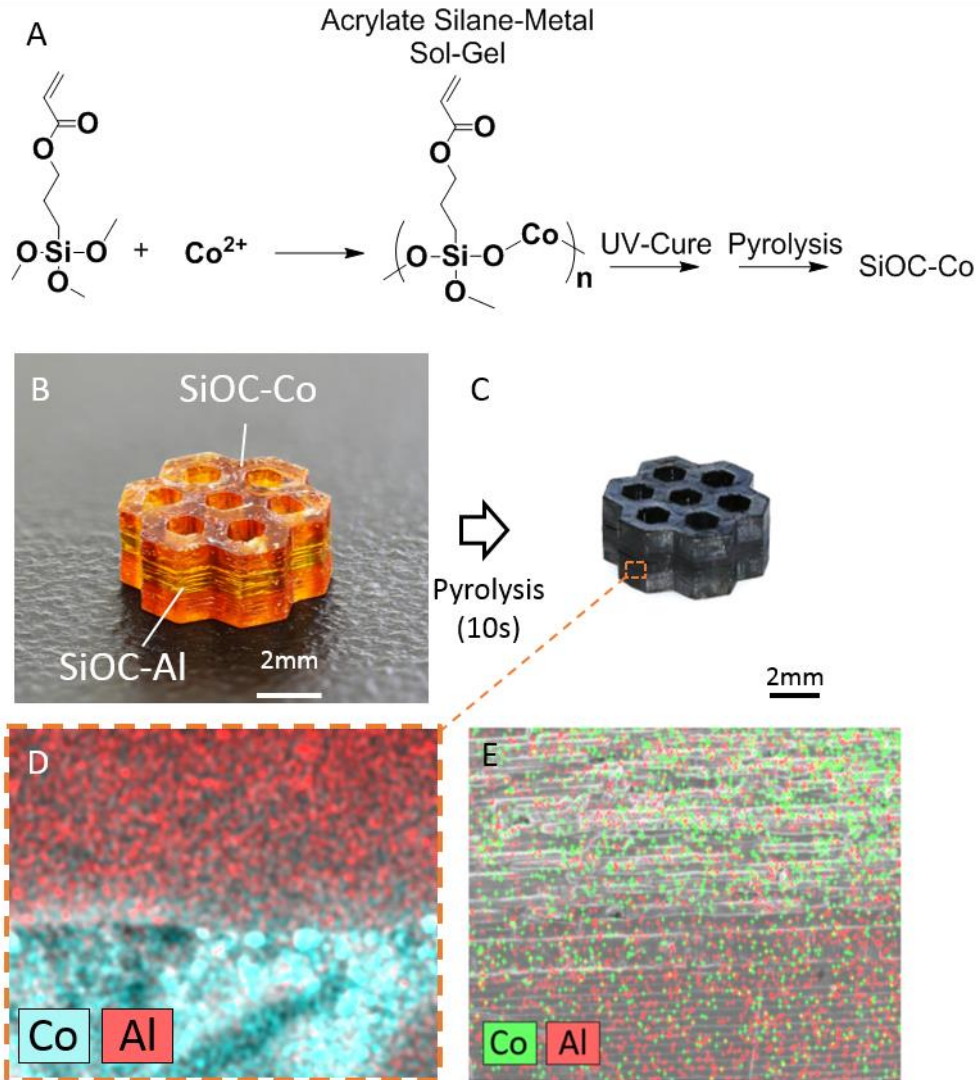


**Figure 4-2: Doped SiOC for Functional 3D Ceramics** a) Schematic for forming metal doped SiOC ceramics b) Photographs of the multi-material SiOC green parts printed with cobalt

doped (magnetic) resin in orange, and aluminum doped (piezoresistive) in green. c) Photographs of the multimaterial SiOC samples sintered by the rapid sintering method showing the uniform shrinkage and maintained structures. d) SEM-EDX of the rapid sintered SiOC-Co and SiOC-Al doped interface showing minimal cross-diffusion due to rapid nature of sintering. e) SEM-EDX of conventional sintered SiOC-Co and SiOC-Al showing significant diffusion

The results demonstrate that rapid-sintering is an effective method to achieve a multi-phase structure without cross-doping due to the short sintering time (10 s), fast heating (6000 °C /min), and cooling (10000 °C /min) rates. Meanwhile, the conventional sintering method results in heavy diffusion of the two materials.

My colleague Huachen Cui, demonstrated a the SiOC multi-material sample as a high-temperature sensor. First, comparing the rapid and conventional sintered samples, rapid sintering shows a clearly higher piezoresistive response than conventional sintering, due to the minimization of diffusion **Figure 4-3**. Then Huachen extended this to a piezo-magnetic sensor, since SiOC-Al is piezoresistive<sup>9</sup> and SiOC-Co is magnetic,<sup>10</sup> and under a magnetic field, due to the sandwich structure, Figure 4-3B the SiOC-Al piezoresistive layer undergoes compression and a change in its electrical resistance with proportion to the applied magnetic field. Figure 4-3C, at high and low temperature. This affirms that 3D printing can be used to make high-temperature ceramic functional devices.

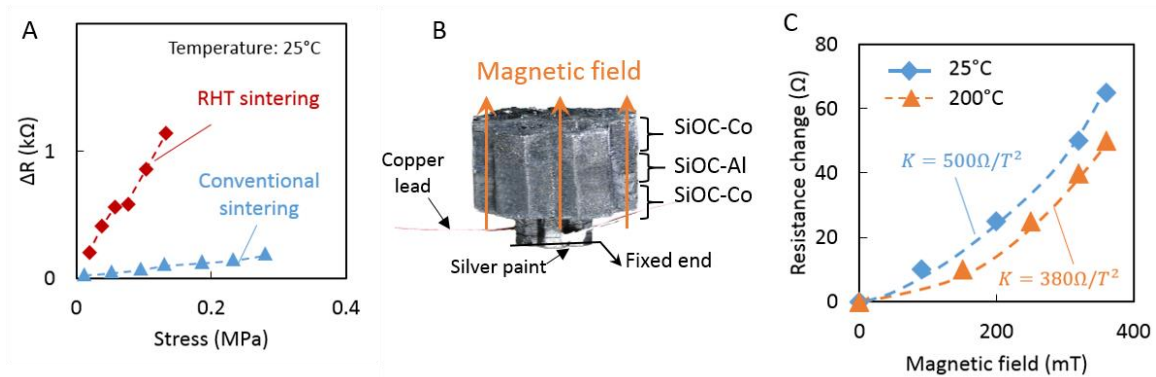


**Figure 4-3: Diffusion in Rapid vs Conventionally Sintered SiOC** a) layout of magnetic sensor testing b) Change in resistance of SiOC-Al piezoresistive layer with magnetic field at two different temperatures.

#### 4.4 Summary and Future Work

A thiol-ene based polymer derived ceramic formulation that can reach high-resolution ( $\sim 10 \mu\text{m}$ ) was developed. This is an order-of-magnitude increase in feature resolution to previously reported polymer derived ceramic light-based 3D printed structures. Formulation of functional polymer derived ceramics were also successfully developed. Multi-material printing and rapid sintering of these samples produced a functional magnetic sensor via piezoresistive effect. The rapid sintering is critical to prevent cross-diffusion and maintain proper phases within the part. This sensor can function at high temperatures ( $>200 \text{ }^\circ\text{C}$ ) and opens opportunities for 3D printed high-temperature functional devices. Future work should focus on developing other functional polymer derived ceramic formulations based on those here (semiconductor, metallic conductor, etc.) and the use of rapid sintering to make 3D functional devices. The upper limit of temperature these devices can survive should also be explored.

#### **4.5 Acknowledgements**

Portions of this dissertation chapter have been published in a revised form in Huachen Cui, Ryan Hensleigh, Hongshun Chen, Xiaoyu Zheng, Additive Manufacturing and size-dependent mechanical properties of three-dimensional microarchitected, high-temperature ceramic metamaterials, *Journal of Material Research*, 2018, Volume 33, pp. 360-371, DOI: <https://doi.org/10.1557/jmr.2018.11>, see reference 12. This version is published under a Creative Commons CC-BY-NC-ND. No commercial re-distribution or re-use allowed. Derivative works cannot be distributed. © copyright holder.

Portions of this dissertation chapter have been published in a revised form in Chengwei Wang, Weiwei Ping, Qiang Bai, Huachen Cui, Ryan Hensleigh, Ruiliu Wang, Alexandra H. Brozena, Zhenpeng Xu, Jiaqi Dai, Yong Pei, Chaolun Zheng, Glenn Pastel, Jinlong Gao, Xizheng Wang, Howard Wang, Ji-Cheng Zhao, Bao Yang, Xiaoyu (Rayne) Zheng, Jian Luo, Yifei Mo, Bruce Dunn, Liangbing Hu, A general method to synthesize and sinter bulk ceramics in seconds, *Science*, 2020, Volume 368, pp. 521-526, DOI: <https://doi.org/10.1126/science.aaz7681>, see reference 13. No commercial re-distribution or re-use allowed.

#### **4.6 Materials and Methods**

Vinylmethoxysiloxane homopolymer (VMM-010), (Mercaptopropyl)methylsiloxane homopolymer (SMS-992), and Aluminum N-nitrosophenylhydroxylamine (AKA076, ANPHA) were purchased from Gelest. (trimethoxysilyl)propyl methacrylate (TMSPM), aluminum

isopropoxide, ethanol, acrylic acid (AA), phenylbis(2,4,6-trimethylbenzoyl)phosphine oxide (Irg819), Sudan I, and cobalt nitrate hexahydrate were purchased from Sigma-Aldrich. Genocure TPO-L was generously donated by Rahn.

Thiol-ene SiOC resin consisted of 10g of VMM-010 and 10g SMS-992, 0.4g (2 wt%) TPO-L, 0.01g (0.05 wt%) Sudan I, and 0.002g (0.01 wt%) ANPHA. Stored in opaque bottle and fridge to maintain shelf life.

To make Al-doped thiol-ene SiOC resins, combine and thoroughly mix 10g of Gelest SMS-992 with 1g TMSPM, 2g aluminum-tri-sec-butoxide, and 0.01g Sudan I. The solution was then mixed with 10g Gelest VMM-010, and 0.4g TPO-L.

To make Co-doped magnetic SiOC resins, mix 2 g of DI water and 0.08 g of hydrochloric acid 37%. Separately, thoroughly mix 6g ethanol, 28.3 g of TMSPM, 0.975 g of AA, and 3.3 g of cobalt nitrate hexahydrate. Dropwise add HCl solution to the TMSPM mixture under vigorous stirring, followed by heating at 100 °C for 2 h. After the heating, 0.56g of Irg819 and 0.014g Sudan I were added and dissolved. Store in opaque bottle and fridge to improve shelf-life.

Refer to reference 13 for further details on multi-material stereolithography and rapid sintering. Conventional sintering was done in Across International T1700 furnace under ultra-high purity Argon gas.

## 4.7 References

1. Zheng, X. et al. Ultralight, ultrastiff mechanical metamaterials. *Science* 344, 1373–1377 (2014).
2. Jang, D., Meza, L. R., Greer, F. & Greer, J. R. Fabrication and deformation of three-dimensional hollow ceramic nanostructures. *Nature Materials* 12, 893–898 (2013).
3. Meza, L. R., Das, S. & Greer, J. R. Strong, lightweight, and recoverable three-dimensional ceramic nanolattices. *Science* 345, 1322–1326 (2014).
4. Eckel, Z. C. et al. Additive manufacturing of polymer-derived ceramics. *Science* 351, 58–62 (2016).
5. Zanchetta, E. et al. Stereolithography of SiOC Ceramic Microcomponents. *Advanced Materials* 28, 370–376 (2016).
6. Stabler, C., Ionescu, E., Graczyk-Zajac, M., Gonzalo-Juan, I. & Riedel, R. Silicon oxycarbide glasses and glass-ceramics: “All-Rounder” materials for advanced structural and functional applications. *Journal of the American Ceramic Society* 101, 4817–4856 (2018).
7. Ionescu, E., Kleebe, H.-J. & Riedel, R. Silicon-containing polymer -derived ceramic nanocomposites (PDC-NCs): preparative approaches and properties. *Chemical Society Reviews* 41, 5032–5052 (2012).
8. Encheva, G. et al. Silica gels containing transition metal oxides. *Journal of Non-Crystalline Solids* 345–346, 615–619 (2004).
9. Cao, Y. et al. Giant piezoresistivity in polymer-derived amorphous SiAlCO ceramics. *Journal of materials science* 51, 5646–5650 (2016).

10. Hauser, R., Francis, A., Theismann, R. & Riedel, R. Processing and magnetic properties of metal-containing SiCN ceramic micro- and nano-composites. *J Mater Sci* 43, 4042–4049 (2008).
11. Lowe, A. B. & Bowman, C. N. *Thiol-X Chemistries in Polymer and Materials Science*. (Royal Society of Chemistry, 2013).
12. Cui, H., Hensleigh, R., Chen, H. & Zheng, X. Additive Manufacturing and size-dependent mechanical properties of three-dimensional microarchitected, high-temperature ceramic metamaterials. *Journal of Materials Research* 33, 360–371 (2018).
13. Wang, C. et al. A general method to synthesize and sinter bulk ceramics in seconds. *Science* 368, 521–526 (2020).

## CHAPTER 5: PATTERNED DEPOSITION TO INTEGRATE 3D STRUCTURES INTO ELECTRICAL DEVICES

### 5.1 Introduction

While I have reviewed my work developing several 3D device systems in other chapters, graphene aerogels for energy storage, piezoelectric composites for sensors and actuators, and doped silicon-oxycarbide for high-temperature sensors. There is a glaring gap that while we are able to fabricate these 3D devices components, ultimately there is no way to integrate them with current 2D device layouts. In a complex 3D sensor, for example, there could be multiple elements within the 3D topology, which are inaccessible to external connection e.g. wire leads. The workhorse of traditional electronics fabrication, lithography, is not compatible with complex 3D substrates/structures with embedded elements. The few demonstrations of lithography for 3D structures, are complex, and limited.<sup>1-3</sup> The 3D structure will inevitably have shadowed and inaccessible areas to external beams. 3D device integration needs to be considered *ab initio*.

The majority of 3D device fabrication relies on 3D printing.<sup>4-6</sup> For light-based 3D printing, integrating functional materials is extremely limited. This is due to several inherent limitations, particularly the light-curable material requirement, and low viscosity (typically <10 Pa\*s). The most advanced 3D printed electronic device method, combines multiple distinct techniques (extrusion, metal writing, etc.), with each technique printing one materials for a specific function i.e. structural, conductive, etc. The multiple steps and disparate techniques requires extensive optimization, and the process is bespoke, limiting broad, flexible manufacturing.<sup>4,5</sup> In contrast, microfabrication is broadly flexible with many materials, substrates, and ultimately devices. New

methods are needed, in particular, ones which allow similar flexibility in materials and substrates to microfabrication (sputtering, etching, etc.).

Selective plating is a process which deposits metals in localized areas of a structure.<sup>7,8</sup> There are a variety of methods to achieve selective deposition. Many 2D demonstrations use charged polymers (polyelectrolytes) to selectively deposit metals, but most of these demonstrations have been strictly 2D, and quite simple. There have been methods to selectively plate structures in 3D, using inherent differences in reactivity,<sup>9</sup> using differences in reactivity of acrylate and methacrylate,<sup>10</sup> using differences in material conductivity,<sup>11</sup> using differences in etching rate of polymers to control surface functionality,<sup>12</sup> and one using charged and neutral polymers.<sup>13,14</sup> These all however are very simple demonstrations, the most complex being a metal 3D coil held by dielectric rods,<sup>10</sup> and beyond this, there are no demonstrated device applications. Additionally, all of these previous methods were limited to single materials depositions. Multi-material depositions will be required to reach significant device complexity.

## **5.2 Charge Programmed Deposition**

Herein a new method for 3D device fabrication which is called charge programmed deposition. The fundamental process is to combine polymer resins with distinct electric charge polarity (positive, negative, or neutral) based on their inherent chemical structure into a multi-material structure. For example negative monomers could include, carboxyl sulfate, or phosphate groups, positive could be tetramethylammonium or phosphonium groups, and neutral would consist of hydrocarbons, siloxanes, et cetera. Additive manufacture of these charged resins, allows one to pattern in 3D printing the substrate charge, making areas of positive, negative, and

neutral surface charge based on the initial resin polarity. Soaking these charge programmed structures in a solution that contains oppositely charged material will deposit the material only in the regions of opposite polarity due to electrostatic attraction. Areas of like-polarity and neutral areas will have no deposition. Because liquids can penetrate and carry deposition materials deep into complex 3D structures, surfaces previously inaccessible to external sources (e.g. lithography) can be patterned with deposition materials.

We focused the development of our method by using electroless deposition. Electroless deposition is a material deposition process whereby a catalyst adhering to a surface triggers an autocatalytic i.e. self-sustaining deposition reaction.<sup>15</sup> Once initiated deposition continues until reactants are consumed or the part is removed from the bath. Electroless deposition is ideal for our charged programmed methods, as the most common triggering catalyst, palladium (Pd) can form both positive (Pd<sup>+</sup>) and negative (Pd<sup>-</sup>) complexes in solution.<sup>7</sup> This allows us to use a single catalyst to pattern both positive and negative areas depending on the polarity of the catalyst. As the catalyst is required to initiate the reaction, deposition will only occur where Pd is adsorbed. An overview of this process is shown in **Figure 5-1**.

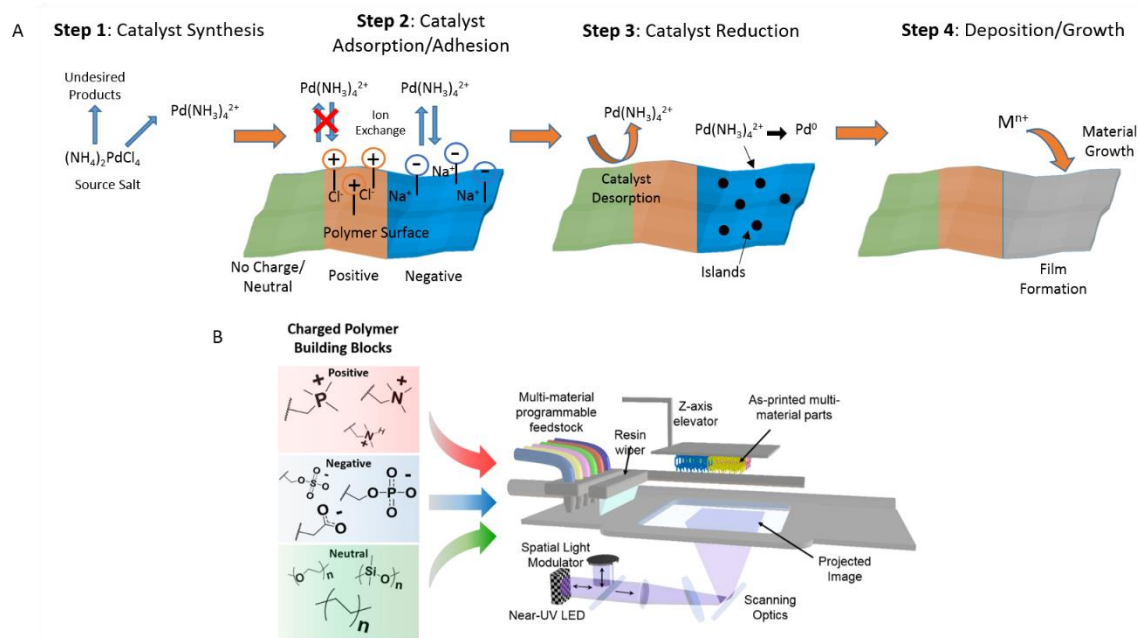


**Figure 5-1: Overview of Selective Deposition Process** a) A schematic overview of the selective deposition process from catalyst synthesis, to electrostatic attraction on polymer surface, reduction, and finally material/metal deposition. b) Schematic of Custom multi-material projection stereolithography system where fluidic system acts to switch charged building blocks and allow light-based manufacturing

Using scanning electron microscopy energy dispersive X-ray spectroscopy (SEM-EDX) the adsorption of Pd ions was monitored on a variety of surfaces, Figure 5-2. These surfaces were made by mixing commercially purchased acrylates (see Methods) of various charges as previously discussed, and acrylate crosslinkers. The charged monomer comprised at least 50wt% of the photopolymer mixture and films were cured between glass slides with a tape spaces, and were nominally 200 microns in thickness.

The films were soaked in freshly made Pd catalyst solution for fixed amounts of time and then dabbed dry with a Kimwipe to remove all solution. These were then measured via SEM-EDX. The resulting elemental analysis confirms the hypothesis, Pd catalyst salts are highly selective for their oppositely charged substrates **Figure 5-2**. There is a clear increase in Pd SEM-EDX peak (Figure 5-2C) on negatively charged films after soaking in Pd+ catalyst solution (red line) after only 30 seconds compared to bare film before soaking (blue line). By comparison, soaking of like charged and neutrally charged resin films in Pd+ (Figure 5-2D) for 24 hours, does not yield any measurable peak. This is true for the Pd- catalyst as well, where 30s of soaking a positively charged film yields a significant peak compared to bare film (Figure 5-2E). Like charged and neutrally charged have no measurable Pd after 30 minutes of soaking (Figure 5-2F).

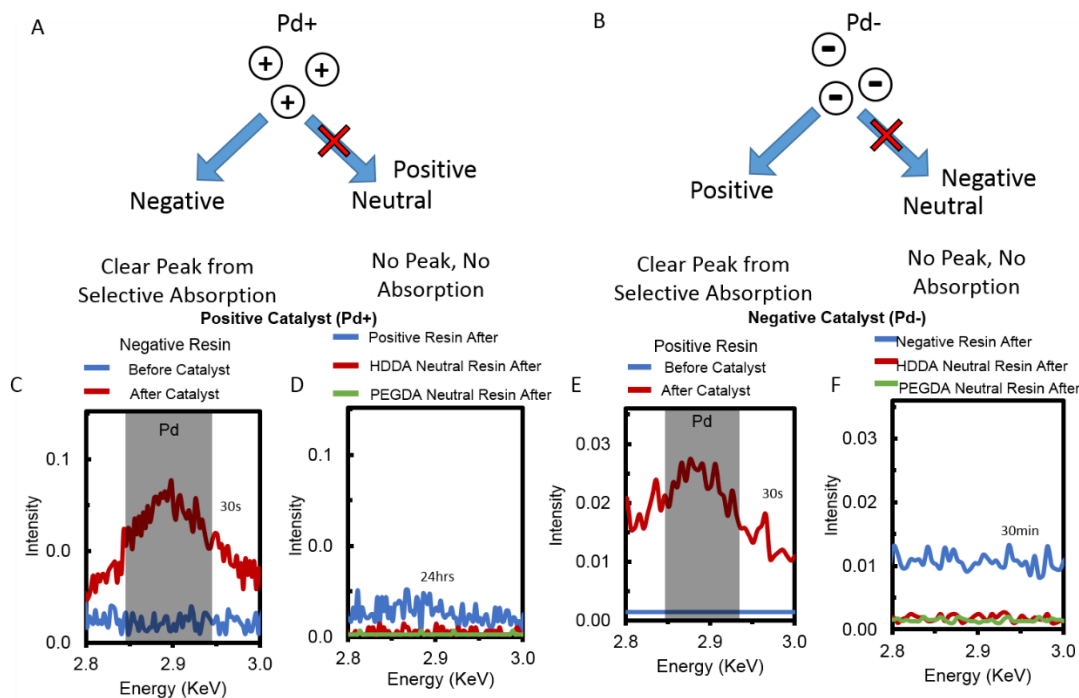


**Figure 5-2: Catalyst Selectively from Surface Polarity** The charged catalysts adsorption was monitored via SEM-EDX on photopolymer resins of various surface charges

Electroless deposition is capable of depositing a variety of materials including nickel-phosphorus (Ni-P), copper (Cu), zinc oxide (ZnO),<sup>16</sup> magnetite (Fe<sub>3</sub>O<sub>4</sub>),<sup>17</sup> and others.<sup>18</sup> **Figure 5-3** shows the programming of Ni-P to various areas of octet-truss. In confirmation of our hypothesis, by varying the charged resins within the 3D CAD design/printed part, we are able to localize Ni-P deposition. We do not detect any Ni-P deposition outside of these areas, as the Pd catalyst is required to initiate the reaction.

The selective deposition resolution was tested using an Air Force Resolution Target, which has a series of numbers, vertical and horizontally spaced lines with decreasing size. The process works down to the resolution limit of our multi-material 3D printing process. Beyond this our printing process could not resolve the features clearly. However, previous work using a similar selective deposition process with block-co-polymers, showed that well controlled electroless deposition could successfully plate nano-scale domains (~100nm).<sup>19</sup>

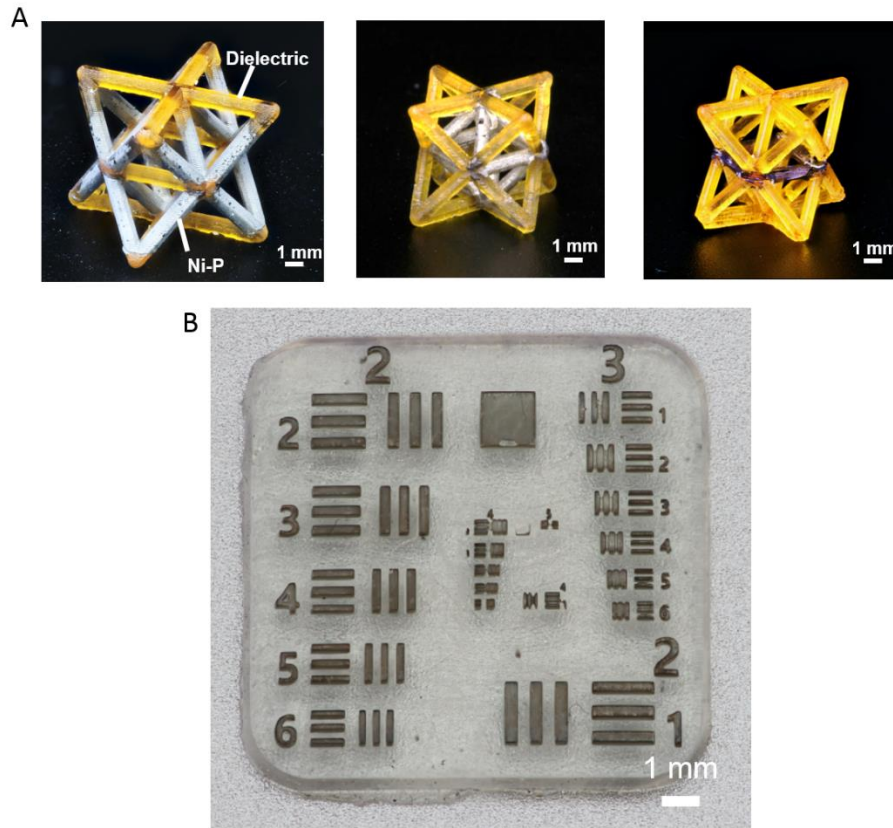


**Figure 5-3: Deposition Programming and Resolution** a) Octet-truss with different areas selectively deposited with Ni-P metal b) Air Force Resolution Target, the charge programmed deposition reaches the resolution limit of the printing system

The electroless deposited Cu metal is fairly conductive, but can be improved with electroplating of copper. As electroplating requires a conductive substrate, it is also localized only to the previously deposited electroless areas. We measured the conductivity of our samples via 4-point-probe method, **Figure 5-4**. With Cu electroplating our features achieve high conductivity,  $1.2 E^7$  S/m, which is nearly that of bulk Cu,  $5.96 E^7$  S/m.<sup>20</sup> The electroplating increases the thickness of the deposits into the several micron range, Figure 5-4C.

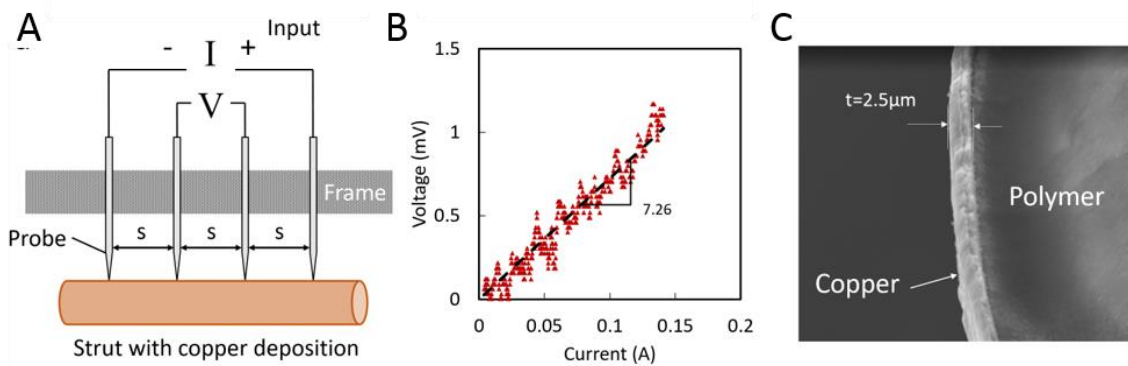


**Figure 5-4: Conductivity Measurement** a) Schematic of the four-point probe. b) Voltage as a function of the applied current. c) SEM image showing the cross-section of the fractured strut with copper deposition.

### 5.3 Multi-Material Deposition

As previously mentioned, the wide variety of electroless materials opens many opportunities, but if we are to approach the complexity of microfabrication, multiple deposition will be required. A key advantage of charged programmed deposition presented here, is that by combining both positive, negative, and neutral with the positive or negative Pd catalysts, multimaterial deposition are possible, **Figure 5-5**. Essentially one would repeat the selective deposition process twice, and if there is side reactions with previously deposited materials, which previous papers have shown, multimaterial deposition are possible.

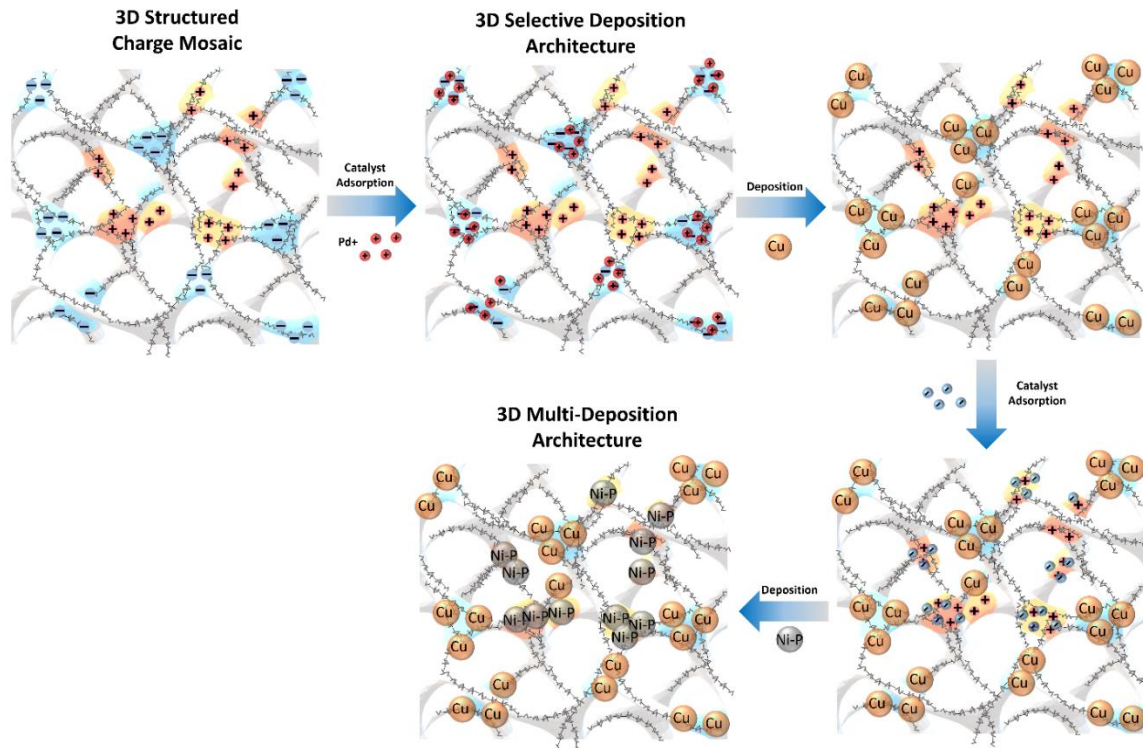


**Figure 5-5: Schematic Multi-material deposition** Overview of multi-material deposition process, first depositing one material via selective catalyst adsorption, the process is repeated to deposit a 2<sup>nd</sup> material.

Multi-material deposition are shown in **Figure 5-6** including magnetite/Cu (6A), and Ni-P/Cu (6B). Such depositions have never been previously demonstrated in 3D to the author's knowledge and open significant opportunities for metamaterials and other functional devices. There is no detected cross-contamination between the deposited areas.

Beyond electroless methods, it is also possible to electrostatically deposit other materials. For example, multi-walled carbon nanotubes (MWCNTs) can be dispersed in aqueous solutions with charged surfactants.<sup>21</sup> Using a 1wt% MWCNT solution dispersed in water with a common

positively charged surfactant (CTAB, see methods), the MWCNTs selectively deposit to their electrostatically opposite substrates, Figure 5-6C. After ambient drying overnight, the MWCNTs mats exhibit electrical conductivity of 1000 S/m, which is typical for MWCNTs.

To test the crystallinity of the deposited magnetite ( $\text{Fe}_3\text{O}_4$ ) and ZnO, X-ray diffraction (XRD) was used. Solutions were made, as described in the methods section ( $\sim 20\text{g}$ ), and a small ( $0.02\text{g}$ ) amount of  $\text{Pd}^+$  solution was added to initiate the electroless process. This was repeated several times and powders were centrifuged out of solution, washed with water multiple times, washed with acetone, and left to dry overnight. XRD reveals the structure are of the correct crystalline structure based on previous reports, Figure 5-6D and E.<sup>16,17</sup>

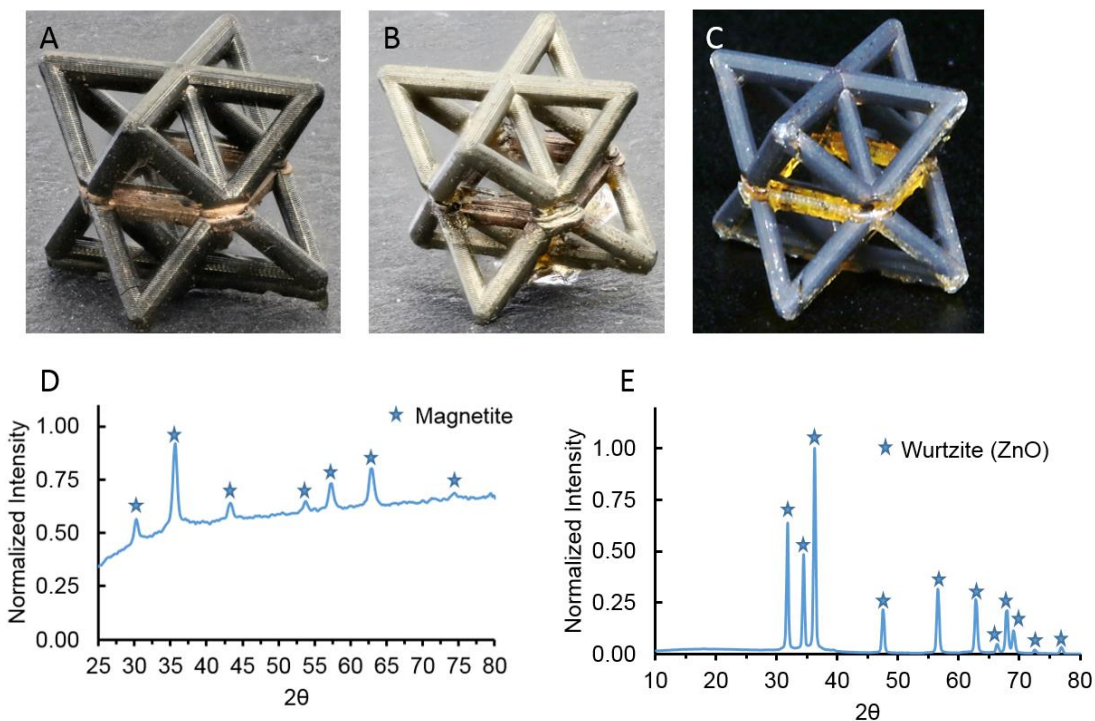


**Figure 5-6: Multi-Material Deposition** a) Multi-deposition octet-truss combining Cu and magnetite ( $\text{Fe}_3\text{O}_4$ ). b) Ni-P and Cu multi-deposition octet-truss. c) Selectively plated carbon

nanotubes with charged surfactant CTAB **d)** Electroless magnetite ( $\text{Fe}_3\text{O}_4$ ) XRD showing proper crystal structure **e)** Electroless ZnO XRD showing proper crystal structure

#### 5.4 Composites and Devices

My colleague Huachen Cui has also tested, and found it is also possible to composite the underlying structural or plating polymer with powders to form a composite. As the selective deposition is confined to the surface, the underlying composite properties are independently tunable. For example, compositing of polyethyleneglycol diacrylate (PEGDA) polymer which is used as the neutral polymer throughout this work and has a low dielectric constant (~2-3), combined with lead-zirconate-titanate (PZT) a high dielectric constant powder, we can increase the dielectric properties of the underlying composite by several orders-of-magnitude, **Figure 5-7.**<sup>22,23</sup> Variation of the dielectric constant is critical for electromagnetic applications. Other material combinations, such as magnetic, thermal, or other are also possible.

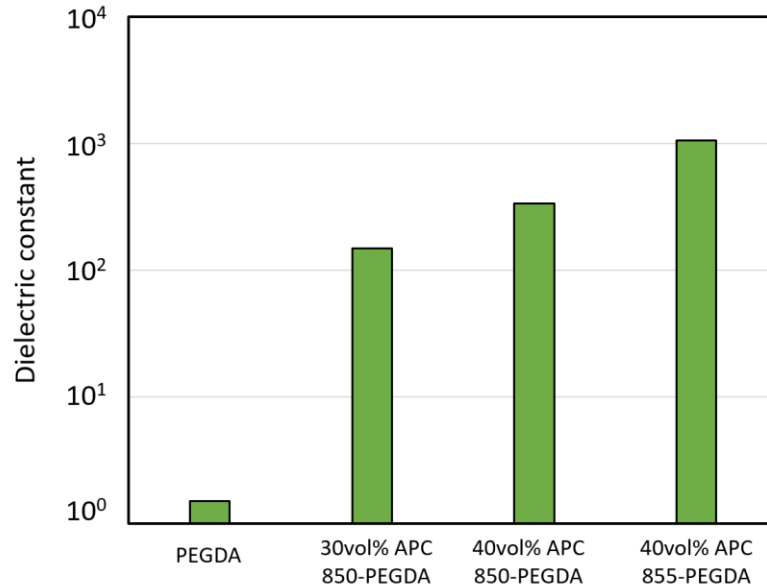


**Figure 5-7: Tunable Dielectric Constant** Dielectric constant of our unplated sections can vary from ultra-low (~2) to ultra-high (1000) by compositing with PZT ceramic (APC850 or APC855) or other nanoparticle inclusions.

My colleague Huachen Cui and I have combined the selective deposition with our piezoelectric composite work (Chapter 3). By selectively depositing metals within our 3D piezoelectric-polymer composites we are able to form functional devices including a tactile and impact sensor, **Figure 5-8**. These sensors could be combined to form a flexible advanced prosthetic or soft-robot, with much simpler fabrication than previous demonstration. Currently, most electronic skins/wearables (e-skin) are manufactured with multi-step microfabrication procedures (deposition, lithography, etching, etc.) which is a time-consuming process. The rapid, one-step process we have developed here could allow bench-top fabrication of such devices in more rapid cost-effective manner. It is also the first demonstration of integrating sensors within a

complex structure without embedding them. This allows us to remotely measure impact in a much more simplified manner, than previously.

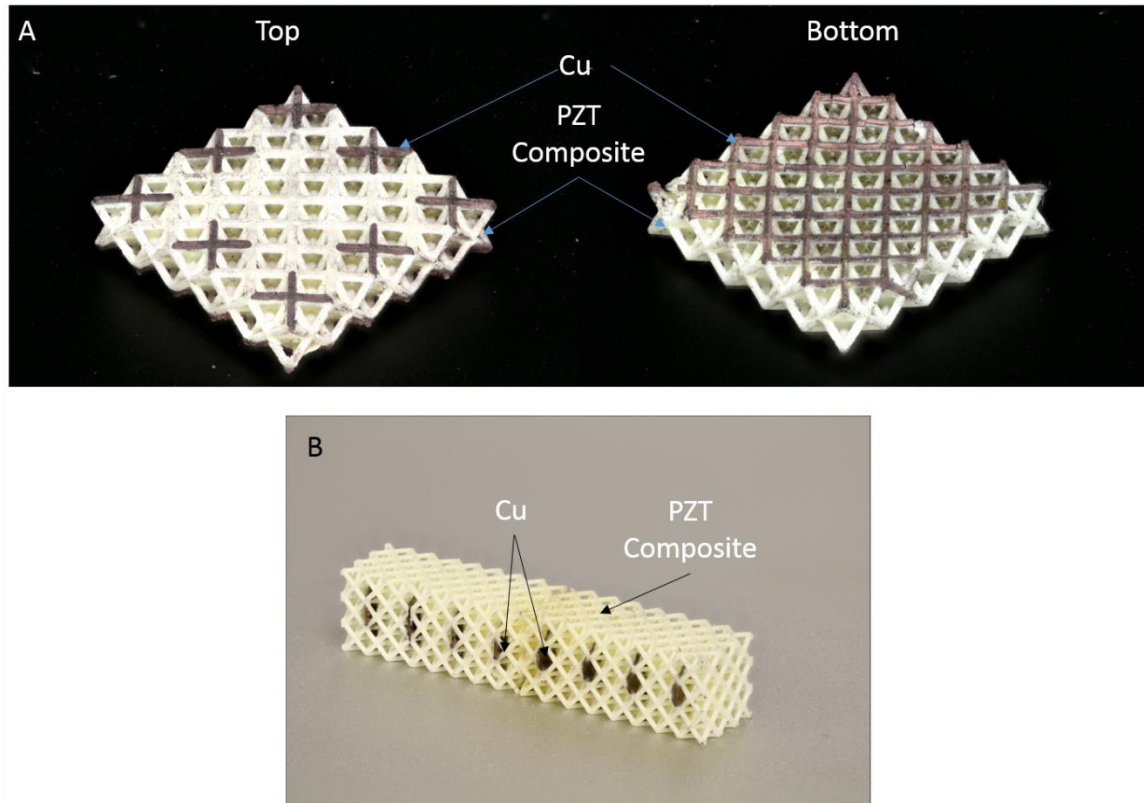


**Figure 5-8: Selectively Deposited Piezoelectric Devices** a) A tactile sensor where Cu electrode pixels were selectively deposited on an octet-truss lattice, the bottom of the same structure is completely coated with the counter electrode b) A piezoelectric octet-truss lattice with embedded Cu electrodes.

## 5.5 Ongoing Work

The primary application focus going forward is in applying this work to antennas. My colleague Zhenpeng Xu and I are collaborating with Anastasios Papathanasopoulos and Junbo Wang of the Rahmat-Samii group at UCLA to demonstrate practical antennas using selective deposition, **Figure 5-9**. Their antenna designs cannot be fabricated by other methods, and are ultra-light which is critical for space applications. Our methods and can provide a fruitful new field of 3D metal-dielectric antenna which will be explored.

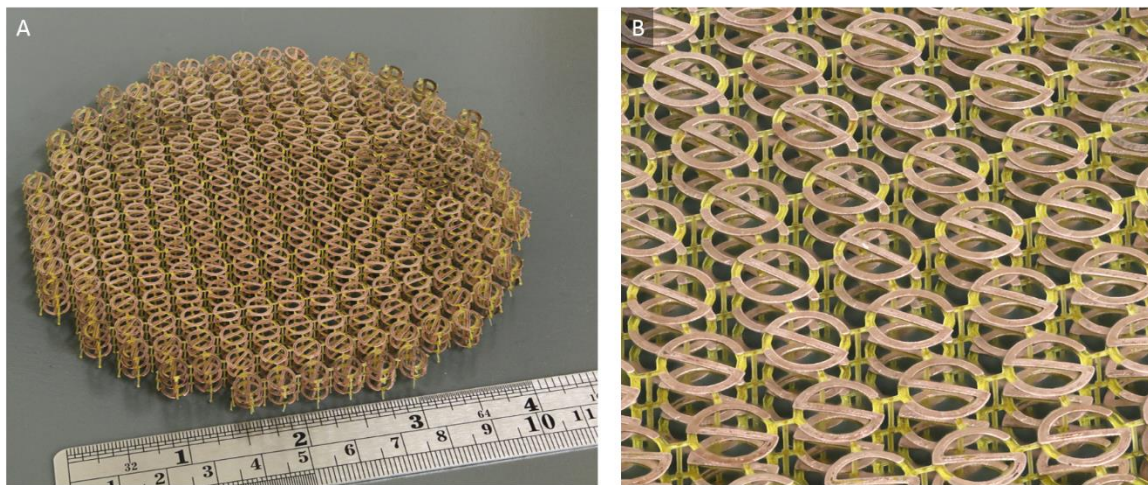


**Figure 5-9: Selective Deposition for Antennas** a-b) Antenna array with orange dielectric and selective copper coating

## 5.6 Summary and Future Work

The hypothesis that charged surfaces can be used to selectively deposit oppositely charged materials is confirmed. This process was used to demonstrate a variety of material deposition (metals, ceramics, semiconductors, magnetic materials, etc.) and also multiple depositions within

the same structure were demonstrated. Future work should focus on applying this technique towards practical devices where complex 3D metal-dielectric layouts are required.

### **5.7 Acknowledgements**

Portions of this dissertation chapter have been published in a revised form in Ryan Hensleigh, Huachen Cui, Zhenpeng Xu, Jeffrey Massman, Desheng Yao, John Berrigan, Xiaoyu Zheng, Charge-programmed three-dimensional printing for multi-material electronic devices, Nature Electronics, Volume 3, Issue 4, pg. 216-224, DOI: <https://doi.org/10.1038/s41928-020-0391-2>, see reference 22. No commercial re-distribution or re-use allowed. Derivative works cannot be distributed.

Portions of this chapter are in preparation for publication.

## 5.8 Materials and Methods

Bis[2-(methacryloyloxy)ethyl]phosphate (PDD), [2-(Acryloyloxy)ethyl]trimethylammonium chloride solution 80wt% in H<sub>2</sub>O (TMAA), Bisphenol A glycerolate dimethacrylate (BisGMA) Trimethylpropane triacrylate (TMPTA), polyethylene glycol diacrylate Mn~250 (PEGDA), 1,6-hexanediol diacrylate (HDDA), Phenylbis(2,4,6-trimethylbenzoyl)phosphine oxide (Irg819), Sudan (I), Sodium tetrachloropalladate (II) (Pd<sup>-</sup>), Tetraaminepalladium (II) chloride monohydrate (Pd<sup>+</sup>), Iron (III) nitrate nonahydrate, zinc nitrate hexahydrate, borane dimethylamine complex (DMAB), sodium dodecyl sulfate (SDS), 3-(Trimethoxysilyl)propyl methacrylate (TMSPM), glacial acetic acid, hydrochloric acid, and reagent grade sodium chloride (NaCl) were purchased from Millipore-Sigma. Ebecryl 242 and Ebecryl 114 were donated by Allnex. Multi-walled carbon nanotubes (MWCNTs) 20-30nm outer diameter were purchased from Cheaptubes. Piezoelectric nanoparticle lead zirconate titanate (PZT, APC855) was purchased from APC International.

Electroless metal plating solutions were purchased from Caswell Inc. and used as received: Electroless Copper Kit and Electroless Nickel. The Caswell provided catalysts i.e. “sensitizer” and “activator” solutions were not used.

### *Resin Formulations*

Negative resin: 5g of PDD, 5g TMPTA, 0.2g Irg819, 0.015g Sudan I

Positive resin: 5g TMAA, 5g BisGMA, 0.2g Irg819, 0.015g Sudan I

Neutral (TMPTA) resin: 10g TMPTA, 0.2g Irg819, 0.015g Sudan I

Neutral (PEGDA) resin: 10g PEGDA, 0.2g Irg819, 0.015g Sudan I

Neutral (HDDA) resin: 10g HDDA, 0.2g Irg819, 0.015g Sudan I

Piezoelectric resins: For piezoelectric resins and resins of varying dielectric constant, various amounts of PZT from 1-40 vol% are combined with PEGDA and then dispersed with a high-energy ball mill (Retsch) for 30 minutes based on work of Cui et al.<sup>23</sup> The wave mapping demo used a 3vol% functionalized PZT-PEGDA resin. To functionalize PZT add 0.5g PZT, 1.049g TMSPM, and 1.049g glacial acetic acid to 50g of DI water. Sonicate for 15 minutes, then reflux for 4 hours. Wash twice with water, once with ethanol, and then dry before dispersing via high-energy ball mill. The shape-sensing resin consisted of 20vol% of unfunctionalized PZT in PEGDA with 2wt% Irg819 (to polymer).

### *Solutions*

Solutions can be repeatedly used for 2 to 3 parts. Pd+ solution: 0.0282g Tetra-amine Palladium Chloride in 20g DI water. Solution is stable for at least 1 week. Pd- solution was made following Dressick et al.<sup>8</sup> First measure 0.0117g NaCl and set aside. Then add 0.0588g Sodium Tetrachloro Palladate in 20g DI water, vortexed 30s, then NaCl was immediately added and vortexed 1min. This solution is left to age 1 day before use. Solution is active for at least 1 month. DMAB solution: 0.0118g DMAB in 20g was used same day as made. Electroless Nickel-Phosphorus (Ni-P) was made per Caswell instruction and used same day as made. Electroless Copper (Cu) was made per Caswell instruction and used the same day as made. For large structures, the part was put in a container, and the amount of solution required to cover it was

found. The above solution were then scaled to those amounts. Pd<sup>+</sup> solution can be reduced to 75% (0.0212g in 20g DI) and then scaled to large amounts to reduce waste.

Magnetite deposition followed the work of Nakanishi et al.<sup>30</sup> 0.0177g (0.03M) DMAB and 0.0101g (0.0025 M) of iron (III) nitrate nonahydrate in 10g DI water. Solution should be used the same day as made.

Zinc oxide followed the work of Saito et al.<sup>32</sup> 0.2975g (0.05M) zinc nitrate hexahydrate and 0.0118g (0.01M) DMAB was added to 20g of DI water. Solution seems stable for at least a week, but was used same day as made.

Carbon Nanotube Deposition: 0.01g MWCNTs and 0.02g SDS were added to 10g DI water and sonicated. The black supernatant was used as is.

### ***Multi-material 3D Printing***

For large structures a commercial system Photon Mono X (ANYCUBIC) was used. Using this system, the printing was paused when a secondary material was needed. Without removing the structure from the substrate, the resin bath was removed, cleaned of resin, the structure was also cleaned with Kimwipes and ethanol. The second material was then added to the resin bath and printing continued as required based on the CAD model. This was repeated as needed for the entire structure.

To manufacture our structures, we utilize a custom made projection stereolithography system which integrated microfluidic control to add resin and wash/remove resin from the build chamber.<sup>22</sup>

### *Selective Deposition*

Once finished printing, parts were repeatedly washed with ethanol and dried on Kimwipes. A UV-post-cure was done, and large flat structure should be left on the substrate for this. The parts were then typically left overnight on the substrate to cure further from ambient light. Before plating parts were rinsed with DI water and dried with Kimwipe

First seed part with Pd solution of opposite charge by place part in solution for 2-5 minutes, then dry with Kimwipe. Note, large flat parts must be very thoroughly dried. Flowing air can be used to removed trapped fluid. Then place parts in DMAB solution for 2-5 minutes until areas where deposition occur become darker or black. Remove part and dry.

For Ni-P, heat solution to 80 °C and place part in for 5-20 minutes until a coating of desired thickness/quality is obtained.

For copper, place in Caswell solution at room temperature for 20-60 minutes until a coating of sufficient quality and thickness is achieved. Do not leave overnight.

For magnetite, heat solution to 80 °C and plate for 5-20 minutes.

For ZnO, heat solution to 60 °C and plate 2-4 hours. Recommend repeating procedure next day to build thick layers.

For MWCNT deposition, dip part into solution, wait several minutes, removing, **gently** rinse with water, and dry with Kimwipe.

### ***Copper Electrodeposition and Measurement***

A Caswell copper electrodeposition kit was used as received and per their instructions. Cu was electrodeposition required 1-10 minutes by touching area with a needle, at 2-4 volts, and 0.02 to 0.05 amps depending on part size. Conductivity measured using 4-point probe (VersaSTAT3). The conductivity was calculated with the following equation

$$\sigma_{film} = \frac{\ln 2}{\pi t} \left( \frac{I}{V} \right)$$

where  $t$  is the thickness of the thin film. We fractured the struts and measured the thickness under a scanning electron microscope (EI Quanta 600 FEG), averaging the thickness measurements.

### ***Dielectric Measurement***

The dielectric areas consisted of either pure photopolymer (PEGDA) or a composite of PEGDA, PZT powder varying from 0 to 40vol% and initiator mixed by high-energy ball milling. To measure the dielectric constant of these composites, a 7mm by 7mm by 0.08mm solid films were printed and electrodes are deposited on the top and bottom surfaces to form a capacitor. The capacitance ( $C$ ) of these films was measured on a commercial capacitance meter (KEYSIGHT E4990A) and the dielectric constants ( $\epsilon_r$ ) were calculated by,

$$\epsilon_r = \frac{Cd}{A\epsilon_0}$$

where  $d$  is the distance between the electrodes (0.08mm),  $A$  is the cross-section area of the samples ( $1\text{cm}^2$ ) and  $\epsilon_0$  is the electric constant ( $8.854 \times 10^{-12}$  F/m). The dielectric constant can be

varied of a wide range by varying the amount of a dielectric powder within our photocurable polymer.

### **Measurement of Catalyst loading on charged Polymer**

Square films of each resin were made, and dipped into catalyst solution, wicked dry with tissue and measured with no other treatment. Aliquots of the same catalyst solution were used for all samples after being freshly made, and film sizes were kept relatively similar,  $5 \pm 1 \text{ mm}^2$ , to minimize variability.

## 5.9 References

1. Liu, N. *et al.* Three-dimensional photonic metamaterials at optical frequencies. *Nat. Mater.* **7**, 31–37 (2008).
2. Radke, A., Gissibl, T., Klotzbücher, T., Braun, P. V. & Giessen, H. Three-Dimensional Bichiral Plasmonic Crystals Fabricated by Direct Laser Writing and Electroless Silver Plating. *Adv. Mater.* **23**, 3018–3021 (2011).
3. Burckel, D. B. *et al.* Fabrication of 3D Metamaterial Resonators Using Self-Aligned Membrane Projection Lithography. *Advanced Materials* **22**, 3171–3175 (2010).
4. Macdonald, E. *et al.* 3D Printing for the Rapid Prototyping of Structural Electronics. *IEEE Access* **2**, 234–242 (2014).
5. MacDonald, E. & Wicker, R. Multiprocess 3D printing for increasing component functionality. *Science* **353**, aaf2093 (2016).
6. Adams, J. J. *et al.* Conformal Printing of Electrically Small Antennas on Three-Dimensional Surfaces. *Adv. Mater.* **23**, 1335–1340 (2011).
7. Wang, T. C., Chen, B., Rubner, M. F. & Cohen, R. E. Selective Electroless Nickel Plating on Polyelectrolyte Multilayer Platforms. *Langmuir* **17**, 6610–6615 (2001).
8. Dressick, W. J., Dulcey, C. S., Georger, J. H., Calabrese, G. S. & Calvert, J. M. Covalent Binding of Pd Catalysts to Ligating Self-Assembled Monolayer Films for Selective Electroless Metal Deposition. *J. Electrochem. Soc.* **141**, 210–220 (1994).
9. Ishikawa, A., Kato, T., Takeyasu, N., Fujimori, K. & Tsuruta, K. Selective electroless plating of 3D-printed plastic structures for three-dimensional microwave metamaterials. *Appl. Phys. Lett.* **111**, 183102 (2017).

10. Farrer, R. A. et al. Selective Functionalization of 3-D Polymer Microstructures. *J. Am. Chem. Soc.* **128**, 1796–1797 (2006).
11. Angel, K., Tsang, H. H., Bedair, S. S., Smith, G. L. & Lazarus, N. Selective electroplating of 3D printed parts. *Additive Manufacturing* **20**, 164–172 (2018).
12. Li, J., Wang, Y., Xiang, G., Liu, H. & He, J. Hybrid Additive Manufacturing Method for Selective Plating of Freeform Circuitry on 3D Printed Plastic Structure. *Advanced Materials Technologies* **0**, 1800529.
13. Takeyasu, N., Tanaka, T. & Kawata, S. Fabrication of 3D metal/polymer microstructures by site-selective metal coating. *Appl. Phys. A* **90**, 205–209 (2008).
14. Takeyasu, N., Tanaka, T. & Kawata, S. Fabrication of 3D Metal/Polymer Fine Structures for 3D Plasmonic Metamaterials. in *Photonic Metamaterials: From Random to Periodic* (2007), paper WD3 WD3 (Optical Society of America, 2007). doi:10.1364/META.2007.WD3.
15. Abrantes, L. M. & Correia, J. P. On the Mechanism of Electroless Ni- P Plating. *J. Electrochem. Soc.* **141**, 2356–2360 (1994).
16. Nakanishi, T., Masuda, Y. & Koumoto, K. Site-Selective Deposition of Magnetite Particulate Thin Films on Patterned Self-assembled Monolayers. *Chem. Mater.* **16**, 3484–3488 (2004).
17. Saito, N. *et al.* Low-Temperature Fabrication of Light-Emitting Zinc Oxide Micropatterns Using Self-Assembled Monolayers. *Adv. Mater.* **14**, 418–421 (2002).
18. Ichinose, I., Senzu, H. & Kunitake, T. A Surface Sol–Gel Process of TiO<sub>2</sub> and Other Metal Oxide Films with Molecular Precision. *Chem. Mater.* **9**, 1296–1298 (1997).

19. Boontongkong, Y., Cohen, R. E. & Rubner, M. F. Selective Electroless Copper Deposition within Block Copolymer Microdomains. *Chem. Mater.* **12**, 1628–1633 (2000).
20. Matula, R. A. Electrical resistivity of copper, gold, palladium, and silver. *J. Phys. Chem. Ref. Data* **8**, 1147–1298 (1979).
21. Jiang, L., Gao, L. & Sun, J. Production of aqueous colloidal dispersions of carbon nanotubes. *J. Colloid Interface Sci.* **260**, 89–94 (2003).
22. Hensleigh, R. et al. Charge-programmed three-dimensional printing for multi-material electronic devices. *Nature Electronics* **3**, 216–224 (2020).
23. Cui, H. et al. Three-dimensional printing of piezoelectric materials with designed anisotropy and directional response. *Nature Materials* **18**, 234 (2019).